TECHNISCHE UNIVERSITÄT MÜNCHEN

Physik-Department
Lehrstuhl für Funktionelle Materialien

Structure and dynamics of nanocomposites composed of hydrophobically modified ethoxylated urethanes and magnetite nanoparticles in the hydrogel and dried state

Antonella Campanella

Vollständiger Abdruck der von der Fakultät für Physik der Technischen Universität München zur Erlangung des akademischen Grades eines

Doktors der Naturwissenschaften (Dr. rer. nat.)

genehmigten Dissertation.

Vorsitzende:	Prof. Dr. Martin Zacharias
Prüfer der Dissertation:	1. Prof. Dr. Peter Müller-Buschbaum
	2. Prof. Dr. Friedrich Simmel

Die Dissertation wurde am 07.07.2016 bei der Technischen Universität München eingereicht und durch die Fakultät für Physik am 18.07.2016 angenommen.

Ai miei genitori

Abstract

This work presents the preparation, and the structural and the dynamic characterizations of a novel type of nanocomposites based on hydrophobically modified ethoxylated urethanes (HEUR) and coated magnetite nanoparticles (MNPs). The structure of the novel nanocomposites as hydrogels and as dry films is analyzed using small angle neutron scattering (SANS). The MNPs influence the network-like structure of the gel phase, while they do not affect significantly the HEUR structure in the dried state. The magnetic response of the dried state shows a superparamagnetic behaviour. The dynamics of the nanocomposites as hydrogels is investigated with dielectric relaxation (DRS) and neutron spin echo spectroscopy (NSE). We find that, upon the addition of MNPs, the segmental dynamics of the polymer is slowed down on the nanoseconds scale. On the other hand, as found for the structure, the addition of MNPs does not have a significant effect on the segmental dynamics of the polymer in the dried state, investigated by DRS and thermally stimulated depolarization current (TSDC).

Zusammenfassung

Diese Arbeit befasst sich mit der Präparation, und der strukturellen und dynamischen Charakterisierung einer neuen Sorte von Nanokompositen, die aus hydrophob modifizierten ethoxylisierten Urethanen (engl. HEUR) und beschichteten Magnetit-Nanopartikeln (engl. MNPs) bestehen. Die Struktur der neuartigen Nanokompositen als Hydrogele und als trockene Filme wurde mittels Neutronenkleinwinkelstreuung (engl. SANS) untersucht. Die MNP beeinflussen die netzartige Struktur der Gel-Phase, während die HEUR-Struktur im Trockenen nicht signifikant geändert wird. Das magnetische Ansprechen des trockenen Zustandes entspricht einem super-paramagnetischen Verhalten. Die Dynamik der Nanokomposite als Hydrogele wurde mit dielektrischer Relaxations-Spektroskopie (DRS) und Neutronen-Spin-Echo-Spektroskopie (NSE) beobachtet. Wir haben gefunden, dass die Beigabe von MNP die Segmentdynamik des Polymers auf der Nanosekunden Skala verlangsamt. Wie auch schon für die Struktur beobachtet, gibt es keinen signifikanten Effekt auf die Segmentdynamik der Polymere durch die MNP im trockenen Zustand, wie mit der DRS und mit der thermisch stimulierten Depolarisationsstrom-Methode (engl. TSDC) bestimmt.

Contents

1. Introduction

The combination of magnetic and dielectric properties, stability and the biocompatibility make magnetic nanocomposite materials suitable for both environmental and biomedical applications and for use in electronics [1, 2]. For instance, magnetic nanocomposites have been used for the emission enhancement of organic light emission diodes (OLEDs) [3], the increase of the power conversion efficiency of both heterojunction poly-small molecules solar cells [4] and can be used as electromagnetic wave absorbers thanks to their elevated magnetic and dielectric permeability connected to dissipative properties [5, 6]. Typically, magnetic nanocomposite materials comprise a polymer matrix and inorganic filler particles. The polymer matrix is used for processing, whereas the inorganic filler adds the magnetic contribution to the system. Frequently, diblock copolymer templates have been used to guide specially coated magnetic nanoparticles (MNPs) in polymer matrices to get control on the MNPs dispersion [7–9].

In this work we present a novel type of nanocomposite systems consisting of hydrophobically modified ethoxylated urethane (HEUR), as the polymer matrix, and coated magnetite nanoparticles (MNPs), as inorganic filler particles.

Hydrophobically modified ethoxylated urethane (HEUR) is a telechelic polymer having poly(ethylene oxide) (PEO) as the main hydrophilic chain and alkyl alcohol groups as hydrophobic end groups. Aqueous solutions of HEUR have been studied from the theoretical point of view as model systems [10, 11]; and their rheological properties have been extensively investigated [12–15]. Among the different kinds of structures that the HEUR polymers form in water, at high polymer concentration (ϕ_{poly} >10 wt %), they form a complex extended network with aggregates composed of the hydrophobic ends which act as crosslinks between the hydrophilic main chains (Fig. 2.2) [10, 12, 13]. The presence of the micellar cores is exploited, embedding into them hydrophobic molecules or particles with specific functions, i.e. pigments, inorganic nanoparticles. The embedding of such hydrophobic particles into the micellar domains of the polymer network is a good way to avoid their aggregation, and therefore, to obtain a homogeneous dispersion into the polymer matrix. Thus, this feature of the telechelic polymer gels is very useful in the formulation of nanocomposites. Furthermore, polyurethanes are good candidates for polymer matrices in nanocomposite systems because of their versatility [16].

The inorganic component of our novel nanocomposites are coated magnetite nanoparticles. Iron oxide nanoparticles, and in particular magnetite nanoparticles (Fe_3O_4), are widely used in several kinds of applications, from the medical ones, e.g. magnetic resonance technology or drug delivery, to the environmental ones [17–19].

A crucial point in the design of composite systems is the control of the nanoparticle dispersion in the polymer hydrogel matrix. Therefore, it is important to determine the morphology of these systems. In this work, the investigation of the morphology of the HEUR-MNPs nanocomposites is carried out by small angle neutron scattering (SANS) (chapter 3). Structural characterization is carried out in order to determine the polymer matrix structure in the hydrogel and in the dry state.

On the other hand, the dynamic investigation of the HEUR-MNPs nanocomposites is focused on the study of the segmental dynamics of the polymer. The use of different experimental techniques, i.e. differential scanning calorimetry (DSC), dielectric relaxation spectroscopy (DRS) and neutron spin echo (NSE) (chapter 3) is aimed at achieving a profound understanding of the dynamics of the investigated system. The importance of the understanding of the segmental dynamics lies in the fact that it is related to both the mechanical and the dielectric properties of the material which are useful for applications.

Therefore, with the structural and dynamic characterization of the novel HEUR-MNPs nanocomposites presented in this work, we would like to answer to the following questions:

- Which are the conditions for a homogeneous MNP distribution in the polymer matrix?
- Which modes exist in the gel and in the dry films? How do they interrelate?
- Are there specific properties occurring for the dispersed MNPs?

In the following chapters, the achieved results will give a tentative answer to these questions. Furthermore, the influence of the MNPs on both the structure and the dynamics of the pure polymer matrix will be profoundly discussed.

2. Theoretical aspects

This chapter comprises the theoretical background for the experimental studies and interpretations presented in this thesis. First of all, the main features of the investigated systems and the state of art of the related scientific research are discussed in detail. The discussion begins with the individual components, i.e. the telechelic polymers and the magnetic nanoparticles (MNPs). The second part of the chapter focuses on the theoretical aspects of the experimental techniques employed in the present experimental work. In particular, all the different theories used for the interpretation of the structural and dynamic characterization are explained. In the section 2.1.3 the theory by Daoud and Cotton on star polymers is discussed, as it is relevant for interpretation of the dynamic characterization of the investigated nanocomposites and, in section 2.2.6, the scattering from gel systems is explained.

2.1. Investigated systems

2.1.1. HEUR polymers: a special type of telechelic polymers

The term "telechelic" originates from the Greek words *telos*, far, and *chelos*, claw, therefore, it describes a molecule having two "claws" far away from each other. The term was originally proposed by Uraneck in 1960 [20] to describe macromolecules having two reactive groups at both chain ends, i.e. polymeric diols. In a more general sense, the term is used to define polymers possessing end groups which are not necessarily chemically reactive but that can from inter or intra-molecular interactions via self-assembly forces, for instance van der Waals forces or hydrogen bonds. The simplest example of telechelic polymers are triblock copolymers of type ABA or, more generally ABC, dispersed in the appropriate solvent which is selective for the midblock B, leading to the aggregation of the terminal groups through hydrophilic or hydrophobic effects [21,22]. In Fig. 2.1 examples of ABA and ABC types of telechelic poly(ethylene oxide) (PEO)-based triblock copolymers are shown [23]. In the last twenty years telechelic polymers have attracted great interest for several reasons. First of all, they are useful for the synthesis of multi-copolymers and can be used as precursors of chain extender. Furthermore, telechelic polymers represent

a fundamental model for understanding intra- and inter-molecular aggregation process in polymers in relation with the polymer conformation.

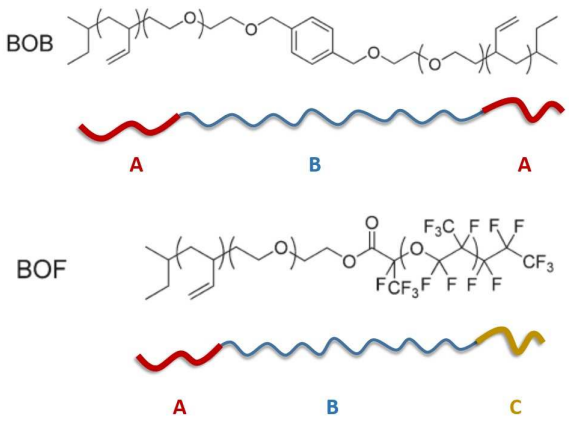

Figure 2.1.: Sketch of ABA and ABC types of telechelic polymers. BOB is the name of the block-copolymer with poly(ethylene oxide) (PEO) as mid-block and 1,2-polybutadiene (PB) as end-blocks. The second type, having 1,2-polybutadiene (PB) and poly(perfluoropropylene oxide) (PFPO) as end-blocks, is denominated BOF [23]

Telechelic polymers represent the simplest example of *associating polymers*, which contain hydrophobic, polar or ionic groups which are able to associate and form aggregates similar to the ones formed by surfactants. The aggregation process of associating polymers has been intensively investigated in previous studies [10, 24]. It was found by Semenov and coworkers, that telechelic polymers, above the critical micelle concentration (CMC) aggregate in *flower-like* micelles made of compact hydrophobic cores composed of the hydrophobic ends of the telechelic polymer chain (Fig. 2.2). The inner structure of the hydrophobic core is similar to the structure of the micelle formed by star polymers [25,26]. For the micelles formed by telechelic polymers the aggregation number p is defined as the number of chains per micelle and it depends on the energy of interaction between the hydrophobic groups and on their length. For associating polymers, the typical aggregation number was found to be between p=5 and p=50 [27, 28]. In the theoretical study of the equilibrium and the dynamic properties of associating polymers, the aggregation number is considered to be a known fixed large number: indeed, the aggregation number was observed to be rather insensitive to concentration and molecular weight of soluble parts [29]. The main difference between star polymers and *flower-like* micelles is the fact that two star polymers in a good solvent always repel each other, while *flower-like* micelles can be connected to each other because telechelic polymers can form bridges between neighbouring micelles (see Fig. 2.2).

As explained by Semenov in the study of the equilibrium and dynamic properties of a

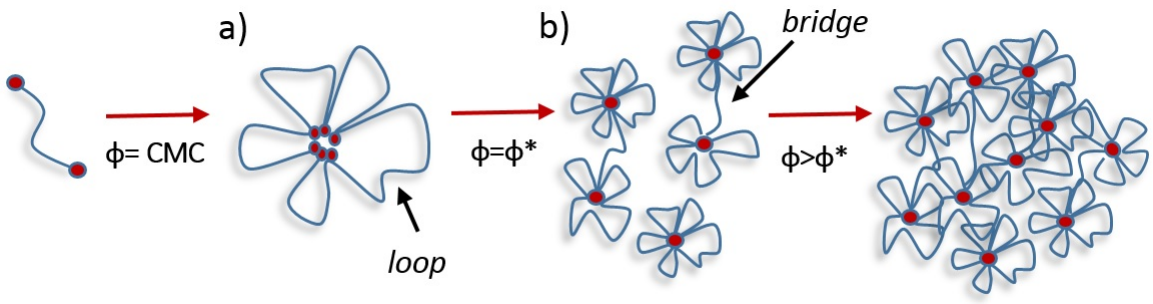

Figure 2.2.: Sketch of a phase diagram of a telechelic polymer a) a flower consisting in p=5 chains b) bridging between flowers. The hydrophobic end-groups are depicted in red

solution of telechelic polymers [10], increasing the telechelic polymer concentration above the CMC, $\phi > CMC$, the micelles phase separate and form a densely packed micelles phase connected to each other. At a certain concentration $\phi = \phi^*$, the flowers form a reversible network where they are connected by "bridges". This process is shown in Fig. 2.2 b). Increasing the polymer concentration further, such that $\phi > \phi^*$, the viscosity of the gel increases exponentially and macroscopic percolation structures are formed. This effect is known as *thickening* of associating polymers [30] and several models were adopted to explain it [11]. Because of the *thickening* effect, the associating polymers are widely used in the formulation of water-borne paint, as rheology modifier [31, 32].
Belonging to the more general class of *associating* polymers the so-called hydrophobically modified polymers (HM-P) consist of a water soluble polymer with hydrophobic groups chemically attached to the hydrophilic polymer backbone. The earliest studies on this class of polymers, in particular on polyelectrolytes, was carried out by Strauss and coworkers [33]. HM-P can be divided into two categories depending on how the hydrophobic groups are situated in the hydrophilic polymer backbone: i) end-capped HM-polymers: where the hydrophobic groups are attached at both ends of the hydrophilic backbone (Fig. 2.3 a)) ii) comb-like HM-polymers: where the hydrophobic groups are grafted along the hydrophilic backbone (Fig. 2.3 b))

The telechelic polymers used in this work belong to the class of end-capped HM-polymers and they are called hydrophobically modified ethoxylated urethanes (HEUR). They consist of a polyethylene glycol (PEG) main chain with urethanes segments and two C_{10}-C_{22} alkyl chains at both ends of the main chain. The most common synthesis procedure for commercially available HEUR polymers involves PEG of low molecular weight, e.g. 6000, which reacts with an excess of diisocyanate. The product is a polymer chain with urethane segments and one reactive isocyanate group at each chain end. They react with long alkyl chain alcohol leading to the HEUR polymer structure. A simplified scheme of the synthesis of HEUR is shown in Fig. 2.4. Using different synthesis approaches, in-

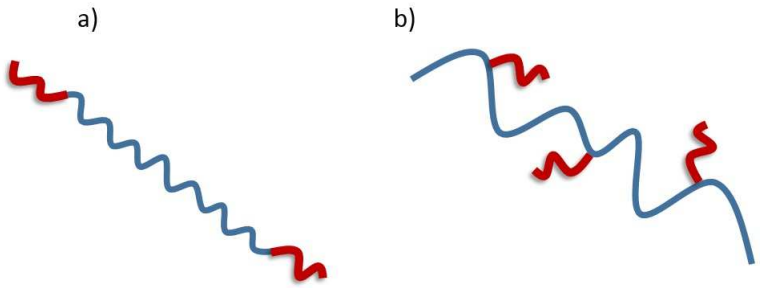

Figure 2.3.: Sketch of a) end-capped b) comb-like hydrophobically modified polymer. The hydrophobic blocks are depicted in red

volving the reaction of an alcoholethoxylate with diisocyanate, HEUR polymers with more narrow molecular weight distribution were synthetized [34]. HEUR polymers synthetized in this way have a polydispersity index, i.e. weight average molecular weight M_w / number average molecular weight M_n, of about 1.1. The commercial HEUR polymer used in this work, has a polydispersity index of 1.04.

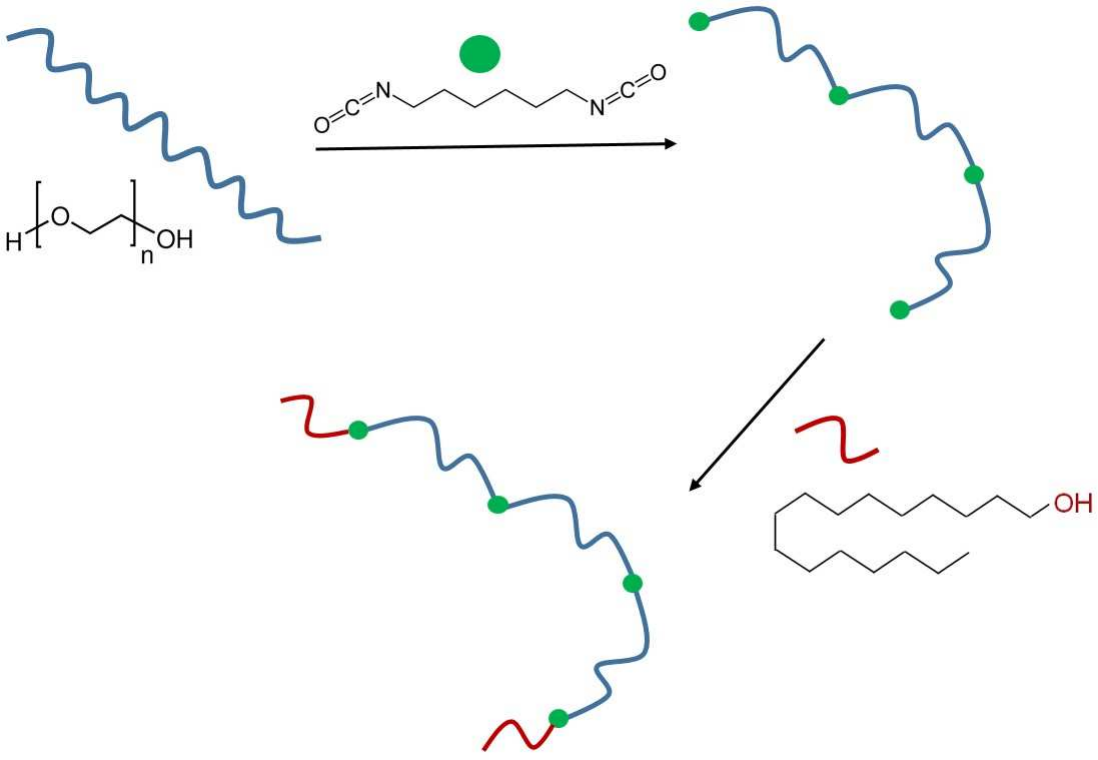

Figure 2.4.: Schematic synthesis reactions path of HEUR polymers. Blue lines show the PEG backbone, the red ones the long chain alcohol and the green circles the diisocyanate groups or diurethane likages

The phase behaviour of HEUR polymers in water solution has been extensively investigated through rheology, leading to a structural and dynamic model of their aggregation process as a function of the concentration and of the molecular weight of the polymer [12, 15, 35, 36]. As seen for the generic associating polymers, HEUR polymers form *flower-like* micelles, when the polymer concentration exceeds the CMC. Because of the thermal motion, periodically the hydrophobic ends detach from the micellar core and move around in the surrounding. The "floating" hydrophobic end is soon captured again by another micellar core. The increase of the polymer concentration leads to the formation of *clusters* of flowers, because of the bridging between the micelles, as shown in the sketch in Fig. 2.2. At high polymer concentration ($\phi > 10$ wt%), bridging chains will percolate the whole volume, and a network will be formed. The network of bridging chains is also called *permanent network*. The rheological properties of a typical HEUR polymer solution in the concentration regime $\phi > \phi^*$ can be visualized from the shear-stress dependent viscosity (Fig. 2.5).

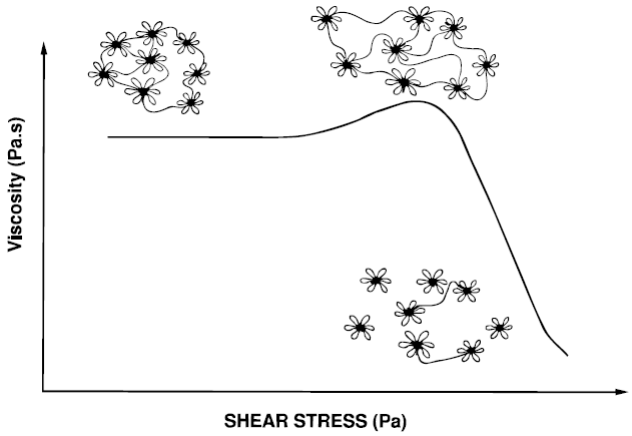

Figure 2.5.: Viscosity versus shear stress of a HEUR polymer solution showing the Newtonian, shear-thickening and shear-thinning regimes [13]

In the curve of the viscosity as a function of the shear stress it is possible to observe the following regimes:

- at low shear stress, it is possible to observe a shear stress-independent viscosity. This is defined as *Newtonian* behaviour, and it is typical of liquids
- at intermediate shear stress, an increase of the viscosity is observed, and this effect is the so-called *shear thickening*. It arises for the stretching of the bridging chains between the micellar cores of the network
- at high shear stress, a steep decrease of the viscosity is observed. It is due to the fragmentation of the bridging chains. This effect is called *shear tinning*.

From nonlinear rheological measurements of HEUR aqueous solutions at different HEUR concentration it was found that the *thickening* disappears at polymer concentration $\phi^* \sim$ 4 wt% [12,37]. Annable and coworkers found that, at this concentration, an *impermanent network* is formed [14].

2.1.2. Semidilute polymer solutions: the blob concept

As seen in the paragraph 2.1.1, at high polymer concentration ($\phi > 10$ wt%), HEUR telechelic polymers form a permanent network where the "micellar domains" act as non-covalent cross-links of the polymer network (Fig. 2.2). In this concentration regime, the hydrophilic middle chains are in contact between each other and they form entanglements. This feature, is also the characteristic property of semidilute polymer solutions. In this case, the contact between different polymers leads to topological cross-links. Therefore, such a solution presents a gel-like behaviour. The concentrated HEUR polymer solution ($\phi >$10 wt%) can be approximated to a semidilute polymer solution. This assumption is relevant for the interpretation of the results of the dynamic investigation of HEUR hydrogels achieved in this work (chapter 6). The semidilute polymer solution is a network with many polymer-polymer contacts of a typical distance ξ_c, which is also called *correlation distance/length*. In order to describe the semidilute polymer solutions, the concept of *blob*, introduced by DeGennes, is used [25, 38]. The *blobs* are regions of size ξ which contain chain segments, consisting of g monomers, characterized by single linear chain behaviour (Fig. 2.6).

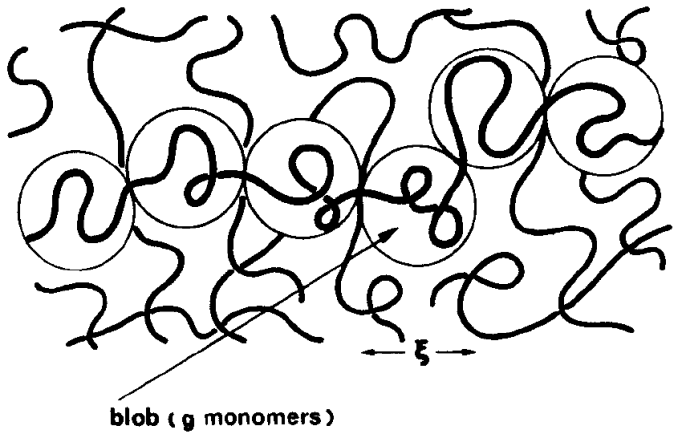

Figure 2.6.: Polymer network formed by a semidilute polymer solution. A blob is defined by the intersection of a chain segment with other chains

Within such a blob, the polymer behaves like in a good solvent, and one finds g monomers inside the blob according to:

$$\xi \propto g^{\nu} \tag{2.1}$$

with ν=0.6, being the *Flory exponent* for polymers in a good solvent [39]. Beyond the blob, the correlation is lost and the polymer chain behaves like an ideal coil, like in a θ-solvent, and its radius of gyration is defined as:

$$R_g = \sqrt{3}\xi_c \left(\frac{N}{g}\right)^{1/2} \tag{2.2}$$

with N being the number of monomers of the polymer chain and g being the number of monomers within the blob. The blob size depends on the polymer concentration. Considering the concentration regimes of a flexible polymer solution (schematically depicted in Fig. 2.7), we observe that:

- for low polymer concentration $\phi < \phi^*$, the blob becomes large, and finally covers a full single polymer molecule, therefore $g \approx N$. In this case, the polymer behaves like in good solvent, where the interactions between the polymer molecules and the solvent molecules are favourable
- at the overlap concentration, $\phi = \phi^*$, the monomer concentration of an isolated polymer reaches the overall polymer concentration:

$$\phi^* \propto N{R_g}^{-3} \propto N^{1-3\nu} \tag{2.3}$$

- at high concentration, $\phi \approx 1$, the blobs size shrinks and a blob contains approximately one monomer, $g \approx 1$.

The correlation length ξ_c can be therefore expressed as:

$$\xi_c \propto R_g \left(\frac{\phi}{\phi^*}\right)^{y} \tag{2.4}$$

Therefore, at the overlap concentration, the correlation length ξ_c is equal to the radius of gyration, and at higher concentration, it is proportional to ϕ^y. In the high concentration regime, it may be assumed that the blob size does not depend on the polymerization degree, if the concentration remains constant. The polymer is assumed to be much larger than a blob, thus, there is no influence on the blobs anymore. From the N-dependence of the radius of gyration from eq. 2.3, and considering the eq. 2.4 one obtains:

$$\xi_c \propto N^{\nu} \left(\frac{\phi}{N^{1-3\nu}}\right)^{y} \propto N^0 \tag{2.5}$$

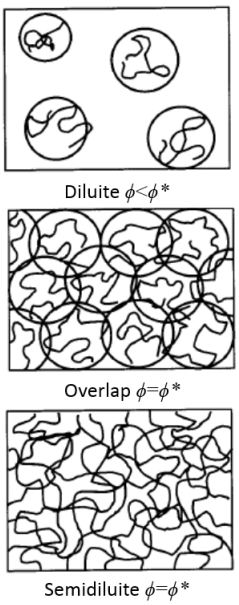

Figure 2.7.: Concentration regimes in flexible polymer solutions. Above the overlap concentration ϕ^*, the polymer chains interpenetrate [40]

Therefore, the exponent is found to be $y = -3/4$. The two dependences on the polymer concentration ϕ, firstly of the correlation length, $\xi_c \propto \phi^{-3/4}$; and of the radius of gyration, $R_g^2 \propto \phi^{-1/4}$, have been found experimentally by neutron scattering [25].

Since we compared the semidiluted polymer solution with the HEUR concentration solution, it is important to point out the difference between these two systems. Fig. 2.6 shows a network formed by a semidilute polymer solution. Such a structure is defined as *topological gel*. In the *topological gel* the polymer chains with bulky end-groups are neither covalently cross-linked as in chemical gels, nor attractively interacting as physical gels, but are just topologically interlocked. In this case, the blob is defined by the intersection of a chain segment with other chains. In the case of a network formed by telechelic polymers, the blob is also defined as the spherical region containing a chain segment between topological crosslinks, but the hydrophobic domains act as additional constrains for the polymer chain, and they are considerably bigger than the simple topological crosslinks in the topological gel. This fundamental difference is illustrated in Fig. 2.8.

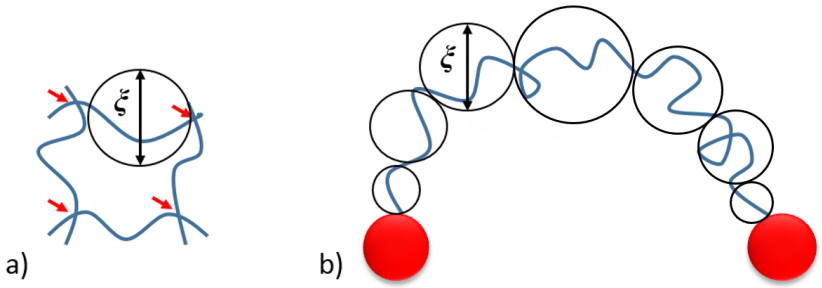

Figure 2.8.: The concept of blobs in the a) topological gel and in the b) HEUR gel are depicted, where the micellar domains are represented as the red balls. The blob's size ξ is shown in both cases

2.1.3. Conformation model of *star shaped* polymers applied to telechelic polymers

In polymer chemistry, *branching* occurs by replacing a substituent on a monomer subunit of the polymer backbone with another covalently bounded chain of the same type of polymer. In the case of graft copolymers, the new chain is of a different type. The simplest type of branched polymers are the *star shaped* polymers, where linear chains are connected to a central core. The core of the *star* can be an atom, molecule, or macromolecule (Fig. 2.9).

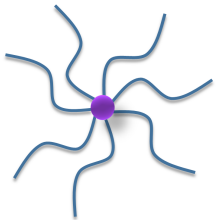

Figure 2.9.: Sketch of a *star shaped* polymer consisting of seven linear chains connected to the branch point (depicted in purple)

Star shaped polymers have received continuous attention over a long time [41]. Most of the theoretical work was done to determine the conformation of *star shaped* polymers in their unperturbed state [42, 43]. Daoud and Cotton, developed a model for the conformation of *star shaped* polymers in order to predict the swelling properties of a star as a function of the quality of the solvent and the monomer concentration ϕ [25]. This so-called *DC-model* was used by Halperin for the study of the behaviour of star polymers confined to a narrow slit in a good solvent [44]. In the *DC-model* a uniform single star

made of f branches joining at the centre of the star is considered. Each branch has N statistical units of size a. The *DC-model* is based on two observations:

- star polymers have spherical symmetry
- because all branches have to join at the center, the concentration of monomers in this region is very high. When one gets away from the centre, the concentration decreases, leading eventually to the single (linear) chain problem in the outside region where the different branches can be considered as being far apart between each other. Therefore, the volume fraction of the monomers of the branch, ϕ, is expected to be a decreasing function of the distance from the center of the star, r.

The DC concept of star polymer is depicted in Fig. 2.10. The structure of *star shaped* polymers is described in terms of *blobs* [25]. *Blobs* occupy regions of size ξ, which depends on the local monomer concentration.

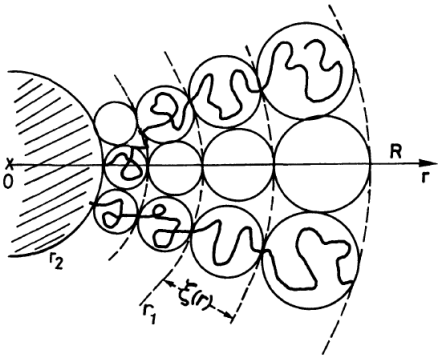

Figure 2.10.: Daoud-Cotton conception of a star polymer. Every branch is made of a succession of blobs with size ξ increasing from the centre of the star to the outside [25]

The DC-model postulates the following:

- the size ξ of the *blob* depends on the distance to the center of the star r: $\xi = \xi(r)$. This means that the concentration profile is *self similar* and thus $\xi \sim r$.
- In a sperical shell of radius r and thickness $\xi(r)$ there are f blobs.

The second postulate determines the f dependence of ξ: the volume of a spherical shell $r^2\xi$ is equal to that of f blobs of volume ξ each. Therefore, this dependence reads like:

$$\xi \sim r/f^{1/2} \tag{2.6}$$

According to the DC-model, in the star one expects to find three different regions:

- a core, or center, where the monomer concentration is very high ($\phi \sim 1$) and the monomers are closed packed
- an ideal or Gaussian zone, where ξ is small enough so that the blobs are ideal:

$$\xi(r) \sim n^{1/2}(r)a \tag{2.7}$$

  where $n(r) = n(\xi(r))$ is the number of monomers in a blob of size ξ
- an exterior *corona*, where ξ is higher and where excluded volume interactions are important within the blobs [44].

The *DC-model* can be applied also to other systems. For example, micelles can be treated as stars but with a larger center composed of non-covalently-bound groups [45]. In fact, in his study on the dynamic properties of solutions of telechelic polymers in the limit of high aggregation number [10], Semenov used the *blobs* picture to describe the micelles structure formed by telechelic polymers. On the same line, in this work we apply the *DC-model* to the polymer network formed by the telechelic HEUR polymers in aqueous solution. In fact, the hydrophobic domains of the HEUR network can be approximated to the centers of stars connected between each other. Therefore they can be considered as the branch points of long graft copolymers. This approximation is schematized in Fig. 2.11.

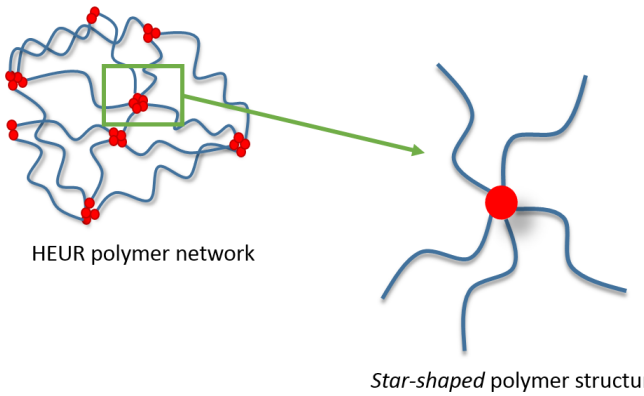

Figure 2.11.: The region of the HEUR network (left) near the hydrophobic domain is magnified. The magnified portion on the right side is similar to a *star shaped* polymer with five branches

The extension of the *DC-model* to the investigated systems was crucial to understand the effects of polymer conformation on the dynamics of the system.

2.1.4. Magnetite nanoparticles (MNPs)

In the last two decades, the enhanced interest of researchers in nanoparticles is due to their unusual physical and chemical properties compared to the massive (*bulk*) materials. In particular, in the case of the magnetic properties, the difference between the bulk material and the nanoparticles is especially pronounced. In fact, it was found that the magnetization per atom and the magnetic anisotropy of the nanoparticles can be much greater than those of the bulk material. The magnetic properties of nanoparticles are limited by many factors, for instance the chemical composition, the particle size and shape and its interaction with the surrounding matrix and the neighbouring particles. Before discussing in detail the magnetic properties of nanoparticles, it is necessary to give a definition to the so-called *nanoparticle*. A nanoparticle is an object with size between 1 and 100 nm. On the other hand, when we talk about the bulk material we refer to a typical size above 1 μm [46]. Among the most widely encountered magnetic nanoparticles, for the preparation of the magnetic nanocomposites investigated in the present work, we have chosen magnetite nanoparticles, which are mostly used in biomedical applications because of their biocompatibility [47]. The chemical formula of magnetite is Fe_3O_4. It crystallizes with the spinel structure. The large oxygen ions are closed packed in a cubic arrangement and the smaller Fe ions fill the gaps. There are two types of gaps: i) the tetrahedral site, where the Fe ions are surrounded by 4 oxygen ions ii) the octahedral site, where the Fe ions are surrounded by 6 oxygen ions (Fig. 2.12). The tetrahedral and the octagonal sites form two magnetic sublattices, namely A and B. The spins on the A sublattice are antiparallel to those on the B sublattice. The two crystal sites are very different and result in complex forms of exchange interactions between Fe ions both between and within the two types of sites.

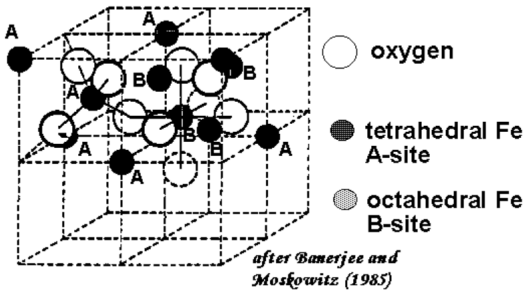

Figure 2.12.: Spinel structure of magnetite showing the tetrahedral and the octahedral sites, indicated as A and B respectively

Because of the crystalline structure, the magnetite is *ferrimagnetic*, although it was considered a ferromagnet until Néel, in the 1940, provided the theoretical framework for

understanding ferrimagnetism. Several approaches for the synthesis of magnetite nanoparticles are present. In some cases, they are synthetized through thermal decomposition of compounds containing Fe^{3+} ions under an oxygen-deficient atmosphere. It is accompanied by partial reduction of Fe^{3+} to Fe^{2+}. Thus, thermolysis of $Fe(acac)_3$ in dyphenylether in presence of small amounts of hexadecane-1,2-diol, which acts as reducer of part of ions Fe^{3+} to Fe^{2+}, gives Fe_3O_4 nanoparticles with size of 1 nm (Fig. 2.13).

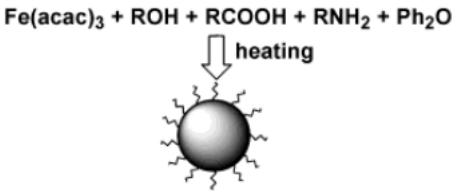

Figure 2.13.: Scheme of the synthesis of magnetite nanoparticles using oleic acid (RCOOH) and oleyamine (RNH_2) as capping agents [48]

The size of the produced nanoparticles can be increased by adding an excess of $Fe(acac)_3$ into the reaction mixture [48].

2.1.5. Basic theory of superparamagnetism

The response of materials to an applied magnetic field depends on their magnetic structure. A way to categorize the magnetic nature of materials, is considering the magnetic susceptibility value, χ. The magnetic susceptibility is a dimensionless quantity that indicates the degree of magnetization of a material in response to an applied magnetic field. It is defined as:

$$M = \chi H \tag{2.8}$$

where M is the magnetization of the material (the magnetic dipole moment per unit volume), and H is the magnetic field strength.

Accordingly to the value of the magnetic susceptibility of the material χ, the following types of magnetism can be distinguished:

1. Large χ: these materials include *ferromagnetic*, *ferrimagnetic* or *antiferrimagnetic*. They can have, even without influence of an external magnetic field, a strong ordering of the orientation of the magnetic moments. In particular, as shown in Fig. 2.14, *ferromagnetic* materials exhibit parallel alignment of moments resulting in large net magnetization even in the absence of a magnetic field. The elements Fe, Ni, and Co and many of their alloys, are typical ferromagnetic materials. Two distinct features of ferromagnetic materials are their spontaneous magnetization and the existence of magnetic ordering temperature. The spontaneous magnetization is the net magnetization that exists inside a uniformly magnetized microscopic volume in absence of magnetic field. The magnitude of this magnetization, at 0 K, is dependent on the spin magnetic moments of electrons. Even though electronic exchange forces in ferromagnets are very large, thermal energy eventually overcomes the exchange and produces a randomizing effect. This occurs at the so-called Curie temperature (T_C). Below the Curie temperature, the ferromagnet is ordered and, above it, disordered. The saturation magnetization goes to zero at the Curie temperature. In addition to the Curie temperature and the saturation magnetization, ferromagnets can retain memory of an applied field once it is removed. This behaviour is called hysteresis and a plot of the variation of magnetization with magnetic field is called hysteresis loop (Fig. 2.16). Another hysteresis property is the coercivity of remanence (H_r). This is the reverse field which, when applied and then removed, reduces the saturation remanence to zero. It is always larger than the coercive force. On the other hand, the magnetic ordering called *ferrimagnetism* occurs in ionic compounds, such as oxides, e.g. Fe_3O_4, magnetite. The magnetic structure is composed of two magnetic sublattices (called A and B) separated by oxygens. The exchange

interactions are mediated by the oxygen anions. In ferrimagnets, the magnetic moments of the A and B sublattices are not equal and it results in a net magnetic moment. Thus, Ferrimagnetism is similar to ferromagnetism. Therefore, it exhibits all the hallmarks of ferromagnetic behaviour - spontaneous magnetization, Curie temperatures, hysteresis, and remanence. However, ferro- and ferrimagnets have very different magnetic ordering (see Fig. 2.14). In contrary to the *ferrimagnetic* materials, in *antiferromagnetic* materials the A and B sublattice magnetic moments are exactly equal but opposite, so that the net moment is zero (Fig. 2.14).

2. Small χ:

   - If $\chi > 0$ the material is *paramagnetic*. The magnetic moments are only aligned under the influence of an external field in its direction (Fig. 2.14).
   - If $\chi < 0$ the material is *diamagnetic*. The magnetic moments are only aligned under the influence of an external field in its opposite direction.

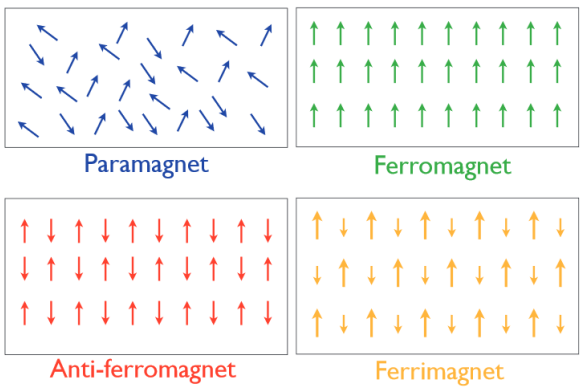

Figure 2.14.: Sketch of the different types of magnetic materials. The different orientations of the atomic magnetic moments are shown

When the size of the material is reduced to the nano-scale length the phenomenon of *superparamagnetism* can occur. It is a type of magnetism that occurs in small *ferromagnetic* and *ferrimagnetic* nano-sized materials. The size of the nanoparticles which show this property is between 1 nm and 50 nm, depending on the material. They are single-domain nanoparticles, meaning that the total magnetic moment can be regarded as a giant moment composed of all the individual magnetic moments of the atoms of which compose the nanoparticle. Very often, nanoparticles show a certain preference for the direction, along to which their magnetization aligns. These nanoparticles are said to have an *anisotropy* in these directions. If there is one direction much preferred over all others, the nanoparticles have *uniaxial anisotropy*. Nanoparticles with uniaxial anisotropy

randomly flip the direction of their magnetization, and this effect is induced by thermal energy. The average time to perform such a flip is given by the relaxation time, τ, which reads:

$$\tau = \tau_0 \exp\left\{\frac{\Delta E}{k_B T}\right\} \tag{2.9}$$

where τ_0 is a length of time, characteristic of the material, called the *attempt time*, which is around 10^{-9} s [49], ΔE is the energy barrier which the magnetization flip has to overcome, k_B is the Boltzmann constant and T is the temperature.

The energy barrier for the magnetization flip occurs in particles with anisotropies. It depends on the particles volume:

$$\Delta E = KV \tag{2.10}$$

where K is the *anisotropy* constant and V is the volume of the particle.

The superparamagnetic state of nanoparticles does not only depend on the temperature T and on the energy barrier ΔE, but also on the measurement time of the experimental technique used. If the measurement time, τ_m, is smaller than the average time between magnetization flips (relaxation time τ), the nanoparticle is in a well defined state that is called *blocked state*. If the measurement time is larger than the relaxation time τ, we will observe fluctuations in the magnetization and a time-averaged net moment equal to zero (Fig. 2.15).

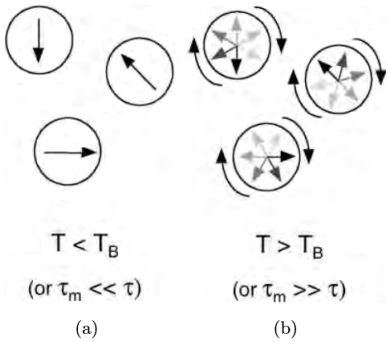

Figure 2.15.: a) The measurement time is much smaller than the relaxation time. Blocked state. b) The measurement time is much larger than the relaxation time. Superparamagnetic state [50]

The temperature at which the nanoparticle is in its blocked state is called *blocking temperature*, T_B. It is related to the nanoparticle's size by the eq. 2.10, considering that:

$$\Delta E = 25 k_B T_B = KV \tag{2.11}$$

Therefore, by measuring the blocking temperature T_B of the nanoparticles, it is possible to obtain their size [51, 52].

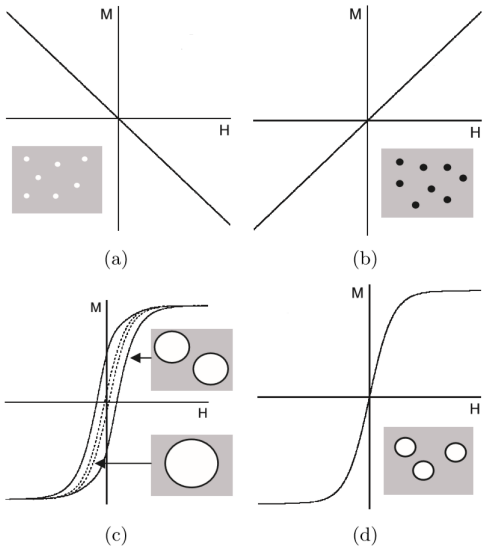

Figure 2.16.: Magnetization curves of a) diamagnetic materials b) paramagnetic materials c) ferromagnetic material d) superparamagnetic material. The big and small particles represent, respectively, single-domain and multi-domain particles [50]

In conclusion, in order to compare the magnetic response of different materials, in Fig. 2.15 the magnetization curves of *diamagnetic*, *paramagnetic*, *ferromagnetic* (or *ferrimagnetic*) and *superparamagnetic* materials are shown. In the case of the *ferromagnetic* material, a hysteresis loop can be observed. For single-domain particles, the loop is narrow (dashed line), while for multi-domain particles the loop is quite broad. On the other hand, the magnetization curve of the *superparamagnetic* material has similar sigmoid shape of the *ferromagnetic* one, but no loop is observed. This means that when the magnetic field is removed, the magnetization drops to zero. The difference between the *ferromagnetic* (or *ferrimagnetic*) behaviour and the *superparamagnetic* one is determined by the size of the particle: as soon as it gets small enough, the latter effect takes over [53].

2.2. Scattering methods: theoretical background

2.2.1. Neutrons as probe

Scattering with light, X-rays and neutron radiation is an established method of investigating structures from microscopic up to mesoscopic length scales, i.e. 10^{-10} – 10^{-6} m. The cross section depends on the refractive index for light, the atomic number (number of electrons) for X-rays and on the overall structure/magnetic moment of the nucleus for neutrons. Neutrons represent a versatile probe to investigate the fundamental properties of the matter. They also present advantages over to X-rays. The are several reasons for this:

- The neutrons are electrically neutral, hence they can penetrate into matter and probe bulk properties. They have a penetration depth higher than X-rays, which, in some cases, can penetrate only several hundreds of nm.
- The interaction of neutrons with matter is via nuclear forces. Therefore, they interact differently with neighbouring elements (e.g. Mn, Fe and Ni). It makes them an ideal probe for samples containing hydrogen, carbon or oxygen, therefore for organic materials, i.e. soft matter.
- The neutrons have large magnetic moment, hence they are sensitive to the magnetic properties of the sample.
- The neutron scattering from deuterium and hydrogen is very different, by this an exchange of both in a molecule enables the labeling of certain parts without changing the chemical properties significantly.

2.2.2. Scattering theory

Scattering experiments are often applied to the study of soft matter. Three types of scattering experiment, each giving different information, can be performed:

- *Static scattering*: the dependence on the scattering angle θ of the averaged scattering intensity is measured. It gives structural information about the scattering medium.
- *Dynamic scattering*: the analysis of the time dependence of fluctuations in the scattered radiation is performed. It give information about the dynamics of the system.
- Absolute magnitude of the scattered intensity averaged over time: gives information on the mass or molecular weight of the scattering objects.

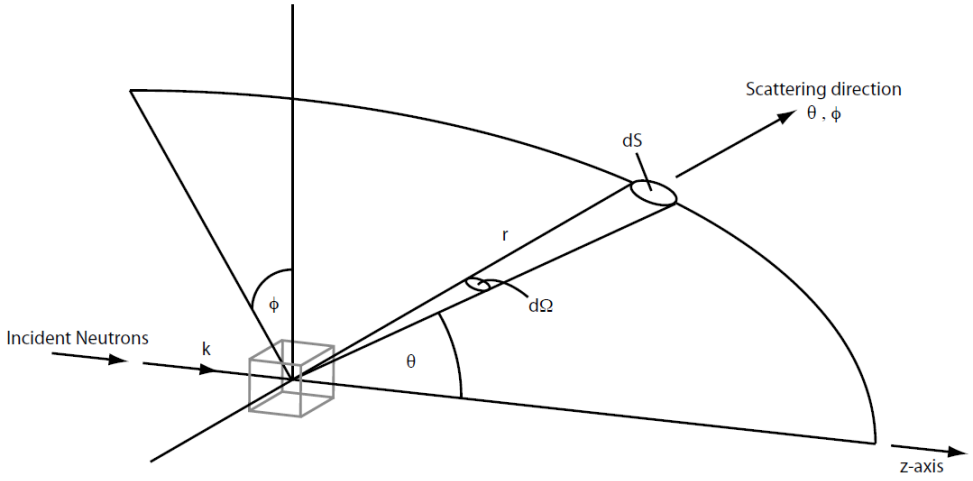

Figure 2.17.: Geometry of a typical scattering experiment, showing the scattering direction polar coordinates (r, θ, ϕ), and the scattering angle dΩ [54]

The geometry of a typical scattering experiment is depicted in Fig. 2.17.

A neutron beam with a given energy E is incident on a sample. Part of the beam passes through the sample, some is scattered under a scattering angle θ in the solid angle $d\Omega$. The intensity of the scattered radiation $I(\theta, t)$ is measured by a detector placed at an angle θ. The time dependence of the scattered intensity is due to the fact that it fluctuates in time. The portion of sample which is illuminated by the incident radiation and detected by the detector is defined as "scattering volume" V. In order to have a scattering event the scattering medium has to be inhomogeneous because the scattering is caused by fluctuations in the medium. The fluctuations are associated with variations in the density of the scattering material within the medium.

Assuming that the distance from the sample, $\mathbf{r}$, is large, the incoming and the scattered neutrons can be considered as stationary plane waves. In a quantum mechanical description of the scattering process, the incident neutron beam can be described by the scattering wave function $\psi(\mathbf{r})$:

$$\Psi(\mathbf{r}) = \Psi_0 \exp(i\mathbf{k}_I\mathbf{r}) \tag{2.12}$$

Where k_I is the propagation vector of the incident neutron beam, considered as electromagnetic radiation, with magnitude of:

$$k_I = |\mathbf{k}_I| = k = \frac{2\pi}{\lambda} \tag{2.13}$$

Where λ is the wavelength of the radiation in the medium.

On the other hand, the total wave function is given by:

$$\Psi(\mathbf{r}) \overset{r\to\infty}{\to} \Psi_I(\mathbf{r}) + \Psi_s(\mathbf{r}) \propto \exp(i\mathbf{k}_I\mathbf{r}) + f(\Omega)\frac{\exp(i\mathbf{k}_S\mathbf{r})}{|\mathbf{r}|} \tag{2.14}$$

Where $\Psi_I(\mathbf{r})$ and $\Psi_s(\mathbf{r})$ are the wave functions of the incoming and the scattered neutrons, $\mathbf{k}_S$ is the propagation vector of the scattered beam and $f(\Omega)$ is the amplitude of the scattered wave.

For the description of the scattering event we assume that the scattering is so weak that:

- part of the neutrons pass through the sample undeviated, few are scattered and the probability of double and higher-order scattering is negligible
- the incident beam is not distorted significantly by the medium.

The second assumption corresponds to the Born approximation. The last assumption is that the scattering is quasi-elastic. Therefore, the scattering events leads to a very small difference in frequency between the incident radiation and the scattered one. The difference between the propagation vectors of the incident and the scattered radiation is defined as:

$$\mathbf{q} = \mathbf{k}_s - \mathbf{k}_I \tag{2.15}$$

According to the quasi-elastic approximation, the energy transfer during the scattering process is negligible, therefore the absolute value of the scattered wave vector is unchanged ($|\mathbf{k}_S| = |\mathbf{k}_I|$). Hence, the scattering vector q reads:

$$q = |\mathbf{q}| = \frac{4\pi}{\lambda} sin(\theta/2) \tag{2.16}$$

A sketch of the scattering vector q in case of quasi-elastic scattering, is shown in Fig.2.18.

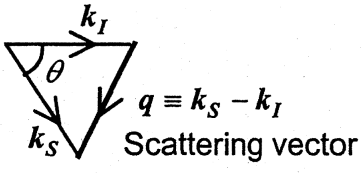

Figure 2.18.: Scattering vector $\mathbf{q}$ as difference of the scattered wave vector $\mathbf{k}_S$ and the incident wave vector $\mathbf{k}_I$

In a neutron scattering experiment, the differential scattering cross-section is measured. It is defined as:

$$\frac{d\sigma}{d\Omega} = \frac{\text{number of particles scattered into the solid angle } d\Omega \text{ per time}}{\text{number of incoming particles per time and area}} \tag{2.17}$$

The differential scattering cross section can be rewritten in terms of the ampitude of the scattered wave $f(d\Omega)$:

$$\frac{d\sigma}{d\Omega} = |f(d\Omega)|^2 \tag{2.18}$$

Considering a sample containing N_S point-like scatters, the interaction potential with the neutron radiation $V(r)$, can be described by the Fermi pseudo potential [55] [56].

$$V(\mathbf{r}) = \frac{2\pi\hbar^2}{m_n} \sum_{i=1}^{N_S} b_i \delta(\mathbf{r} - \mathbf{r_i}) \tag{2.19}$$

where N_S in the number of point-like scatters and b_i is the scattering length, which determines the interaction strength. For neutrons it is an experimentally derived characteristic quantity of the nuclei.

The scattering amplitude $f(\Omega)$ can be rewritten as:

$$f(\Omega) = -\frac{m_n}{2\pi\hbar} \int d\mathbf{r}' V(\mathbf{r}') \exp(-i\mathbf{k}_S \cdot (\mathbf{r}' - \mathbf{r})) \tag{2.20}$$

Considering the free movement of the scattering centres and their possible orientations relative to the scattering vector $\mathbf{q}$, the cross section can be written taking into account equation 2.18, 2.19 and 2.20:

$$\frac{d\sigma}{d\Omega}(q) = \left\langle \left| \sum_{i=1}^{N_S} \sum_{j=1}^{N_S} b_i b_j \exp(-i\mathbf{q}\mathbf{r_{ij}}) \right| \right\rangle = \left\langle \left| \sum_{i=1}^{N_S} b_i \exp(-i\mathbf{q}\mathbf{r_i}) \right|^2 \right\rangle \tag{2.21}$$

where the relative coordinates $\mathbf{r_i} = \mathbf{R_i} + \mathbf{r_{ij}}$ are explained in the scheme in Fig. 2.19. The position of scattering centres within particles are given by $\mathbf{r_{ij}}$.

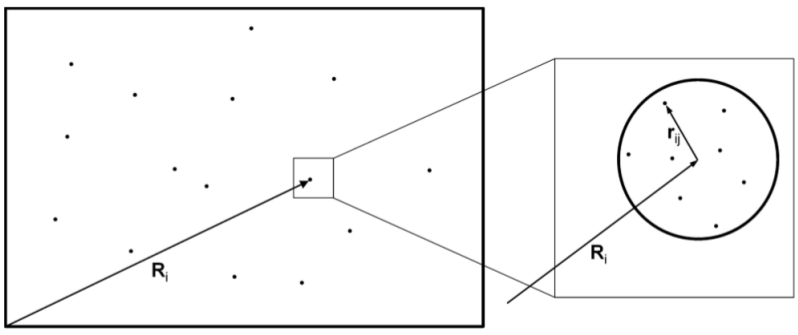

Figure 2.19.: Sketch of relative coordinates $\mathbf{r_i} = \mathbf{R_i} + \mathbf{r_{ij}}$ [57]

Therefore, the scattering cross-section depends only on the absolute value of the scattering vector $|\mathbf{q}|$. In neutron scattering, the scattering length b_i depends also on the spin. Assuming statistically distributed spin states of the nucleus, the scattering length can be

decomposed into an average $|b_i|$ and a deviation δb_i. Hence, the scattering cross-section can be decomposed into terms:

$$\frac{d\sigma}{d\Omega}(q) = \left\langle \left| \sum_{i=1}^{N_S} \langle b_i \rangle \exp(-i\mathbf{q}\mathbf{r}_i) \right|^2 \right\rangle + \sum_{i=1}^{N_S} \left\langle b_i^2 \right\rangle - \langle b_i \rangle^2 = \left(\frac{d\sigma}{d\Omega}(\mathbf{q}) \right)_{coh} + \left(\frac{d\sigma}{d\Omega}(\mathbf{q}) \right)_{incoh} \quad (2.22)$$

The first term represents the coherent contribution to the scattering cross-section, which contains the phase factor $\exp(-i\mathbf{q} \cdot \mathbf{r_i})$. It results from the superposition of the scattering from pairs of scatterers. This term takes into account interference effects, and it is therefore named *coherent scattering*. The second term does not contain any phase information, and it corresponds to the scattering from single atoms which superimpose in an incoherent manner (adding intensities, not amplitudes). Therefore this second term, called *incoherent scattering* is proportional to the number of atoms, or scatters, N_S. It generates a homogeneous incoherent background. The real quantity that is measured in a neutron scattering experiment is the macroscopic coherent cross section, defined as:

$$\frac{d\Sigma}{d\Omega}(\mathbf{q}) = \frac{1}{V_S} \frac{d\sigma}{d\Omega}(\mathbf{q}) \quad (2.23)$$

With V_S being the sample volume. Introducing the relative coordinates $\mathbf{r_i} = \mathbf{R_i} + \mathbf{r_{ij}}$, the system can be decomposed in N_z particles at position R_i with N_i scattering centres each. Therefore, the macroscopic scattering function reads:

$$\frac{d\Sigma}{d\Omega}(\mathbf{q}) = \frac{1}{V_S} \left\langle \left| \sum_{i=1}^{N_z} \exp(-i\mathbf{q}\mathbf{R_i}) \sum_{j=1}^{N_i} b_{ij} \exp(-i\mathbf{q}\mathbf{r_{ij}}) \right|^2 \right\rangle \quad (2.24)$$

Since eq. 2.24 contains the position of the scattering centers within the particles, r_{ij}, the sum over N_i only incorporates information about the inner structure of the particles. This term is the so-called scattering amplitude:

$$A_i(\mathbf{q}) = \sum_{j=1}^{N_i} b_{ij} \exp(-i\mathbf{q}\mathbf{r_{ij}}) \quad (2.25)$$

Inserting eq. 2.25 into eq. 2.24, one obtains the following expression for the macroscopic scattering cross section:

$$\frac{d\Sigma}{d\Omega}(\mathbf{q}) = \frac{1}{V_S} \left\langle \sum_{i=1}^{N_z} \sum_{i'=1}^{N_z} A_i^*(q) A_{i'}(q) \exp(-i\mathbf{q}(\mathbf{R_i} - \mathbf{R_{i'}})) \right\rangle \quad (2.26)$$

Considering monodisperse and isotropic particles, the average over all particle orientations can be done individually for each sum:

$$\frac{d\Sigma}{d\Omega}(\mathbf{q}) = \frac{N_z}{V_S}\left\langle |A(\mathbf{q})|^2 \right\rangle + |\langle A(\mathbf{q})\rangle|^2 \left\langle \sum_{i=1}^{N_z}\sum_{i'=1}^{N_z} \exp(-i\mathbf{q}(\mathbf{R_i} - \mathbf{R_{i'}})) \right\rangle \tag{2.27}$$

The macroscopic scattering cross-section can be written in terms of the so-called *form factor*, $P(q)$, and *structure factor*, $S(q)$ which are defined as:

$$S(q) = 1 + \frac{1}{N_z}\frac{|\langle A(\mathbf{q})\rangle|^2}{\left\langle |A(\mathbf{q})|^2 \right\rangle} \left\langle \sum_{i=1}^{N_z}\sum_{i'=1}^{N_z} \exp(-i\mathbf{q}(\mathbf{R_i} - \mathbf{R_{i'}})) \right\rangle \tag{2.28}$$

$$P(q) = \left\langle |A(\mathbf{q})|^2 \right\rangle \propto \left\langle \sum_{i=1}^{N_i} b_i \exp(-i\mathbf{q}\mathbf{r_i}) \sum_{j=1}^{N_j} b_j \exp(-i\mathbf{q}\mathbf{r_j}) \right\rangle \tag{2.29}$$

As seen in eq. 2.29, the form factor $P(q)$ contains the intra-particle correlations. It gives information about the inner structure of the sample, therefore about the shape of the scattering objects. On the other hand, the structure factor $S(q)$ (eq. 2.28), contains the correlations between different particles. This means that it gives information about the interaction potential between the particles in the investigated sample. Therefore, the macroscopic scattering cross-section can be written in terms of the form factor and the structure factor:

$$\frac{d\Sigma}{d\Omega}(q) = \frac{N_z}{V_S}P(q)S(q) \tag{2.30}$$

For infinite dilution the structure factor is fixed to the unity, i.e. $S(q) = 1$ which means that the macroscopic cross-section in eq. 2.30 reduces to:

$$\frac{d\Sigma}{d\Omega}(q) = \frac{N_z}{V_S}P(q) \tag{2.31}$$

In the following sections, models for the form factor $P(q)$ and for the scattering cross section $d\sigma/d\Omega$ will be explained.

2.2.3. Form factor for homogeneous spheres

In small angle neutron scattering, it is fundamental to consider that the atomic structure cannot be resolved. Therefore, the distribution of scattering centers can be considered continuous and their scattering length b_i summed up to a scattering length density:

$$\rho_j = \frac{\sum_{i=1} b_{ij}}{V_j} \tag{2.32}$$

The scattering length density is normalized by the total volume of the summed scattering centers $\sum_{i=1} V_{ij} = V_j$. This volume is usually the volume of a monomer (in a polymer) or of a molecule. Assumed it, the discrete Fourier transformation of the spacial distribution of scattering centers can be rewritten as a continuous Fourier transformation over the cell with volume V_z:

$$A(\mathbf{q}) = \int_{V_z} d\mathbf{r}\rho(\mathbf{r}) \exp(-i\mathbf{q}\cdot\mathbf{r}) \tag{2.33}$$

Introducing the contrast $\Delta\rho(\mathbf{r}) = \rho(\mathbf{r}) - \rho(0)$, the eq. 2.33 can be written like:

$$\begin{aligned} A(\mathbf{q}) = \int_{V_z} d\mathbf{r}\Delta\rho(\mathbf{r}) \exp(-i\mathbf{q}\cdot\mathbf{r}) + \rho_0 \int_{V_z} d\mathbf{r} \exp(-i\mathbf{q}\cdot\mathbf{r}) = \\ = \int_{V_z} d\mathbf{r}\Delta\rho(\mathbf{r}) \exp(-i\mathbf{q}\cdot\mathbf{r}) + \rho_0\delta(\mathbf{q}) \end{aligned} \tag{2.34}$$

The second term of eq. 2.34 results in a delta distribution, $\delta(\mathbf{q})$, which gives a constant distribution for $\mathbf{q} = 1$. In the case of radial symmetric particles, we have $\Delta\rho(\mathbf{r}) = \Delta\rho(r)$, and the scattering amplitude of the eq. 2.34, can be written in terms of polar coordinates as:

$$\begin{aligned} A(q) = \int_0^\infty dr\Delta\rho(r)r^2 \int_{-1}^1 d\cos(\theta) \exp(-iqr\cos(\theta)) \int_0^{2\pi} d\phi = \\ 2\pi \int_0^\infty dr\Delta\rho(r)r^2 \int_{-1}^1 d\cos\theta(\cos(qr\cos\theta) - i\sin(qr\cos\theta)) \end{aligned} \tag{2.35}$$

If we integrate over $\cos\theta$ the expression of the scattering amplitude becomes:

$$A(q) = 4\pi \int_0^\infty dr\Delta\rho(r)\frac{\sin(qr)}{qr}r^2 \tag{2.36}$$

It is common to split $\Delta\rho(r)$ into a product of a constant factor $\delta\rho$ and a r-dependent function $\eta(r)$, called *density function*. Therefore the eq. 2.36 can be written as:

$$A(q) = \Delta\rho V_p A_0(q) \tag{2.37}$$

with V_p being the volume of the particles, and $A_0(q)$:

$$A_0(q) = \frac{4\pi \int_0^\infty dr \Delta\eta(r) \frac{sinqr}{qr} r^2}{4\pi \int_0^\infty dr \Delta\eta(r) r^2} \tag{2.38}$$

The expression 2.38 is normalized to fulfil $A_0(q) = 1$. No analytical solution is given for eq. 2.38, therefore, it is calculated through numerical methods and special object shapes. The most simple case for which an expression of eq. 2.37 can be calculated is the case of the sphere. In the case of a two-component system, composed of spherical particles with radius R and scattering length density ρ and another component treated as background, e.g. the solvent, the density function $\eta(r)$ for a sphere assumes the values:

$$\eta(r) = \begin{cases} 1, & 0 \leq r \leq R \\ 0, & R < r \end{cases} \tag{2.39}$$

Inserting these conditions in eq. 2.37 and eq. 2.38, the scattering amplitude for spherical objects reads:

$$A(q) = \Delta\rho(r) \frac{4\pi}{3} R^3 P(q) \tag{2.40}$$

where the term $P(q)$ is the form factor of a sphere with radius R, which is given by:

$$P(q) = \frac{3[\sin(qR) - qR\cos(qR)]}{q^3 R^3} \tag{2.41}$$

2.2.4. Scattering from polydisperse core-shell spheres

The form factor of the sphere introduced in eq. 2.41 can be used to obtain the form factor of a core-shell sphere, which is a simple way to describe systems like, for instance, micelles. Considering the sketch in Fig. 2.20, if R_{core} is the radius of the core of the core-shell particle with scattering length density ρ_{core}, and t is the thickness of the shell, the form factor of the spherical core-shell particle is given by:

$$F(q) = \frac{4\pi}{3} R_{core}^3 (\rho_{core} - \rho_{shell}) \frac{3j_1(qR_{core})}{qR_{core}} + \frac{4\pi}{3}(R_{core} + t)^3 (\rho_{shell} - \rho_0) \frac{3j_1(qR_{core} + qt)}{qR_{core} + qt} \tag{2.42}$$

whereas R_{core} is the radius of the micellar core, t the thickness of the shell, ρ_0 the scattering length density (SLD) of the solvent and $j_1(x)$ is the the first order spherical Bessel function:

$$j_1(x) = \frac{sin(x) - xcos(x)}{x^2} \tag{2.43}$$

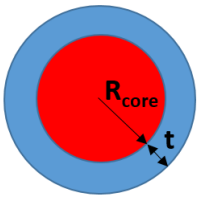

Figure 2.20.: Sketch of a spherical core-shell particle with core radius R_{core} and shell thickness t

Considering a collection of spherical core-shell particles with polydisperse cores, as described by Kotlarchyk and Chen in the analysis of the scattering from polydisperse interacting colloids [58], we need to introduce the Zimm-distribution function $f(R_{core})$ [58]. In a system of spherical core-shell particles with polydisperse cores, it describes the distribution of the cores radii R_{core}. It is given by:

$$f(R_{core}) = \left(\frac{Z+1}{\bar{R}_{core}}\right)^{Z+1} R_{core}^Z \exp\left(-\frac{Z+1}{\bar{R}_{core}}\right) \frac{1}{\Gamma(Z+1)} \tag{2.44}$$

with Γ being the function:

$$\Gamma(x) = \int_0^\infty t^{x-1} \exp(-t) dt \tag{2.45}$$

in this case, the form factor of eq. 2.42 takes into account the polydispersity of the cores with the Zimm-distribution function and it reads:

$$\left|\left\langle F(q)\right\rangle\right|^2 = \left|\int_0^{+\infty} F(q)f(R_{core})dR_{core}\right|^2 \tag{2.46}$$

$$\left\langle |F(q)|^2\right\rangle = \int_0^{+\infty} |F(q)|^2 f(R_{core})dR_{core} \tag{2.47}$$

where $f(R_{core})dR_{core}$ is the probability of a sphere having a radius between R and $R + dR$.

The form factor of polydisperse core-shell particles of eq. 2.42, was used by Sarvesh and co-workers to describe hydrogels composed of telechelic polymers, as a collection of flower-like micelles connected by bridges consisting of the hydrophilic chains of the polymers [59]. According to this model, as depicted in Fig. 2.21, each micelle is characterized by hydrophobic micellar cores with radius R_{core}, and a hydrophilic shell with thickness t.

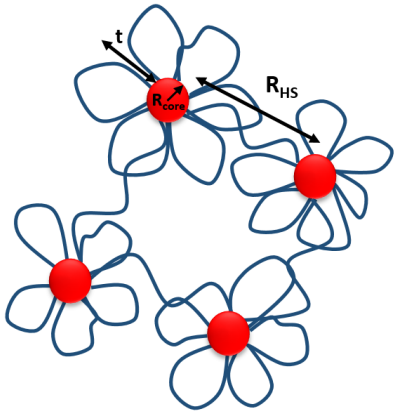

Figure 2.21.: Sketch of the hydrogel composed of HEUR polymers: R_{core} is the radius of the hydrophobic micellar core, t is the shell thickness and R_{HS} is the distance between the flower-like micelles

The overall scattering intensity of the micelles solution can be written as:

$$I(q) = NP(q)S(q) + bkg \tag{2.48}$$

where N is the number density of the scattering centres (micelles), $\Delta\rho$ is the contrast of scattering length density between the micelles and the solvent, $S(q)$ is the structure factor and bkg is the incoherent background. The function $P(q)$ contains the form factor of the scattering particle $F(q)$:

$$P(q) = \left\langle |F(q)|^2\right\rangle \tag{2.49}$$

with $F(q)$ being the form factor of polydisperse core-shell particles with radius R_{core} of eq. 2.42.

In the expression of the scattering intensity 2.48, the function $S(q)$ is the structure factor describing the interactions between the flower-like micelles. It is the unity for low polymer concentration. According to this model, it is given by:

$$S(q) = 1 + \frac{\left|\left\langle F(q)\right\rangle\right|^2}{\left\langle |F(q)|^2\right\rangle}(SHS(q) - 1) \tag{2.50}$$

where $SHS(q)$ is the repulsion potential typical of hard spheres, which is defined by the volume fraction of the interacting particles ϕ, and by the distance R_{HS} between the scattering centers.

2.2.5. Scattering from microemulsions: the Teubner-Strey theory

For concentrated systems, the factorization of the scattering cross section in to the product of a form factor and a structure factor shown in the eq. 2.30 does not hold anymore. In some cases, different approaches may be used for getting a theoretical expression of the cross sections as a function of the microscopical characteristics of the system under investigation. The thermodynamic description of the global phase behaviour of multicomponent mixtures, as microemulsions, provides an explanation of the features of their phase behaviour. In particular, the phenomenological Landau theory [60], describes the thermodynamic behaviour of such multicomponent systems. In the past, this approach was employed to describe the scattering from microemulsions [61–64]. The phenomenological Landau free energy F is obtained from an expansion of the order parameter ψ , which describes the interaction between the components of the system. It reads like:

$$F = \int f(\psi, \nabla\psi, \Delta\psi) d^3r \tag{2.51}$$

with f being:

$$f = a_0 + a_1\psi + a_2\psi^2 + a_3\psi^3 + a_4\psi^4 + a_5\psi^5 + ... + c_1(\nabla\psi)^2 + c_2(\Delta\psi)^2 + ... \tag{2.52}$$

At which order the expansion is truncated depends on the system. According to Teubner and Strey [65], the combination of coefficients:

- $a_i = 0$ except $a_2 > 0$
- $c_i = 0$ except $c_1 < 0, c_2 > 0$

is sufficient to explain the typical features of the scattering curves of microemulsions. In order to investigate the scattering of neutrons in the case of an isotropic liquid, one has to study the fluctuations of the order parameter ψ. For small fluctuations in a homogeneous phase, orders higher than second in ψ can be neglected. Therefore, in the eq. 2.52 we only have $a_2 > 0$. For ordinary liquids we have that $c_1 > 0$ and higher order gradient terms can be neglected, leading to the Orstein-Zernike expression for the scattering intensity distribution [66]:

$$I(q) = \frac{1}{a^2 + c_1 q^2} \tag{2.53}$$

The surface tension σ is proportional to $\sqrt{c_1}$. In microemulsions the characteristic feature is the tendency of surface active agents to create spontaneously interfaces which corresponds to a negative *microscopic surface tension*, therefore it must be $c_1 < 0$. In view of these considerations, stability requires at least one more gradient term of higher order in the expression of the free energy (eq. 2.51), so that the simplest form of the free energy F is given by:

$$F = \int [a_2\psi^2 + c_1(\nabla\psi)^2 + c_2(\Delta\psi)^2]d^3r \tag{2.54}$$

with $a_2 > 0$, $c_1 < 0$, $c_2 > 0$, and the stability condition is:

$$4a_2c_2 - c_1^2 > 0 \tag{2.55}$$

Considering the change in free energy by fluctuations of the order parameter ψ, the free energy of eq. 2.54 leads to a scattering intensity distribution which reads:

$$I(q) \sim \frac{1}{a_2 + c_1 q^2 + c_2 q^4} \tag{2.56}$$

The correlation function leading to eq. 2.56 is given by [67]:

$$\gamma(r) = \frac{d}{2\pi r} \exp(-r/\xi) \sin\left(\frac{2\pi r}{d}\right) \tag{2.57}$$

The Fourier transform of eq. 2.57 gives the following expression of the scattering intensity from microemulsions:

$$I(q) = \frac{8\pi/\xi\langle\eta^2\rangle c_2 V}{a_2 + c_1 q^2 + c_2 q^4} \tag{2.58}$$

with $\langle\eta^2\rangle = \langle(\rho - \bar{\rho})^2\rangle$ being the mean square fluctuation of the scattering intensity. The coefficients of eq. 2.58 are defined as:

- $a_2 = (q_0^2 - \xi^{-2})$

- $c_1 = -2(q_0^2 - \xi^{-2})$
- $c_2 = 1$

where q_0 is the position of the correlation peak appearing in the scattering pattern of microemulsions. The eq. 2.58 is called *Teubner-Strey formula*. With eq. 2.58 we introduced two length scales characteristic of microemulsions, defined as:

$$\xi = \left[\frac{1}{2}\left(\frac{a_2}{c_2}\right)^{1/2} + \frac{1}{4}\frac{c_1}{c_2}\right]^{-1/2} \tag{2.59}$$

and

$$d = 2\pi\left[\frac{1}{2}\left(\frac{a_2}{c_2}\right)^{1/2} - \frac{1}{4}\frac{c_1}{c_2}\right]^{-1/2} \tag{2.60}$$

with ξ being the correlation length and d the domain size (periodicity) of the microemulsion.

In the discussion of the results obtained from the structural characterization of the nanocomposites investigated in this work (discussed in the chapter 5), we use these two length scales to characterize our systems, i.e. polymer network formed by the HEUR telechelic polymers (Fig. 2.2). The approximation of the HEUR polymer network to a microemulsion system is justified by the presence of microscopic interfaces between the hydrophobic domains and the hydrophilic chains/solvent. In this scenario, the characteristic domain size d indicates the distance between the hydrophobic domains of the polymer network (formed by the alkyl end-groups of each HEUR molecule), while the correlation length ξ represents the correlation length of the network, i.e. the distance between two monomers of different hydrophilic backbones of the polymers (Fig. 2.22).

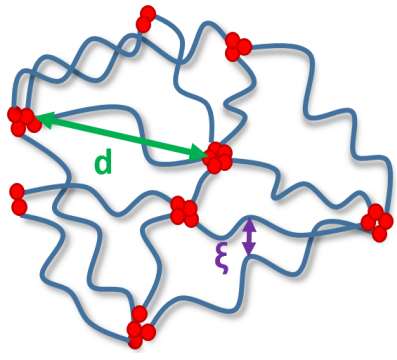

Figure 2.22.: Sketch of the HEUR polymer network in aqueous solution. The domain spacing d, resembling the distance between the hydrophobic domains, and the correlation length ξ are shown by the arrows (green and purple respectively)

A typical SANS pattern of bicontinuous microemulsions is shown in Fig. 2.23.

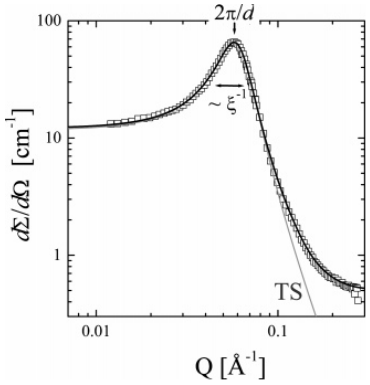

Figure 2.23.: Typical macroscopic scattering cross section of a bicontinuous microemulsion as a function of the scattering vector q. The Teubner-Strey fit is shown as a grey line, and the extended formula including the Beaucage term is shown as a black line [68]

The main features of the SANS pattern shown in Fig. 2.23 are:

- high scattering intensity at low scattering vectors q, indicating strong long-range fluctuations
- a correlation peak at $q_{max} = 2\pi/d$ which indicates the domain size
- a peak width which is proportional to the reciprocal of the correlation length ξ^{-1}

As discussed above, these two features, i.e. the domain size and the correlation length, are well described by the Teubner-Strey (TS) formula (eq. 2.58). However, the Teubner-Strey theory is based on an expansion of the free energy with long-range fluctuations, neglecting the always present short-range undulations of the membrane surrounding the domains. This means that the TS theory does not allow to fit the scattering data in the Porod region, i.e. high q values. An empirical approach based on the description of fractal scattering by Beaucage [69] allows for the extension of the model fitting over a large range of q. This theory consists in a Guinier term describing the overall size at large wavelengths and an empirical term according to the fractal behaviour. The obtained formula reads:

$$\frac{d\Sigma}{d\Omega} = \left[\left(\frac{d\Sigma}{d\Omega}\right)_{TS} + \frac{\mathrm{G}\ \mathrm{erf}^{12}(1.06qR_g/\sqrt{6})}{1.5q^4R_g^4}\right]\exp\left(-\sigma^2q^2\right) + bkg \tag{2.61}$$

where R_g is the radius of gyration of single domains, and bkg is a background term [68].

2.2.6. Scattering from gels

In the section 2.1.1, we briefly discussed the phase behaviour of associating polymers. For HEUR polymers, which represent the polymer matrix of the nanocomposites investigated in this work, at polymer concentration $\phi > 4$ wt % in aqueous solution, and extended network is formed (Fig. 2.2). This phase is defined as *gel*. In the following paragraphs, we will use the term *hydrogel* for defining the gel composed of HEUR polymers, since it is a network composed of hydrophilic polymer chains. A gel is a system composed of crosslinked polymer network and solvent. In the case of the gel network composed of HEUR polymers, the crosslinks are not covalent bonds, but rather micellar cores formed by the hydrophobic ends of the HEUR chain. Therefore, the gel is a multicomponent system. When the components of the gel are compatible with each other, the polymer network spreads out into the solvent to maximize the entropy of mixing. On the other hand, when the components are incompatible, the network shrinks to minimize the surface energy. This volume reduction of the network is also caused by a change in temperature. It was found by Tanaka [70, 71] that a critical temperature for this kind of phase transition exists in gels, due to the existence of a *volume phase transition*. A typical example of such volume phase transition is the one occurring in poly(N-isopropyalacrylamide) (PNIPAM) gel in water [72, 73]. In a gel, the crosslinks are randomly distributed in the space. Therefore, inhomogeneities are created. Because of these inhomogeneities, in gels there are concentration fluctuations with polymer-rich and -poor domains. Scattering is a powerful technique to investigate these kind of inhomogeneities. The typical SANS profile of gels shows:

- high scattering intensity at low scattering vectors q
- a correlation peak, which is an indication of the microphase separation in gels. Unlike the microphase separation in block copolymers, microphase separation in gels does not have various morphologies. It is characterized by the repeat distance of the concentration fluctuations in the gel.

According to the Panyukov-Rabin theory (PR) on the scattering from gels [74], the high scattering intensity observed in the low q-range is due to the contribution of the structure factor to the scattering intensity. The structure factor of gels is a combination of two contributions, and it reads:

$$S(q) = G(q) + C(q) \tag{2.62}$$

where:

- $G(q)$ is the dynamic or thermal correlator

- $C(q)$ is the static correlator

The dynamic correlator $G(q)$ represents the thermal concentration fluctuations of the corresponding polymer solution. Its simplified expression follows the Orstein-Zernike formalism [66] which is a special case of the Teubner-Strey theory (eq. 2.53):

$$G(q) \sim I_{OZ} = \frac{I(0)}{1 + \xi_d^2 q^2} \tag{2.63}$$

with ξ_d being the correlation length of thermal density fluctuations. This contribution to the scattering intensity describes a homogeneous system. On the other hand, the static correlator $C(q)$ can be expressed in terms of the Debye-Beuche theory, which describes an inhomogeneous solid-like state [67]:

$$C(q) \sim I_{DB} = \frac{I(0)}{(1 + \xi_s^2 q^2)^2} \tag{2.64}$$

with ξ_d being the characteristic size of the inhomogeneities. This theory was used in the investigation of the mesoscopic structures of charged gels and their evolution on dehydration by Sugiyama and co-authors [75]. They found that, for a fully wet gel, the gel inhomogeneities are suppressed, and the contribution to the low-q scattering intensity is mainly due to the dynamic correlator contribution, $G(q)$. Decreasing the water content, a correlation peak is observed, indicating the presence inhomogeneities due to the randomly distributed crosslinks in the gel network. This interpretation of the gel structure evolution on dehydration was useful for the comparison between the structure of the hydrogel state and the one of dry state of the HEUR-MNPs nanocomposites investigated in this work.

2.3. Polymer dynamics

In the present work both, the structure and the dynamics of HEUR-MNPs nanocomposites are investigated. We will now introduce some basic theory about polymer dynamics which are relevant for the interpretation of the results obtained from the dynamic characterization of the investigated systems.

2.3.1. Polymer dynamics at different length scales

Dynamic processes in polymers occur over a wide range of length and time scales. The different temperature ranges, with the corresponding length scales, in which we can observe different kinds of polymer dynamics, are shown in Fig. 2.24.

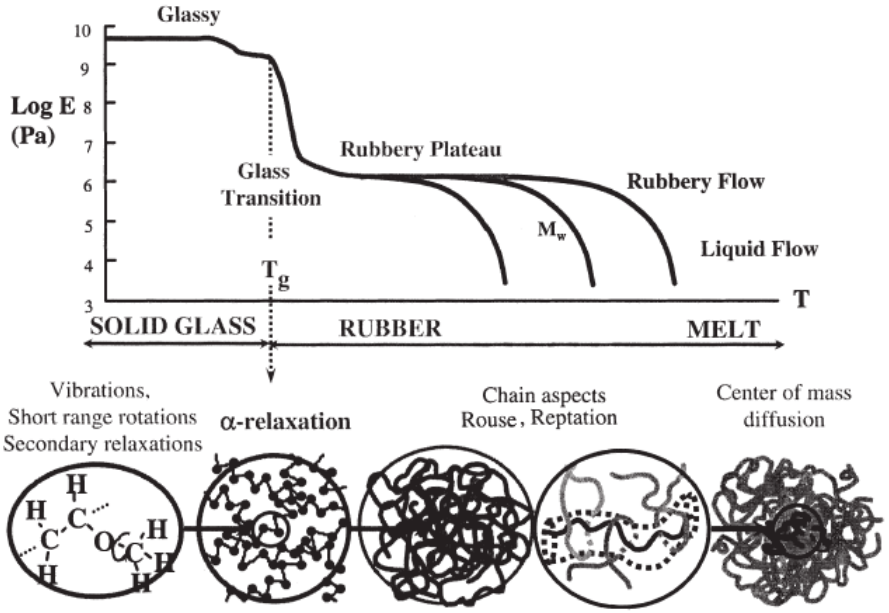

Figure 2.24.: Dynamic modulus in a bulk polymer as a function of the temperature and its molecular origin [76]

We can distinguish four different temperature regimes in which we observe different kinds of dynamics involving various entities:

- At low temperatures, the system is the glassy state and therefore, only small amplitude motions, like vibrations and rotations, are possible. The so-called *secondary relaxations* also occur in this temperature range. These are defined as motions which involve only small portions of the polymer chain, like side groups or small sequences of monomers. They are called with Greek letters from β to δ depending on the size of the moving group.

- At the glass transition temperature, T_g, the system undergoes the phase transition from the glassy state to the liquid state, and it can flow. This allows the motion of the whole polymer chain. It is a cooperative motion involving all the monomers of the chain and it is called *primary* relaxation or α-relaxation.

- Increasing the temperature, we observe large scale motions of the system. These relaxations are limited by confinement effects caused by mutually interpenetrating chains.

- Further increasing the temperature, rubbery flow sets in. The chain has lost the memory of its initial state and the associated characteristic relaxation time is defined as *normal mode*, which is the relaxation of the end-to-end vector of a given chain (Fig. 2.25).

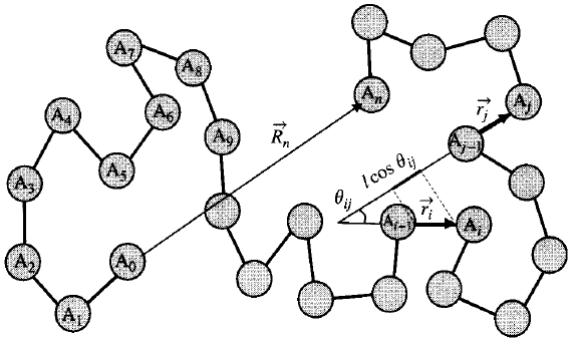

Figure 2.25.: Conformation of a flexible chain with $\vec{R}_n$ being the end-to-end vector. The bond vector $\vec{r}_i$ goes to atom A_{i-1} to atom A_i, and $\vec{r}_j$ goes to atom A_{j-1} to atom A_j. The angle between the vectors $\vec{r}_i$ and $\vec{r}_j$ is θ_{ij} [40]

Then, the rubbery flow passes over the liquid flow which is characterized by the translational diffusion coefficient of the chain [76].

2.3.2. Relaxation processes in polymers

In Fig. 2.24 the polymer dynamics at different temperatures and length scales is shown. At temperatures above the glass transition temperature T_g, the dynamic modulus decreases and the system starts to flow. At this temperature, amorphous materials (or amorphous regions within semi-crystalline materials) undergo a change from a hard and relatively brittle "glassy" state into a molten or rubber-like state, as the temperature is increased. The main difference between the glass transition and melting can be visualized in Fig. 2.26.

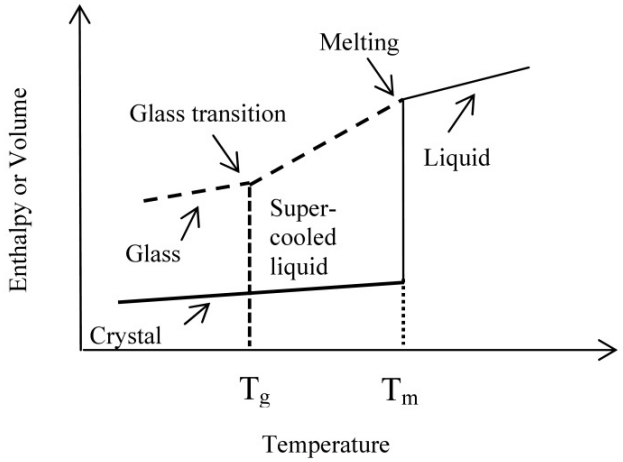

Figure 2.26.: Enthalpy or Volume as a function of the temperature for a crystal and for an amorphous material (glass). The melting point and the glass transition are shown as T_m and T_g respectively

As seen in Fig. 2.26, when a crystalline polymer, or a crystal, melts, it absorbs a certain amount of heat, which is called the *latent heat of melting*, and it undergoes a change in its heat capacity. This change is defined as a *first order transition*, where there is a transfer of heat between system and surroundings and the system undergoes an abrupt volume (or enthalpy) change. On the other hand, when a glass (or an amorphous polymer) melts, the temperature increases at a rate determined by the polymer's heat capacity, as for the melting. However, when the T_g is reached the temperature keeps rising, unlike the case of melting, meaning that there is no *latent heat of glass transition* and the temperature further increases but with a different rate as at $T < T_g$. This is due to the fact that the polymer undergoes an increase of its heat capacity. The glass transition is defined as a *second-order transition*, because there is no transfer of heat, but the heat capacity does change. The volume changes to accommodate the increased motion of the wiggling chains, and, unlike the melting case, it does so continuously. Semi-crystalline polymers undergo both glass transition and melting. The glass transition temperature T_g gives

hints about the dynamics of polymer chains, and in particular, how easily they can move. In particular, higher is the T_g, less mobile are the polymer chains, while the more easily a polymer can move, the less heat it takes for the chains to commence wiggling and break out of the rigid glassy state into the soft rubbery state, and therefore the T_g is low. It is customary to label relaxation processes in polymers as α, β, γ and so on in decreasing order of temperature. The polymer motion associated to the glass transition is called *dynamic glass transition* or, more often, α-relaxation. It is defined as the *primary* relaxation in polymers as it is a cooperative motion that involves the whole chain, while the relaxations occurring at temperatures below the T_g are defined as *secondary* relaxations. The *secondary* relaxations involve small portions of the polymer chain, as side groups or small sequences. Not all the polymers show all the *secondary* relaxations. For instance, only polymers with polar side groups or polar segments as carbonyl groups, show a β-relaxation. The relaxation times τ associated to the *primary* and *secondary* relaxations, show a different kind of temperature dependence [77]. The relaxation times associated to the *secondary* relaxations, such as β, γ and δ, depend on the temperature according to the Arrhenius law [78]:

$$\tau = \tau_0 \exp\left(-\frac{E_A}{k_B T}\right) \tag{2.65}$$

where τ_0 is the fastest relaxation time for $T \to \infty$, and E_A is the energy barrier associated to the relaxation process. The Arrhenius law cannot explain the temperature dependence of the α-relaxation. The explanation of its non-Arrhenius behaviour has proven to be a difficult task: there are numerous competing theoretical models of the glass transition which describe the observed behaviour with various level of precisions [79] [80] [81]. Thus, most experimentalists revert to phenomenological approaches and the most prominent one is the Vogel-Fulcher-Tammann-Hesse equation [82]:

$$\tau = \tau_0 \exp\left(-\frac{B}{T - T_{VF}}\right) \tag{2.66}$$

where B is a parameter corresponding to the hindering barrier for the Arrhenius case (i.e. T_{VF}). The non-Arrhenius behaviour is taken into account by introducing the Vogel-Tammann temperature T_{VF} which is 30-40 °C below the glass transition temperature. This temperature dependence is typical of cooperative processes. Nowadays, eq. 2.66 is used in the form proposed by Angell [83], replacing B by DT_{VF}. The strength parameter D can be taken as a measure of the deviation from the Arrhenius behaviour and it is related to the fragility of the material [84]. In particular, the higher B is, the more fragile the material is. The comparison between eq. 2.65 and eq. 2.66 reveals that the relaxation time increases much faster with decreasing the temperature, for the *secondary*

processes than for the α-relaxation. The investigation of the temperature dependence of the relaxation processes in polymers is crucial for their identifications.

2.3.3. Dynamics of polymers in solution: the Zimm model

The first model of polymer dynamics was developed by Rouse, and it describes the dynamics of unentangled polymers in melts [85]. Afterwards, it was used for the study of the dynamics of entangled polymer solutions [86]. In this model, the polymer chain is represented as N beads connected by springs of root-mean-square size b. The beads only interact with each other through the connecting springs. Therefore, the *Rouse model* ignores hydrodynamic interaction forces, which are long-range forces acting on solvent arising from the motion of a particle in solution. This assumption is reasonable for polymer melts, but it is not correct for polymer in diluted solutions. In this case, hydrodynamic interactions between monomers within the polymer chain and between monomers and the solvent within the pervaded volume of the chain, are strong. For this reason, the best model for the dynamics of polymers in solution is the *Zimm model*, which treats the pervaded volume of the chain as a solid object moving through the surrounding solvent. The pervaded volume is the volume of solution spanned by the polymer chain. It is proportional to the size of the polymer chain R:

$$V \approx R^3 \tag{2.67}$$

Considering that the chain drags with it the solvent in its pervaded volume, then it moves as a solid object of size:

$$R \approx bN^{\nu} \tag{2.68}$$

with b being the root-mean-square size of the ideal springs which connect N beads (according to the Rouse model [85]), which resembles the number of monomers, and ν is the reciprocal of the fractal dimension of the polymer. The friction coefficient of the chain of size R being pulled through a solvent of viscosity η_s is given by the Stokes law [87]:

$$\zeta_Z \approx \eta_s R \tag{2.69}$$

From the Einstein relation [87] the diffusion coefficient of a chain in the Zimm model reads:

$$D_z = \frac{kT}{\zeta_Z} \approx \frac{kT}{\eta_s R} \approx \frac{kT}{\eta_s b N^{\nu}} \tag{2.70}$$

In the Zimm model, the chain diffuses a distance of the order of its own size during the Zimm time τ_Z:

$$\tau_Z \approx \frac{R^2}{D_Z} \approx \frac{\eta_s R^3}{kT} \approx \frac{\eta_s b^3}{kT} N^{3\nu} \approx \tau_0 N^{3\nu} \tag{2.71}$$

The full expression of the diffusion coefficient was calculated by Zimm in 1956 [88]:

$$D_z = \frac{8kT}{3\sqrt{6\pi^3}\eta_s R} \tag{2.72}$$

The chain relaxation time calculated by Zimm reads:

$$\tau_z = \frac{\eta_s}{2\sqrt{3\pi}kT} R^3 \tag{2.73}$$

In principle, a chain in a diluted solution could move a distance of order of its size by Rouse motion, by Zimm motion, or a combination of the two. Comparing the eq. 2.71 with the Rouse relaxation time for polymer melts [85], we observe that the Zimm time is shorter than the Rouse time. In fact, in diluted solutions, the Zimm motion has less frictional resistance than the Rouse motion, and therefore, the faster process is the Zimm motion.

2.3.4. Neutron scattering for the investigation of polymer dynamics

In order to study the dynamics of glass forming materials like polymers, that occur on wide time scales, it is necessary to combine different techniques. Neutron scattering is a powerful tool to investigate polymer dynamics. In the paragraph 2.2.2 we defined the scattering cross section in eq. 2.22. It is important to consider that the expression for the scattering cross section of eq. 2.22 depends only on the scattering vector $\mathbf{q}$ and it is therefore valid for a *static* neutron scattering experiment. The link between the scattering cross section and the real space is given by the fact that, in general, the scattering intensity measured in a *static* neutron scattering experiment is the Fourier transform of the spatial correlation function of the scattering length density. It was defined by Debye and Bueche in 1949 [67]:

$$\gamma(\mathbf{r}) = \frac{1}{V} \int_V \rho(\mathbf{r}')\rho(\mathbf{r}+\mathbf{r}')d\mathbf{r}' \tag{2.74}$$

The scattering intensity $I(\mathbf{q})$ is given by:

$$I(\mathbf{q}) = \int_V \gamma(\mathbf{r}) \exp(-i\mathbf{q}\mathbf{r}))d\mathbf{r} \tag{2.75}$$

On the other hand, in a *dynamic* scattering experiment, the double differential cross section is measured:

$$\frac{d^2\sigma}{d\Omega d\omega} = N\frac{k_f}{k_i}[(\langle b^2\rangle - \langle b\rangle^2)S_{inc}(\mathbf{q},\omega) + \langle b\rangle^2 S_{coh}(\mathbf{q},\omega)] \tag{2.76}$$

with N being the number of atoms in the sample, k_i and k_f the incident and final scattering vectors during the scattering event and b the scattering length, which is characteristic for each nucleus. The scattering functions $S_{inc}(\mathbf{q},\omega)$ and $S_{coh}(\mathbf{q},\omega)$ provide a direct link to the microscopic motion of the atoms. The coherent scattering function gives information about the inter-particle correlation and their time evolution. The Fourier transform of the frequency-dependent scattering function $S(\mathbf{q},\omega)$ is the so-called *intermediate scattering function* $S(\mathbf{q},t)$:

$$S(\mathbf{q},t) = \frac{1}{2\pi}\int_{-\infty}^{\infty} S(\mathbf{q},\omega)\exp(i\omega t)d\omega \tag{2.77}$$

As the static scattering intensity $I(\mathbf{q})$ depends on the spatial correlation function (eq. 2.75), the *intermediate scattering function* depends on the time-dependent van Hove correlation function $G(\mathbf{r},t)$:

$$S(\mathbf{q},t) = \int G(\mathbf{r},t)\exp(-i\mathbf{q}\mathbf{r})d\mathbf{r} \tag{2.78}$$

In the classical picture, the van Hove correlation function can be expressed in terms of the atomic positions:

$$G(\mathbf{r},t) = \frac{1}{N}\left\langle \int d^3\mathbf{r}' \sum_{i,j}\delta(\mathbf{r}-\mathbf{r}'+\mathbf{r}_j(t))\delta(\mathbf{r}'-\mathbf{r}_i(0))\right\rangle \tag{2.79}$$

Therefore, the van Hove correlation function can be classically interpreted as the probability density for finding an atom at time t at a distance $\mathbf{r}$ from the position of an atom at time 0. For this correlation function it does not matter whether both atoms are the same or not. Therefore, also the intermediate scattering function of eq. 2.77 can be expressed in terms of the atomic coordinates:

$$S(\mathbf{q},t) = N^{-1}\sum_{i=1}^{N}\sum_{j=1}^{N}\langle\exp(-i\mathbf{r_i}(0)\mathbf{q})\exp(i\mathbf{r_j}(t)\mathbf{q})\rangle \tag{2.80}$$

It is usually expressed in the normalized form $S(q,t)/S(q,0)$, whereas $S(q,0)$ is the static scattering function (at t = 0):

$$S(\mathbf{q},t=0) = N^{-1}\sum_{i=1}^{N}\sum_{j=1}^{N}\langle\exp(-i\mathbf{r_i}(0)\mathbf{q})\exp(i\mathbf{r_j}(0)\mathbf{q})\rangle \tag{2.81}$$

The coherent scattering function $S_{coh}(\mathbf{q},\omega)$ can be written in terms of the classical expression of the van Hove function:

$$S_{coh}(\mathbf{q},\omega) = \frac{1}{2\pi N}\int dt \left\langle \sum_{i,j} \exp(i(\mathbf{q}(\mathbf{r}_j(t) - \mathbf{r}_i(0)) - \omega t)) \right\rangle \tag{2.82}$$

It is important to consider that many polymer problems depend on the structure and dynamics in a *mesoscopic regime*. In this case, a description in terms of atomic coordinates $\mathbf{r}$ is not adequate. Rather a coarse-grained description in terms of scattering length density $\Delta\rho(\mathbf{r},t)$ is used. Thus, a molecular unit of type j is selected and the sum of the scattering lengths of the contained atoms is related to the effective volume V of this unit, $\rho_j = \sum_{i,j} b_i/V$. The same has to be done with the solvent. The scattering in the low q-regime only depends on the scattering length density difference, the contrast $\Delta\rho(\mathbf{r},t) = \rho_{polymer} - \rho_{solvent}$. The related time dependent scattering function is therefore given by:

$$S(q,t) = \int \langle \Delta\rho(\mathbf{r},t)\Delta\rho(\mathbf{r}',0)\rangle \exp(i\mathbf{q}(\mathbf{r}-\mathbf{r}'))d^3r \tag{2.83}$$

The corresponding small angle neutron scattering (SANS) intensity, defined in the eq. 2.27, is proportional to $S(q,t=0)$.
The coherent scattering function is what is exactly probed in an inelastic neutron scattering experiment. In the investigation of polymer dynamics it gives information about the time evolution of the motion of a single polymer chain, or of segments of it, respect to the other chains. In many polymer problems, the intermediate scattering function in its normalized form, $S(q,t)/S(q,0)$, can be expressed in terms of the Kohlrausch-Williams-Watts (KWW) function, or *stretched exponential* function $F(q,t)$ [76]:

$$S(q,t)/S(q,0) = A\exp\Big[-(\Gamma t)^{\beta}\Big] \tag{2.84}$$

where A is a constant and the KWW function $F(q,t)$ reads:

$$F(q,t) \sim \exp\Big[-(\Gamma t)^{\beta}\Big] \tag{2.85}$$

where $\Gamma = 1/\tau$ is defined as the relaxation rate, with τ being the relaxation time, or decaying time of the normalized intermediate scattering function, β is the stretching exponent, being 0.85 and 1 for the Zimm single chain motion (in the limit of short time scales) and for collective diffusion, respectively.

For completeness we introduce the incoherent scattering function, which is related to the self correlation function by:

$$S_{incoh}(\mathbf{q},\omega) = \frac{1}{2\pi}\int d^3r \int dt \exp(i(\mathbf{qr} - \omega t))G_s(\mathbf{r},t) \tag{2.86}$$

with $G_s(\mathbf{r},t)$ being:

$$G_s(\mathbf{r},t) = G(\mathbf{r},t) = \frac{1}{N}\left\langle \int d^3\mathbf{r}' \sum_i \delta(\mathbf{r}-\mathbf{r}'+\mathbf{r}_i(t))\delta(\mathbf{r}'-\mathbf{r}_i(0)) \right\rangle \tag{2.87}$$

This function is the probability density of finding an atom at time t in a distance $\mathbf{r}$ from its *own* position at time 0. Therefore, the incoherent scattering function can be written like:

$$S_{incoh}(\mathbf{q},\omega) = \frac{1}{2\pi N}\int dt \left\langle \sum_i \exp(i(\mathbf{q}\Delta\mathbf{r}_i(t) - \omega t)) \right\rangle \tag{2.88}$$

3. Characterization methods

In this chapter the experimental techniques employed in this work are presented. They are divided by characterization type. In particular, we first describe the techniques used for the structural characterization of the HEUR-MNPs nanocomposites and then the ones used for the investigation of their dynamics. We describe the basic principles and the experimental set up of each experimental technique.

3.1. Structural characterization

In this section all the experimental methods empolyed for the structural investigation of the HEUR-MNPs nanocomposites are described. The discussion begins with the description of small angle neutron scattering (SANS) for the investigation of the inner structure of the investigated systems, and it concludes with transmission electron microscopy (TEM) which investigates their surface structure. Finally, in a separate section (section 3.1.3), the physical property measurement system (PPMS) for the investigation of the magnetic properties of the nanocomposites is explained.

3.1.1. Small angle neutron scattering (SANS)

Small angle neutron scattering (SANS) is a powerful technique for the structural investigation of the soft matter. Typically, it is employed for the investigation of structures on length scales between 10 Å and 10000 Å. This range of real space lengths corresponds to a scattering vector of magnitude between 10^{-1} $Å^{-1}$ and 10^{-4} $Å^{-1}$. In order to observe scattering events under reasonable scattering angles, one chooses a rather long wavelength, according to the eq. 2.16. Therefore, typically neutrons of wavelength between 5 and 15 Å are used for SANS. The basic principles of a scattering experiments and the scattering theory are explained in the chapter 2, paragraph 2.2.2. We now focus on the description of the SANS experimental set up and on the data treatment used in this work.

Experimental setup

The SANS instrument used in this work is called *KWS1* and it is located at the research reactor FRM-II (20 MW nominal thermal power) of the Technische Universität München (TUM) in Garching (Germany) and operated by the Jülich Center for Neutron Science (JCNS). There, the cold neutron source consists of liquid deuterium with a temperature of 25 K. A scheme of the instrument with all the components is shown in Fig. 3.1.

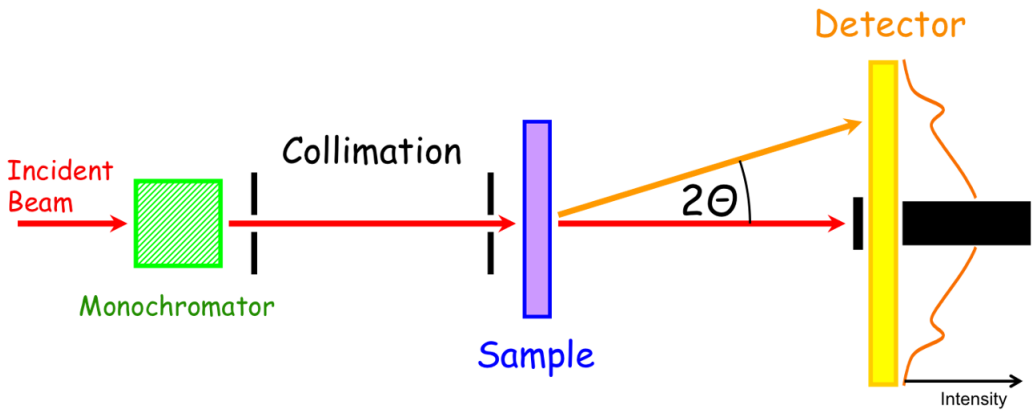

Figure 3.1.: Sketch of the KWS1 instrument at research reactor FRM-II showing all the components: the monocromator, the sample and the detector with the beam-stop (black rectangle), which absorbs the transmitted beam

The wavelength band of the incident neutron beam is selected by the so-called *velocity selector*, which is shown in the picture in Fig. 3.2.

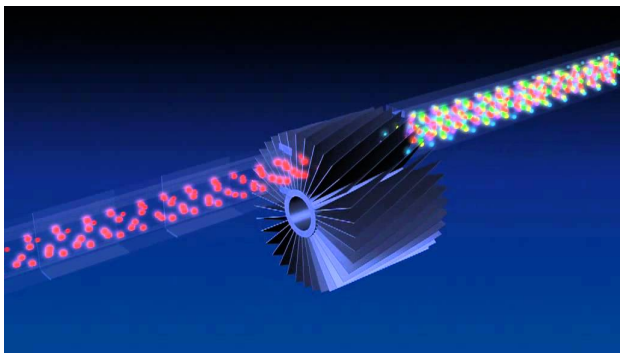

Figure 3.2.: Velocity selector drum of SANS instruments. Neutrons with a specific velocity are selected by the tilted lamellae made of a neutrons absorbing material (Mg-Li alloy)

In Fig. 3.2 it is possible to observe the screw-like twisted channels of the velocity selector drum. They are separated by absorbing walls, which only neutrons of a certain wavelength can pass through when the drum is turning.

Covered q-range	$q = 0.0007$ – 0.5 Å^{-1}
Velocity selector	Dornier, FWHM 10 %, $\lambda = 4.5$ Å – 12 Å, 20 Å
Sample aperture	rectangular 1×1 mm^2 – 50×50 mm^2
Neutron lenses	MgF_2, diameter 50 mm, curvature 20 mm packs with 4, 6, 16 lenses
Detector 1	^6Li-Scintillator 1 mm thick + Photomultiplier Efficiency > 95 %

Table 3.1.: Specifications of the small angle neutron scattering instrument KWS1

The incident wave vector of the neutron beam k_I, is defined by two distant apertures of comparable size. The longer is the distance between the diaphragms, the higher is the collimation for a given cross section of the beam. The sample is placed next to the second aperture and the scattered neutrons are recorded on a detector which is at a large distance from the sample. Typically, the sample-detector distance is comparable with the collimation distance. The overall length of such an instrument can amount to 40 m up to 80 m. The main features of the instrument are reported in Tab. 3.1.

Data treatment

In a SANS experiment the intensity scattered by the sample, I_s, is measured. Once it is measured, we have to related it to the structure of the sample. This is done comparing the incident intensity I_i and the scattered intensity I_s, measured at an angle θ and a distance L on a detector with area $A_{det} = \Delta\Omega L^2$. The ratio of both intensities is defined as the differential scattering cross section, defined in eq. 2.17:

$$\frac{I_s}{I_i}\frac{L^2}{A_{det}}\frac{1}{T} = \frac{d\sigma}{d\Omega} \tag{3.1}$$

where T is the sample transmission. If we normalize the *scattering cross section* for the sample volume we obtain the *macroscopic scattering cross section* already defined in eq. 2.23. It is the quantitative representation of the interaction radiation-sample and contains all the information on the structure and interaction in the sample. The macroscopic scattering cross section and the measured intensity I are connected by:

$$I = I_i D_e \Delta\Omega A T d \left(\frac{d\Sigma}{d\Omega}\right) \tag{3.2}$$

with D_e being the detector efficiency, A the irradiated sample area, d the sample thickness, T the sample transmission and $\Delta\Omega$ the angle of one detector element. The measured intensity at the detector has to be corrected from errors induced by the instrument and by the background. The first correction that has to be done is the *absolute calibration*. A material with a flat cross section is used for the absolute calibration. For this aim, usually plexyglass is used. The measured intensity is normalized with the one of the reference:

$$\left(\frac{d\Sigma}{d\Omega}\right)_s = \frac{I_s}{I_{pl}}\frac{L_s^2}{L_{pl}^2}\frac{d_{pl}}{d_s}\frac{T_{pl}}{T_s}\left(\frac{d\Sigma}{d\Omega}\right)_{pl} \tag{3.3}$$

with s and pl being the indices for the sample and the *plexyglass* respectively and assuming that $\Delta\Omega = A_{det}L^{-2}$ with $A_{det} = const$ (with A_{det} being the area of the detector).

The calibration constant is defined as:

$$\mu_{pl} = d_{pl}T_{pl}\left(\frac{d\Sigma}{d\Omega}\right)_{pl} \tag{3.4}$$

Therefore, the scattering cross section of the sample (eq. 3.3) can be written as:

$$\left(\frac{d\Sigma}{d\Omega}\right)_s = \frac{\mu_{pl}}{C}I_s \tag{3.5}$$

with $C = I_{pl}T_s d_s L_{pl}^2/L_s^2$. It is important to consider that also the sample cell contributes to the scattering intensity. This error can be corrected by measuring the intensity of the empty cell and subtracting it from the sample measurement. Therefore, the measured scattering intensity from the sample is given by:

$$\left(\frac{d\Sigma}{d\Omega}\right)_s = \frac{\mu_{pl}}{C}\frac{I_s - I_{ec}(T_s/T_{ec})}{I_{pl} - I_{ec}(T_{pl}/T_{ec})} \tag{3.6}$$

with the index ec indicating the empty cell. After the absolute calibration the scattering intensity collected at the detector will be a 2-dimensional image function of the angle θ that is converted in a function of the scattering vector q. Another important correction to the measured intensity regards the *resolution effects*. The limited resolution of the detector leads to smearing of the measured intensity. This effect has to be taken into account in the measured intensity. At $q = q_0$ the resolution effect are included in the scattering intensity:

$$I(q_0) = \int R(q, q_0)\frac{\Sigma(q)}{d\Omega}dq \tag{3.7}$$

where $R(q, q_0)$ is the distribution function of the scattering vectors q around the nominal value q_0. For radially averaged data it reads:

$$R(q, q_0) = \frac{q}{\sigma_{q_0}^2}\exp\left(-\frac{q^2 + q_0^2}{2\sigma_{q_0}^2}\right)I_0\left(\frac{qq_0}{\sigma_{q_0}^2}\right) \tag{3.8}$$

where I_0 is the modified Bessel function. It takes into account the wavelength spread $(\Delta\lambda/\lambda)$, finite collimation $(\Delta\beta)$ and the detector resolution (ΔQ_D) through $\sigma_{q_0}^2$:

$$\sigma_{q_0}^2 = \frac{1}{8\ln 2}\left[(q_0\Delta/\lambda)^2 + (k_0\Delta\beta)^2 + (k_0\Delta Q_D)^2\right] \tag{3.9}$$

The parameter β is defined as:

$$\Delta\beta = \begin{cases} 1, & \frac{2r_1}{L} - \frac{r_2^2(l+L)^2}{2r_1 l^2 L}\alpha_1 \geq \alpha_2 \\ 0, & 2r_2\left(\frac{1}{L}+\frac{1}{l}\right) - \frac{r_1^2 l}{2r_2 L(L+1)}\alpha_1 < \alpha_2 \end{cases} \tag{3.10}$$

where L and l are the distances from the source to the sample and from the sample to the detector respectively, r_1 is the radius of the source aperture and r_2 is the radius of the sample aperture. The angles are $\alpha_1 = r_1/(L+l)$ and $\alpha_2 = r_2/l$. At low q-values, the resolution is mainly due to the contribution from the spread in scattering angles, whereas, at high q-values, it is mainly due to the wavelength spread.

SANS for the structural characterization of the HEUR-MNPs nanocomposites

Small angle neutron scattering (SANS) was employed for the structural characterization of the novel HEUR-MNPs nanocomposites in two different morphologies: as dry films and as hydrogels. We also performed SANS measurements on hydrogels containing only the HEUR polymer at increasing polymer concentration, in order to investigate the phase behaviour of the pure polymer matrix. SANS measurements on the nanocomposites in both states and on the pure polymer matrix were performed on the SANS diffractometer $KWS1$ at JCNS in Garching [89]. The scattering patterns were recorded in the range of scattering vector q between 0.0017 and 0.22 $Å^{-1}$ using a neutron wavelength of 4.7 Å ($\pm$ 5 %). We measured the HEUR solutions and the hydrogel nanocomposites using D_2O as solvent in order to avoid recording the high incoherent scattering of H_2O. All 2-dimensional intensity profiles were radially averaged, corrected for transmission, thickness, and background, and presented in absolute scales using a secondary plexiglass standard. Concerning the structural characterization of the polymer matrix, we analyzed 8 HEUR solutions with increasing polymer concentration, ϕ_{poly}: 0.46 wt %, 0.92 wt %, 1.4 wt %, 1.8 wt %, 5 wt %, 10 wt %, 15 wt % and 25 wt %. The samples at high polymer concentrations ($\phi_{poly} > 1.8$ wt %) were in a gel-like phase and therefore they exhibited high viscosity. We used a polymer concentration of ϕ_{poly}= 25 wt % to prepare the polymer matrix of the nanocomposites in the hydrogel phase. We analyzed nanocomposites, in the hydrogel and in the dried state, with increasing MNP concentration: 0.23 wt %, 0.46 wt %, 1 wt % and 3 wt %.

3.1.2. Transmission electron microscopy (TEM)

Transmission electron microscopy (TEM) is a microscopy technique which uses an electron beam as probe. It is transmitted through an ultra-thin specimen, interacting with it as it passes through it. Historically, TEM was developed because of the limited image resolution in light microscopes, which is imposed by the wavelength of visible light. The resolving power of an optical system can be defined as:

$$R = \frac{\lambda}{2NA} \tag{3.11}$$

where R is the distance between distinguishable points, λ is the wavelength of the illumination source and NA is the "numerical aperture", which is a measure of the quality of the objective lens. The resolution in the visible-light microscope considering the blue light source (λ= 436 nm) is R=155 nm. In the case of the electron microscope, considering an electron source of 120 keV with λ= 0.00335 nm, the resolution is R=0.17 nm. Therefore, with TEM it is possible to investigate the matter at much shorter length scales that with the visible-light microscope. However, TEM microscopy has some disadvantages, first of all the low penetrating power of the electron beam. This limitation requires that the samples investigated through TEM must be very small (up to 3 mm of diameter) and thin (<500 nm). The electron beam current in a TEM experiment can be as high as $\approx 0.1 - 1\mu$A which corresponds to $\approx 10^{12}$ electrons passing through the specimen plane. The basic characteristics of the electrons are summarized in the table 3.2.

Charge (e)	(-) = 1.602 10^{-19} C
1 eV	1.602 10^{-19} J
Rest mass (m_0)	9.109 10^{-31} kg
Rest energy (m_0c^2)	511 keV
Kinetic energy (charge × voltage) 1	1.602 10^{-19} N m (for 1 volt potential)= J

Table 3.2.: Basics characteristics of electrons

The basic principle of TEM is the interaction of the electron beam with the thin specimen and it is illustrated in Fig 3.3. The specimen is illuminated with a broad beam of electrons in which the intensity is uniform over the illuminated area. The electrons which hit the specimen are called the *incident beam* and those scattered are called *scattered beams*. The electrons coming through the thin specimen are therefore separated in those that suffer no angular deviations, called *direct beam*, and those scattered through measurable angles (the *scattered beams*). As the electrons pass through the specimen they are either scattered by a variety of processes or they remain unaffected. The end result is that a non-uniform distribution of electrons, which contains all the structural and chemical properties of the specimen, emerges from the exit surface of the specimen.

As illustrated in Fig. 3.3, TEM is constructed to display this not uniform distribution of electrons in two ways: first, as the *spatial distribution* of scattering, which can be observed as contrast in images of the specimen (Fig. 3.3 A)), or as the *angular distribution* of scattering (Fig. 3.3 B)). By using an electron detector, of a size such that it only selects electrons that have suffered more or less than a certain angular deviation, it is possible to choose which electrons to detect and, therefore, which information to obtain for the specimen [90]. In the present work, we used the first TEM-mode, in order to obtain the TEM images of our samples.

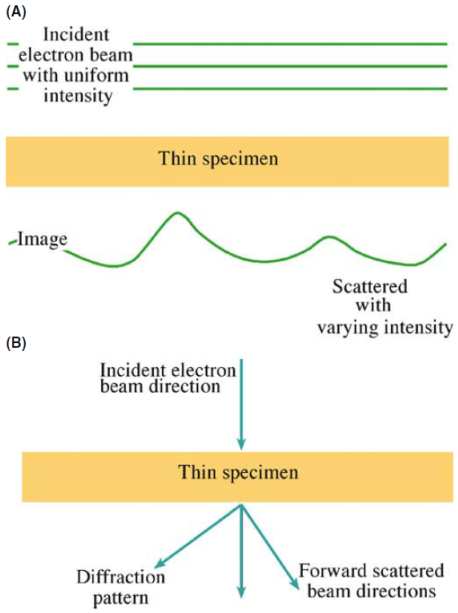

Figure 3.3.: A) Uniform intensity of electrons falls on a thin specimen. Scattering within the specimen changes both the spatial and angular distributions of the emerging electrons. The spatial distribution is depicted as a wavy line. B) The change in the angular distribution is shown by an incident beam of electrons being transformed into several forward-scattered beams [90]

Experimental setup

In Fig. 3.4 a detailed scheme of a typical electron microscope is shown. The main components are:

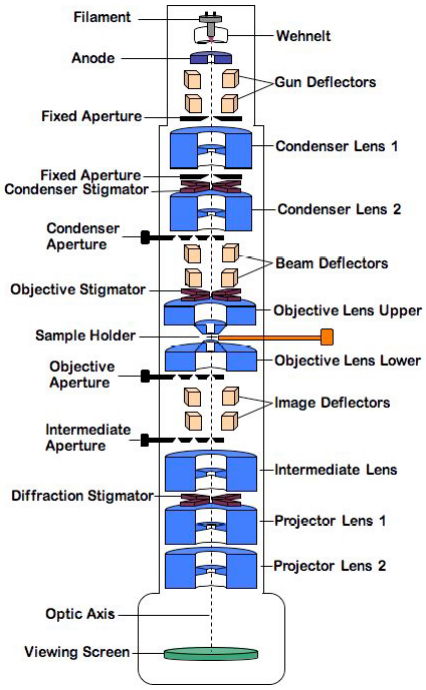

Figure 3.4.: Scheme of a generic transmission electron microscope showing all its components [90]

- an electron gun, which produces the electron beam, and the condenser system, which focuses the beam onto the object. The electron gun contains usually a tungsten filament or a small lanthanum-hexaboride (LaB_6) crystal. These materials have high melting temperature and a low work function that allows the produced electrons to escape when heated, by passing high current through the filament. At temperatures of $\approx 1500°$, electrons are emitted from the tip. The emitted electrons are accelerated and sent through the column by the anode. Between the filament, being the cathode, and the anode, is set a potential between 20 and 1000 kV.

- the image-producing system, consisting of the objective lens, movable specimen stage, and intermediate and projector lenses, which focus the electrons passing through the specimen to form a real, highly magnified image. The lenses in TEM are electromagnetic. A toroidal coil of wire surrounds the optic axis, generating a magnetic field when a current passes through the coil. By changing the amount of current in the coil, the strength of the lens can be adjusted, allowing a large

range of operating conditions. In general, the lenses in the TEM instrument can be divided into three groups: (i) the condenser lenses which illuminate the sample (ii) the objective lenses which form the image and (iii) the projector lenses which magnify the image.

- the image-recording system, that converts the electron image into some form perceptible to the human eye. In particular, the image is viewed on a phosphor-coated metal plate that fluoresces visible light-photons when hit by electrons.

Numerous deflectors (gun, beam and image reflectors in Fig. 3.4 are located at various points on the column to keep the electron beam as straight as possible along the center line of the column (*optic axis*).

TEM measurements on the investigated systems

Transmission electron microscopy (TEM) was employed in this work for two main purposes: i) to obtain the shape and the size distribution of the MNPs and ii) to observe the distribution of the MNPs in the polymer matrix in the dry films. In order to achieve the purpose i), both types of the MNP solutions (hydrophobic and hydrophilic) used for the preparation of the HEUR-MNPs nanocomposites as hydrogels, were investigated. Samples for TEM were prepared by placing a drop of the 2.3 g/L solution on a carbon-coated copper grid. After a few seconds, the excess solution was removed by blotting with filter paper. The nanocomposites in the dried state were also investigated with TEM. In this case samples for TEM were prepared by depositing the powder sample on a carbon-coated copper grid. After a few minutes, excess powder was carefully removed. In both investigations, the specimen was inserted into a high-tilt-specimen retainer (EM-21311HTR, JEOL, Tokyo, Japan) and transferred to a JEM 2200 FS EFTEM instrument (JEOL, Tokyo, Japan). Examinations were carried out at room temperature. The transmission electron microscope was operated at an acceleration voltage of 200 kV. Zero-loss filtered images were recorded digitally by a bottom-mounted 16 bit CCD camera system (FastScan F214, TVIPS, Munich, Germany).

3.1.3. Magnetic properties: physical property measurement system (PPMS)

The physical property measurement system is an instrumental equipment which allows the measurements of physical properties of materials, such as electrical and magnetic properties. In particular, it can be used for magnometry applications, therefore, for measuring the magnetization as a function of the applied field H and of the temperature T. For this kind of application, it is first of all important to control the applied magnetic field and the temperature. The applied magnetic field can be varied between -9 and +9 T. The field axis is hereby always longitudinal to the axis of the probed magnetic moment. To control the temperature, a vacuum pump draws helium from the liquid helium reservoir producing a gas flow around the sample chamber in the so-called cooling annulus. In the cooling annulus heaters warm the gas to the correct temperature. The possible temperature range spans between 1.9 and 400K. A sketch of the temperature control system in shown in Fig. 3.5

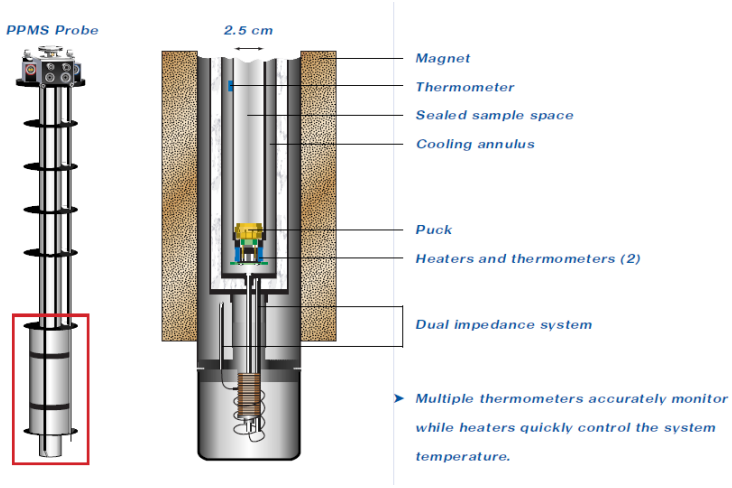

Figure 3.5.: Scheme of the temperature control of the PPMS systems. All the components are shown in the figure

In order to perform magnetic measurements, the PPMS system is often used in the *vibrating sample magnometer* (VSM) configuration. This configuration uses a linear motor to vibrate the sample. The sample is oscillated near a detection coil and synchronously, the voltage induced is detected. The oscillation amplitude is typically $\approx 1-3$ nm and the oscillation frequency is 40 Hz. This system is able to resolve a magnetization change in the sample of less than 10^{-6} emu at a data rate of ca. 1Hz. The VSM option for the PPMS instrument is schematically shown in Fig. 3.6

The sample is attached at the end of a sample rod that is driven sinusoidally by the

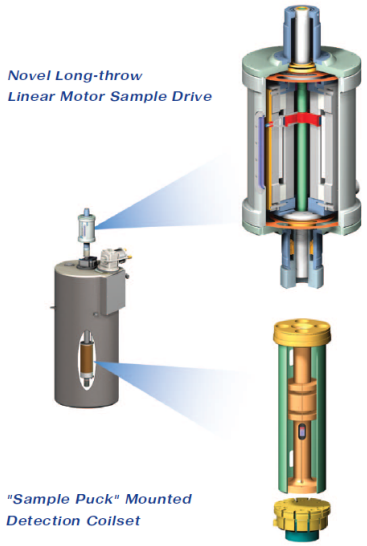

Figure 3.6.: Scheme of the VSM set up

VSM motor. The center of oscillation is positioned at the vertical center of a gradiometer pickup coil.

Magnetic response measurements on the HEUR-MNPs nanocomposites in the dried state

The magnetic response measurements were carried out on the HEUR-MNPs nanocomposites as dry films with different MNP concentration: 0.23 wt %, 0.46 wt %, 1 wt % and 3 wt % . The measurements were performed using the Physical Property Measurement System (PPMS) from Quantum Design in the vibrating sample magnetometer (VSM) setup and the Closed Cycle Measurement System (CCMS) built by Cryogenics Ltd. For the hysteresis curve, magnetization m as a function of the applied magnetic field H, the magnetic field scan was set between -1 T and 1 T, while for the ZFC and the FC curves the temperature scan was set between 8 K and 300 K with a set magnetic field of 0.01 T.

3.2. Dynamic characterization

This section comprises the experimental methods employed for the investigation of the dynamics of HEUR-MNPs nanocomposites. The description begins with the techniques which probe short time scales, like dielectric relaxation spectroscopy (DRS) ($\tau \sim 10$ ms) and neutron spin echo (NSE) ($\tau \sim 10$ ns). Then, the ones probing longer time scales ($\tau \sim 100$ s), like thermally stimulated depolarization current (TSDC) and differential scanning calorimetry (DSC), are described. Finally, a short introduction on rheology is reported.

3.2.1. Dielectric relaxation spectroscopy (DRS)

Dielectric relaxation spectroscopy is a powerful technique widely used in the investigation of the relaxation mechanisms occurring in amorphous materials, like polymers. Nowadays it covers the spectral range from 10^{-6} to 10^{12} Hz. The molecular dynamics in this frequency range is characterized by the superposition of different relaxation processes which take place on a local scale (β, γ and δ-relaxations) and as cooperative fluctuations (α-relaxation and dynamic glass transition) (Fig. 3.7).

Dielectric relaxation spectroscopy is based on the interaction of an external electric field with a the electric dipole moment of the sample, often expressed by the *permittivity* [92] [91] [93]. The application of the electric field to the sample is achieved by applying a voltage V across a capacitor consisting of two parallel plates electrodes whose separation distance, d, is small compared with their surface dimension. When a constant voltage V is applied, a static electric field E is created:

$$E = \frac{V}{d} \tag{3.12}$$

when there is vacuum between the two parallel plate electrodes the charges Q per unit area are stored on the plates and are proportional to the static field:

$$Q = \varepsilon_0 E \tag{3.13}$$

where ε_0 is the permittivity of the free space, 8.85 $\times 10^{-12}$ F/m. On the other hand, when the space between the parallel capacitor's plates is filled with a homogeneous dielectric material, the charges will be distributed in the material: negative charges are attracted to the positive electrode and vice versa. This effect leads to a storage of charges $+P$ and $-P$ per unit area on the dielectric material surfaces adjacent to the electrodes (Fig. 3.8). Therefore, the charges cannot move freely through the dielectric medium, but they are displace in amount of D, the so-called *dielectric displacement*:

$$D = \varepsilon_0 \varepsilon_s E = \varepsilon_0 E + P \tag{3.14}$$

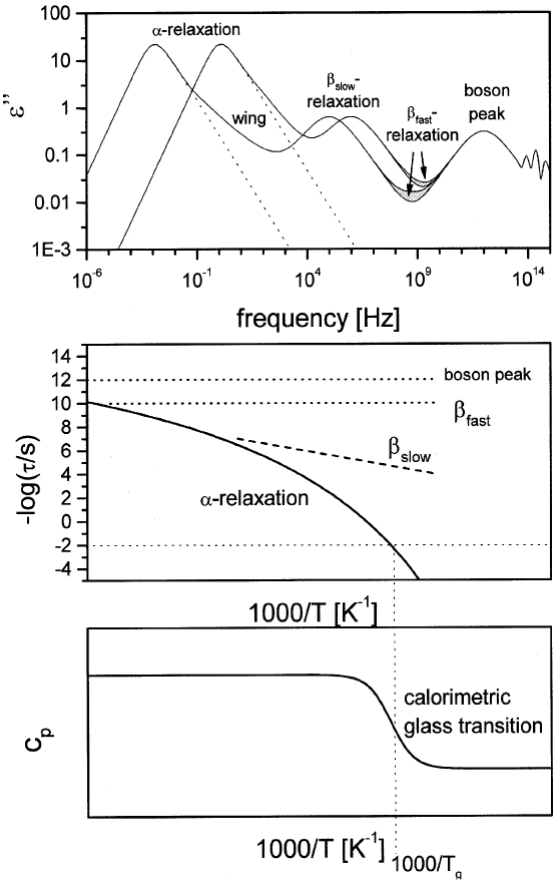

Figure 3.7.: Dynamic processes occurring in glass-forming liquids. Top: imaginary part of the complex dielectric function as a function of the frequency. The α and the β-relaxations (β_{fast} is often called γ), together with the boson peak, are shown. Middle: Relaxation map (relaxation time vs inverse temperature) of the loss processes shown on the top. Bottom: Calorimetric measurement of the glass transition temperature [91]

with ε_s being the static dielectric constant, or relative permittivity. The polarization P in the dielectric material can be derived from eq. 3.14:

$$P = \varepsilon_0 \chi E \tag{3.15}$$

where $\chi = \varepsilon_s - 1$ is the electric susceptibility.

In dielectric relaxation spectroscopy, a periodic electric field is applied on the dielectric material:

$$E = E_0 \cos \omega t = Re[E_0 \exp\{i\omega t\}] \tag{3.16}$$

where ω is the angular frequency. In this case, the *dielectric displacement* D will be shifted by a phase lag δ:

$$D = D_0 \cos(\omega t - \delta) = D_0 \cos\delta \cos(\omega t) + D_0 \sin\delta \sin(\omega t) \tag{3.17}$$

Considering that:

$$\tan\delta = \frac{\varepsilon"}{\varepsilon'} = \frac{\text{energy dissipated per period}}{\text{energy stored reversibly per period}} \tag{3.18}$$

The dielectric displacement is given by two contributions:

$$D_1 = D_0 \cos\delta = \varepsilon'\varepsilon_0 E_0, D_2 = D_0 \sin\delta = \varepsilon"\varepsilon_0 E_0 \tag{3.19}$$

Therefore, in a dynamic electric field, the complex dielectric constant can be written as a complex quantity:

$$\varepsilon^* = \varepsilon'(\omega) - i\varepsilon"(\omega) \tag{3.20}$$

where the imaginary part of the permittivity $\varepsilon"(\omega)$, is the dielectric loss. Therefore, the dielectric displacement D reads:

$$D = \varepsilon^*(\omega)\varepsilon_0 E \tag{3.21}$$

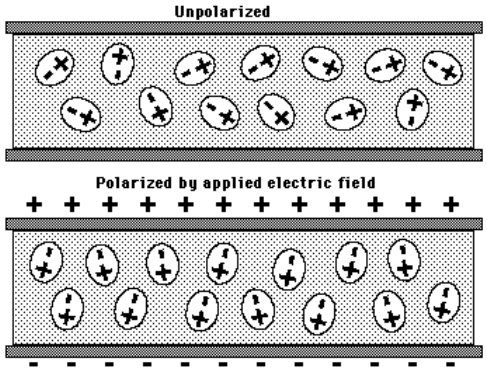

Figure 3.8.: Orientation of the electric dipole moments in a dielectric, upon the application of an external electric field **E**

Assuming a material with dipoles with a single relaxation time, it can be proven that [91]:

$$\varepsilon^*(\omega) = \varepsilon_\infty + \frac{\varepsilon_s - \varepsilon_\infty}{1 + i\omega\tau} \tag{3.22}$$

The eq. 3.22 is the *Debye equation*. The term $\Delta\varepsilon = \varepsilon_s - \varepsilon_\infty$ is called the *dielectric strength* and reflects the contribution of this kind of dipoles to the static dielectric constant. The *Debye equation* is the dielectric relaxation response of an ideal, non-interacting population of dipoles, with a single relaxation time τ, to an alternating external electric field. It describes the evolution of ε^* for a relaxation following the exponential decay shown in Fig. 3.9. The maximum of the symmetric function ε"(ω) corresponds to the inflection point of the function $\varepsilon'(\omega)$. The dispersion peak in the plot ε"(ω) as a function of the frequency allows a better resolution than the transition step in the plot $\varepsilon'(\omega)$ vs frequency. Therefore it is more often used in dielectric relaxation investigations.

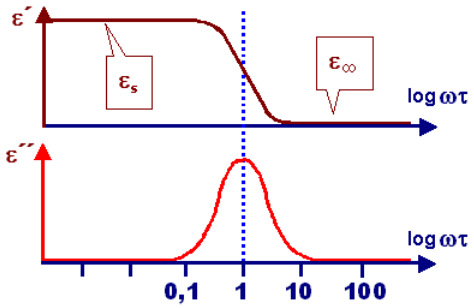

Figure 3.9.: Real and imaginary part of the dielectric complex permittivity ε^* as a function of $\omega\tau$ of the applied periodic field $\mathbf{E}$. ε_s and ε_∞ are the limits of the dielectric constant at small and high frequencies, respectively

Therefore, with DRS, the momentary delay in the dielectric constant of a material as a function of the applied electric field, is measured. This delay is caused by the delay in molecular polarization with respect to a changing electric field in a dielectric medium, and therefore, it is related to the molecular motion. It is important to consider that for polymer relaxations, the profile of ε"(ω) vs frequency is not symmetric and broader than the *Debye relaxation*, due to a distribution of relaxation times in the population of dipoles. In this case, ε^* can be described with the empirical *Havriliak-Negami* (HN) function:

$$\varepsilon^* = \varepsilon_\infty + \frac{\varepsilon_s - \varepsilon_\infty}{(1 + (i\omega\tau)^\alpha)^\beta} \tag{3.23}$$

The shape exponents α and β $(0 < \alpha, \beta < 1)$ are the shape parameters: α indicates the width of the peak and β its asymmetry. Values of $\alpha = \beta = 1$ correspond to a single relaxation time causing a Debye peak. In this case, the loss peak (represented in Fig. 3.9 in the case of a simple Debye relaxation) occurs at:

$$\omega_{max} = \left(\frac{\sin \frac{\pi\alpha}{2(\beta+1)}}{\sin \frac{\pi\alpha\beta}{2(\beta+1)}} \right)^{1/\alpha} \tau^{-1} \tag{3.24}$$

DRS Experimental set up

A dielectric, conductivity and impedance spectrometer for material analysis measures the electric properties of materials over a wide frequency and temperature range. A scheme of the spectrometer used in this work is shown in Fig. 3.10:

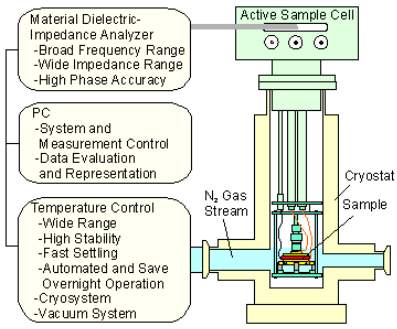

Figure 3.10.: Sketch of an impedance spectrometer showing all the components and their features

As shown in Fig. 3.10, the spectrometer consists of the following components:

- A system to measure the complex impedance $Z^*(\omega)$ of the sample capacitor over a sufficient frequency and impedance range. The measured broad frequency range is between 3×10^{-5} and 2×10^7 Hz, including low frequencies for characterization of dielectric relaxations and electrochemical effects.
- A sample cell that connects the sample capacitor to the impedance analyzer and mounts it into a cryostat for temperature control.
- A temperature control system which adjusts the sample capacitor to fixed temperatures.
- A computer with a software package for system control and evaluation.

DRS for the dynamic investigation of the HEUR-MNPs nanocomposites

Dielectric relaxation spectroscopy was employed for the investigation of the relaxation processes occurring in the HEUR-MNPs nanocomposites in the hydrogel and in the dried state. In both cases, a Novocontrol Impedance Spectrometer (Novocontrol Technologies GmbH & Co. KG Montabaur, Germany) was used in the frequency range between 0.01 Hz and 1 MHz. Concerning the measurements on the samples in the hydrogel state, they were performed in the temperature range between -100 °C to 25 °C in heating steps of 5°C or 10° C. Three HEUR hydrogels 25 wt % (aq) differing in the MNP concentration

(0 wt %, 0.46 wt % and 0.8 wt %) were measured. A few mg of each sample was placed between the gold plated electrodes (diameter 20 mm) of a liquid sample cell BDS1308 (Fig. 3.11). Silica spacers with diameter 0.5 mm were used for electric isolation and control of the sample thickness. For the DRS measurements on the nanocomposites in the dried state, the matrix and two nanocomposites with 1 and 3 wt % MNP concentration were investigated. In this case the measurements were performed in the temperature range between -85 °C and 25 °C, during cooling, in steps of 5 °C or of 10 °C. A film of each sample (1 mm) was placed between two gold plated electrodes (diameter 20 mm) of a parallel plate capacitor. For both types of samples, the capacitor was mounted in a cryostat and its temperature was controlled by a heated gas stream of nitrogen evaporated from the liquid state by a Novocontrol Quatro. The temperature was controlled with an uncertainty of 0.1 °C. The complex dielectric function $\varepsilon^*(\omega) = \varepsilon'(\omega) - i\varepsilon"(\omega)$ was then recorded by a Novocontrol Alpha Analyzer as a function of frequency ϵ.

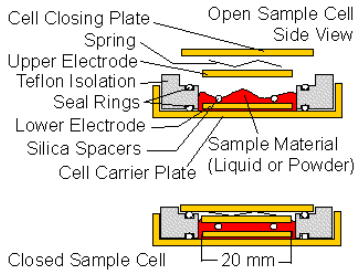

Figure 3.11.: Scheme of the liquid sample cell BDS1308 used for the DRS measurements on the nanocomposites in the hydrogel state

3.2.2. Neutron spin echo (NSE)

Inelastic neutron scattering (IENS) techniques are widely employed for the investigation of polymer dynamics. In conventional IENS techniques, the incident beam has to be monochromatized to a certain energy E_i. After the scattering process, the energy of the scattered beam E_f is analyzed and compared with E_i. In order to achieve high energy resolutions, a very narrow energy interval must be selected from the low-intensity neutron spectrum source. The neutron spin echo technique allows the study of polymer dynamics achieving higher resolution than the conventional IENS techniques [94]. This is possible because NSE measures the individual velocity changes of the incident and scattered neutrons using the Larmor precession of the neutron spin in a magnetic field. The velocities before and after scattering on one and the same neutron can be compared and a direct measurement of the velocity difference becomes possible. Relative resolutions in the order of 10^{-5} can be achieved with an incident neutron spectrum of 10-20 % bandwidth.

A schematic setup of the neutron spin echo spectrometer is shown in Fig. 3.12.

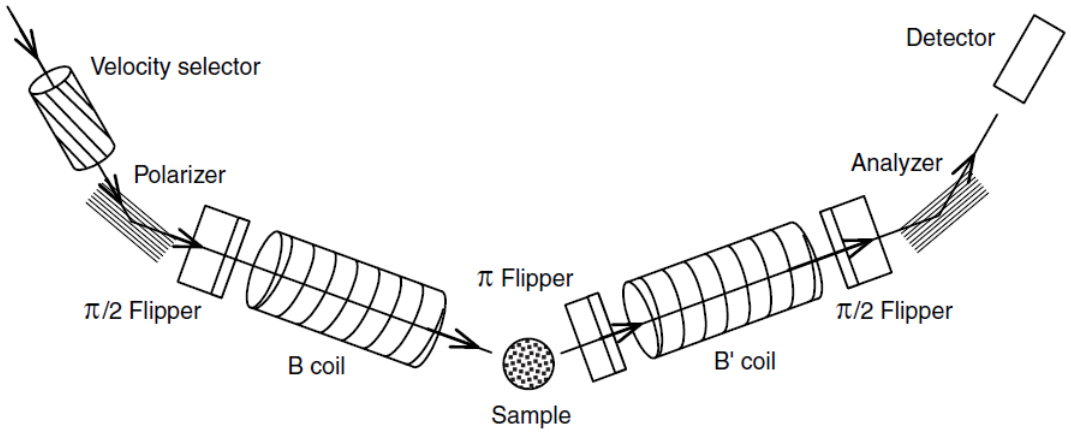

Figure 3.12.: Scheme of the NSE spectrometer. All the components, from the velocity selector to the detector, are shown

The components and their functions are the following:

- A velocity selector filters out a wavelength interval of 10-20 % width of the primary neutron beam. A polarizer orientates the neutron beam to a direction parallel to its direction of flight (z direction).
- The neutron beam encounters the so-called $\pi/2$ flipper. In this flipper, the polarization of the neutron beam is turned from its flight direction (z direction) into a perpendicular direction (x direction). In order to achieve this new polarization

direction, the neutrons pass through a magnetic filed with a direction at 45° to the z-axis whose the magnitude $\mathbf{B}_{\pi/2}$ and duration are chosen such that the neutron spin performs a Larmor precession of 90° around the titled axis (Fig 3.13 b)). The angular velocity of the Larmor precession is:

$$\omega_L = |\gamma|\mu B_{\pi/2}\hbar \tag{3.25}$$

with γ being the gyromagnetic ratio of the neutron, μ the nuclear magneton and $B_{\pi/2}$ the magnetic field. Being l the length on which the neutrons are affected by the field and $v = h/(m_n\lambda)$ their velocity, it is possible to calculate the precession angle ϕ:

$$\phi = \left(\frac{2\pi|\gamma|\mu\lambda m_n}{h^2}\right) B_{\pi/2} l \tag{3.26}$$

The polarization component along the x-axis is given by the beam average:

$$P_x = \langle \cos\phi \rangle = \int f(v) cos(\gamma_L l B_{\pi/2}) dv \tag{3.27}$$

where $f(v)$ is the neutrons velocities distribution, l is the length on the precession coil and γ_L=2.916 kHz/Gauss.

- At this point, the $\pi/2$ polarized neutrons pass through a cylindrical coil with magnetic field B parallel to the flight path in which the velocities encoding by Larmor precessions occurs. It accumulates a total phase ϕ.

- After being scattered by the sample, the neutrons pass through a so-called π-flipper which manipulate the spin of the neutrons inverting two spatial components of the neutron spin (e.g. y and z) leaving the third one unchanged, as shown in Fig. 3.13 a). This operation is equivalent to a 180° rotation in the $y - z$ plane.

- The π-polarized neutrons pass through a second precession coil called B', where the velocity decoding takes place, rotating "back" by a phase angle ϕ'.

- Finally a $\pi/2$ flipper restores the initial polarization of the neutron beam parallel to its flight direction.

- Analyzer for the final neutrons polarization.

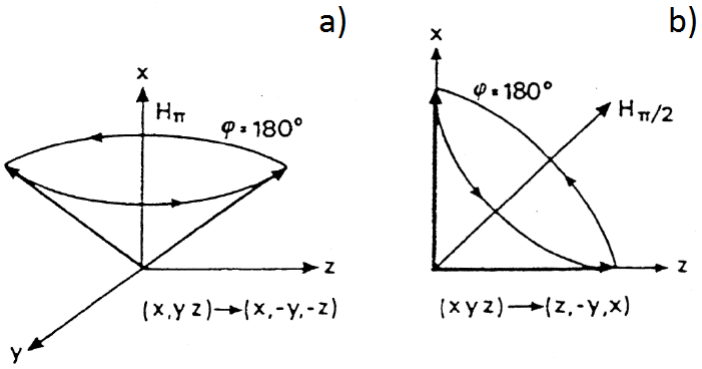

Figure 3.13.: Spin angular operations used in the neutron spin echo technique. a) Motion of the neutron polarization during the π and b) the $\pi/2$ rotation [94]

The initial polarization is restored only under certain conditions. In order to understand what is this condition, one has to consider that, in total, the neutron spin has rotated in both main precession coils, by $\phi - \phi'$ around the z-axis. Therefore, the final polarization is identical to the incident one if $\phi = \phi'(+2\pi n)$, especially if $\lambda_i = \lambda_f$ (elastic scattering) for $Bl = B'l'$. This condition is called *spin echo*. The *spin echo* condition can be visualized considering the *spin echo group* which shows the oscillations of the neutron beam polarization as a function of the flight path along the magnetic field (Fig. 3.14). After the neutron beam is polarized on the x-axis by the $\pi/2$ flipper with a polarization P_x,it passes through the π flipper where the polarization is inverted, and therefore, in the second coil, the precession will be opposite compare to the first one (part AC in Fig. 3.14). The point C in the diagram in Fig. 3.14 represents the spin echo condition, which occurs at the time, t_{NSE} defined as:

$$t_{NSE}(B) = \frac{\hbar \gamma_L l B}{m_n \bar{v}} \tag{3.28}$$

with $\bar{v}$ being the average velocity of neutrons.

Besides the spin echo conditions, which occurs in case of an elastic scattering event, the probability of a single neutron to reach the detector is reduced due to the polarization analyzer by $cos(\phi - \phi')$. Considering an inelastic scattering event, the precession mismatch which is the total Larmor precession angle from the first coil (Larmor angle of the precession inside the coil is ϕ) to the second coil (the Larmor precession inside the second coil is ϕ') can be approximated by:

$$\phi_{tot} = \phi - \phi' = \left(\frac{2\pi|\gamma|\mu m_n}{h^2}\right) Bl(\lambda_i - \lambda_f) \approx \frac{|\gamma|\mu m_n^2 \lambda^3 Bl}{h^3}\omega \tag{3.29}$$

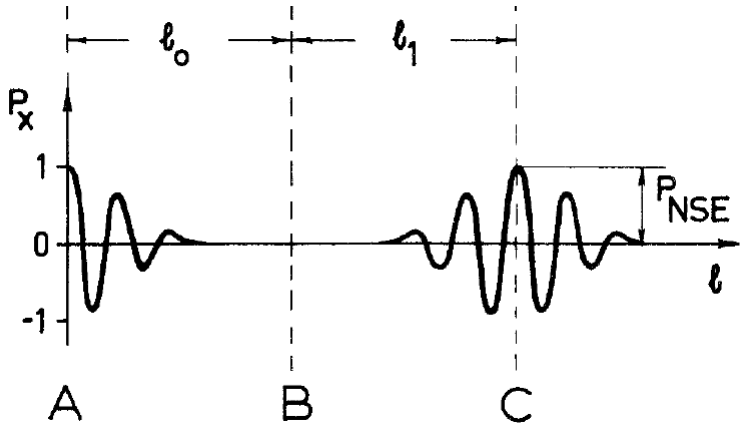

Figure 3.14.: Larmor spin precession of neutrons in a beam and the simple spin echo effect. P_{NSE} is the polarization the out coming neutrons, i.e. the NSE signal [94]

with the quantity $|\gamma|\mu m_n^2 \lambda^3 Bl/h^3$ being the time measured by NSE $t_{NSE}(B)$. The basic idea of the NSE spectroscopy is to use ϕ_{tot} to measure ω, which is the neutron energy transfer. The equation 3.28 is used to chose the magnetic field B to obtain the spin echo signal and to calculate the proportionality parameter t_{NSE} of the equation 3.29. Therefore the mismatch factor $cos(\phi - \phi')$ of which the neutron beam is reduced at the analyzer, can be written as $cos(t_{NSE}\omega)$. Because the energy transfer for inelastic scattering is not fixed, but distributed according to the scattering function $S(q,\omega)$ the reduction factor of $cos(\phi - \phi')$ to the count rate at the detector has to be weighted by the $S(q,\omega)$:

$$S(q, t_{NSE}) = \frac{\int_{-\infty}^{\infty} S(q,\omega) cos(\omega t_{NSE}) d\omega}{\int_{-\infty}^{\infty} S(q,\omega) d\omega} \tag{3.30}$$

Equation 3.30 is the intermediate scattering function defined in eq. 2.78. It is called *intermediate scattering function* because it is the Fourier transform in space of the microscopic van Hohe correlation function and, on the other side, the time-energy Fourier transform of the scattering function $S(q,\omega)$. The function $S(q,\omega)$ in eq. 3.30 is usually the coherent scattering function. In this work, the coherent contribution is by far the dominant part. The intermediate scattering function is given by the echo amplitude. The most common way to determine it is the following:

- The scattered beam polarization is measured by counting for a given time spin up (flipper π on) and spin down (flipper π off). These two points on the spin echo group are on the left in Fig. 3.15. The difference up-down is the maximum echo amplitude that is possible to recover.

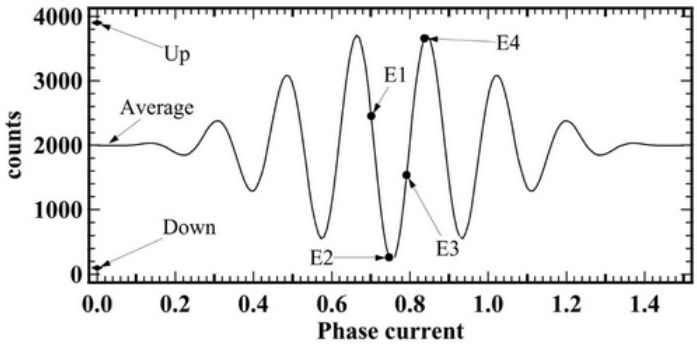

Figure 3.15.: Typical spin-echo group (counts as a function of the phase current) showing the 4 points echo measurement, E1, E2, E3 and E4 [95]

- The minimum reliable measurement sequence for recovering the amplitude is to record four points on the spin echo group placed by 90° steps around the center. These points are defined as:

$$E1 = Aver + E_{ampl}\sin(\phi) \tag{3.31}$$

$$E2 = Aver - E_{ampl}\cos(\phi) \tag{3.32}$$

$$E3 = Aver - E_{ampl}\sin(\phi) \tag{3.33}$$

$$E4 = Aver + E_{ampl}\cos(\phi) \tag{3.34}$$

  From the four equations 3.31 - 3.34 the average intensity ($Aver$), the echo amplitude (E_{ampl}) and the phase (ϕ) can be determined

- Finally, the echo amplitude E_{ampl} is divided by the initial polarization (up-down/2), thus giving $S(q,t)$ in a normalized form:

$$\mathrm{S}(q,t)/S(q,0) = \frac{X_{sample}}{X_{reference}} \tag{3.35}$$

  with

$$X_{sample} = \frac{2E_{ampl,sample}}{Up_{sample} - Down_{sample}}, \tag{3.36}$$

$$X_{reference} = \frac{2E_{ampl,reference}}{Up_{reference} - Down_{reference}} \tag{3.37}$$

  where Up and $Down$ are, respectively, the up and down initial polarizations. The reference is a sample which scatters elastically in the probed q-range; usually activated carbon powder is used for this purpose because of its large surface area per unit volume.

NSE for the dynamic characterization of the HEUR-MNPs nanocomposites

In this work, the dynamics of the HEUR-MNPs nanocomposites in the hydrogel state, was investigated using Neutron Spin Echo Spectroscopy (NSE). NSE measurements were performed on the pure HEUR hydrogels 25 wt % (aq) as reference and on the hydrogels containing MNPs at two different concentrations: 0.46 wt % and 0.8 wt %. In order to achieve maximum contrast and minimum incoherent background arising from protonated material, we used heavy water (D_2O) as a solvent for the hydrogel samples. The measurements were performed at the $J-NSE$ spectrometer at the FRMII research reactor in Garching, Germany [96], in the q-range between 0.05 $\AA^{-1}$ and 0.21 $\AA^{-1}$ at a wavelength of 8 $\AA$, probing Fourier times up to 40 ns. The samples were mounted in a thermostat controlled sample environment at 25 °C.

3.2.3. Differential scanning calorimetry (DSC)

Differential scanning calorimetry is a technique in which the difference in the amount of heat required to increase the temperature of a sample and a reference is measured as a function of the temperature. It is useful to study the thermal behaviour of materials. A scheme of the experimental setup is shown in Fig. 3.16.

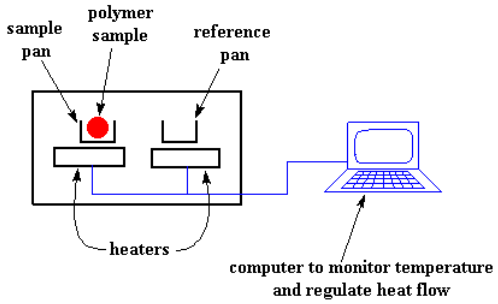

Figure 3.16.: Differential scanning calorimetry device with the heaters connected to the sample and the reference pans

As shown in Fig. 3.16, two heaters are connected to two pans. One of them is empty and it serves as reference, and the other one contains the sample. The heaters heat the two pans at a specific rate which stays exactly the same throughout the experiment. The two separate pans, with their two separate heaters, heat at the same rate as each other. The heater underneath the sample pan has to put out more heat than the heater underneath the reference pan. The result of the experiment is the so-called *thermogram* which reports the difference in heat output of the two heaters at a given temperature (also called *heat flow*) as a function of the temperature. The *heat flow* is defined as the heat q supplied by the unit time t:

$$\text{heat flow} = \frac{q}{t} \tag{3.38}$$

By dividing the *heat flow* by the temperature rate, $\Delta T/t$, we obtain the *heat capacity*, C_p, which gives information about the phase transitions observed in the sample:

$$C_p = \frac{q}{\Delta T} \tag{3.39}$$

In Fig.3.17 a typical DSC thermogram is shown.

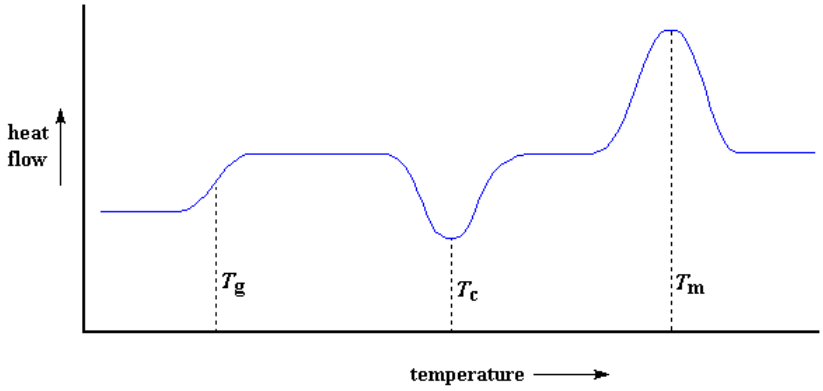

Figure 3.17.: Generic heating thermogram (heat flow as a function of the temperature) showing three different phase transitions: the glass transition, the crystallization and the melting

During the heating of a sample, from room temperature to its decomposition temperature, peaks with positive and negative *heat flow* may be recorded. The thermogram shown in Fig. 3.17 is acquired during heating and, therefore, the endothermic transitions occurs as peaks, while the exothermic ones as dips. The exothermic peak occurring at the temperature T_c is due to the *crystallization* of the sample and the T_c is the crystallization temperature. Increasing the temperature, we observe an endothermic peak occurring at the temperature T_m which corresponds to the phase transition of *melting*. Both these phase transitions occur in crystalline or semi-crystalline materials. In the thermogram shown in Fig. 3.17, at temperatures below the crystallization temperature T_c, it is possible to observe a phase transition which appears like a step, with the inflection point occurring at T_g. This transition is the so-called *glass transition* occurring in amorphous or semi-crystalline materials, and it is a very important phase transition in polymers. The main difference between the *glass transition* and the other two phase transitions shown in the thermogram in Fig. 3.17, i.e. *crystallization* and *melting*, is the fact that in the case of the *glass transition* we observe a change in the heat capacity of the system but it is not accompanied by a change in enthalpy. On the other hand, both *melting* and *crystallization* involve giving off or absorbing heat, therefore, they present the so-called *latent heat*.

Phase transitions as the *glass transition* which do not involve change in the latent heat are called *second order transition*, while phase transitions as *melting* and *crystallization* which involve a change in the heat capacity and in the enthalpy of transition are defined as *first order transitions*. Obviously, not in all the samples we observe all the types of phase transitions shown in the thermogram in Fig. 3.17 but possibly only in samples with both amorphous and crystalline domains.

DSC measurements on the HEUR-MNPs nanocomposites

Differential scanning calorimetry measurements were carried out on the systems investigated in this work in order to study their thermal behaviour. Concerning the hydrogel samples, we investigated the pure HEUR hydrogel matrix (25 wt % (aq)) and the nanocomposite hydrogels with two MNP concentrations: 0.46 wt % and 0.8 wt %. The measurements were performed in nitrogen atmosphere. For the investigation of the phase transitions of the HEUR-MNPs nanocomposites in the dried state, we investigated the pure polymer matrix and the nanocomposites with 1 wt % and 3 wt % MNP concentration. For the hydrogel samples, the measurements were performed from -160 to 100 ° C with cooling and heating rates fixed at 20 °C/min. In the case of the nanocomposite in the dried state, three cooling scans were performed with starting temperatures of 150 °C, 80 °C and 40 °C down to -150 °C, and two heating scans from -150 °C up to 80 °C and up to 90 °C with 10 °C/min. A TA Instruments Q200 differential scanning calorimeter was used. For both the morphologies of the investigated samples, a few mg of sample were placed in aluminium T_0 pans (by TA Instruments).

3.2.4. Thermally stimulated depolarization current (TSDC)

Thermally stimulated depolarization current is a technique useful for the investigation of the structure, of the electrical properties and of the dynamics of the materials. It is ideal for the investigation of polymer dynamics, because it is a more sensitive alternative than other thermal analysis techniques for detecting the phase transitions which depend on changes in molecular mobility [97, 98]. It is possible to obtain similar information as in the case of the Dielectric relaxation spectroscopy (DRS) (paragraph 3.2.1) but in a lower frequency range ($\approx 10^{-3} Hz$) and in the temperature domain. In Fig. 3.18, a scheme of the TSDC experimental setup is shown.

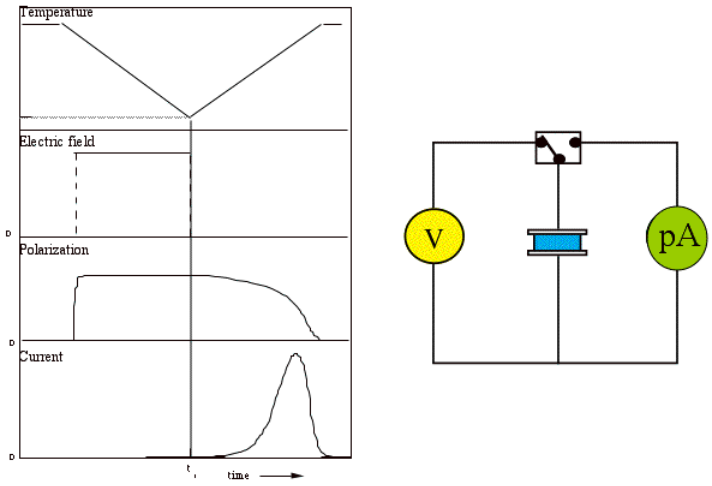

Figure 3.18.: Left: behaviour of the input variables (temperature and electric field) and of the measured response (polarization and current) as a function of the time. Right: simple sketch of the experimental setup for TSDC measurements

As it is possible to observe in the Fig. 3.18, the sample is placed between short-circuited electrodes. It is placed in an oven and heated up to a temperature T_p higher than its glass transition temperature T_g, in order to eliminate surface and volume charges. Then a DC electric field E_p is applied at a temperature T_p for a time t_p longer than the expected relaxation time for the reorientation of dipoles. In presence of the electric field, the sample is rapidly cooled to a temperature $T_0 \leq T_p$, where all the dipole/ionic motions are completely hindered. Then, the sample is short circuited for a few minutes to remove stray charges, and then it is connected to an electrometer which measures the depolarization current as a function of the temperature, while the sample is heated at a linear rate for 1 to 3 K/min. The resulting TSDC spectrum shows maxima corresponding to the various decay precesses. The mechanisms which give rise to these decay processes are:

- in polar materials, the decay process may be caused by the orientation of permanent dipoles

- trapping of charges by structural defects or impurities and build up of charges near heterogeneities such as the amorphous-crystalline interfaces in semi-crystalline polymers and the grain boundaries in polycrystalline materials.

Therefore, the type of processes detected in TSDC measurements during discharge depends on the nature of the polymer. The net charge of the polymer is generally due to the aligned dipoles and space charges. In polar polymers the disorientation of charges plays a prominent role. The discharge by dipole disorientation is thermally activated and thus, can be speeded up by heating. As a result of the disorientation of polar side groups at low temperatures, the peak related to the β relaxation is observed. When the polymer is heated to its glass transition temperature, its dipoles are disoriented by the mobility of the main chain large segments. This disorientation is responsible for the α peak, located at the glass transition temperature T_g of the polymer.

TSDC measurements on the HEUR-MNPs nanocomposites

TSDC measurements were performed on the HEUR-MNPs nanocomposites in the dried state, in order to have information about the dynamic processes occurring at low frequencies ($10^{-4} - 10^{-2}$ Hz as equivalent frequency). In fact, these processes were not observable in the Dielectric spectroscopy measurements, because of the high conductivity contribution. The investigated samples were the pure HEUR polymer film, and two nanocomposites as dry films with 1 wt% and 3 wt% MNP concentration respectively. Each sample was inserted between the plates of a parallel capacitor and was polarized by an electric field E_p at a polarizing temperature T_p for a time t_p. With the electric field still applied, the sample was cooled to a temperature T_0, which is chosen to be low enough to prevent depolarization by thermal energy. Then, the sample was short-circuited and reheated at a constant rate b. The discharge current generated during heating was measured as a function of the temperature with a sensitive electrometer. TSDC measurements were carried out in the temperature range from -150 to 20 °C using a Keithley 617 electrometer in combination with a Novocontrol sample cell for TSDC measurements. Typical experimental conditions were T_p = 20°C and -60°C, E_p = 5 kV/cm, t_p = 5 min, a cooling rate of 10 K/min, T_o = -150°C, and b = 3 K/min.

3.2.5. Introduction to rheology

In this section, a brief introduction about rheology is reported. Further details about rheology and the behaviour of complex fluids can be found in the books of Larson [99] and Barnes [100]. Rheology is defined as the study of the deformation and flow of the matter. The response of the matter to an applied force is defined as *deformation*, and it differs for different kinds of materials. The effect of the deformation of the material on its properties, like for instance the viscosity η, are measured by rheometry. The viscosity of a fluid is defined as a measure of its *resistance to flow*, and it reflects internal relaxation processes. The viscosity of a fluid can be significantly affected by variables such as *shear rate*, temperature, pressure and *time of shearing*. The force that is required to produce the motion of a fluid is called *shear stress* and it is defined as:

$$\sigma = \frac{F}{A} \tag{3.40}$$

where F is the force applied to the material, and A is the surface parallel to the direction of the force F. A sketch of the deformation that the shear stress produces in a solid is depicted in Fig. 3.19.

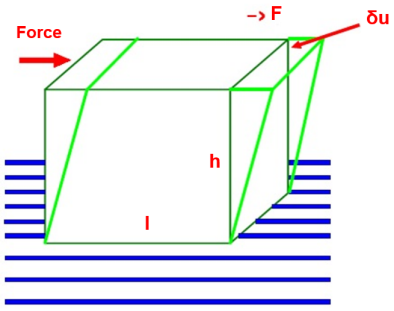

Figure 3.19.: Sketch of an ideal solid on which a shear stress $\sigma = F/A$ is applied. A is the area of the upper surface of the cube and δu is the deformation produced by the shear stress

For an ideal solid, like the one of Fig. 3.19, which is also defined as a *purely elastic* material, the Hooke's law states that the stress is proportional to the *strain*:

$$\sigma = G\gamma \tag{3.41}$$

where the *strain* γ is the ratio between the deformation δu and the height h, and G is the so-called *shear modulus*, which is constant. Therefore, in the case of *purely elastic* materials, the response to the stress is linear. In this case, the material has undergone a fully recoverable deformation, therefore, no flow has occurred. On the other hand, if we consider a cube of material which behaves as an *ideal fluid* and we apply the shear stress

σ, the material will deform with a deformation which continually increases at a constant rate (Fig. 3.20). The rate of change of the strain is called *shear strain rate* or *shear rate* ($\dot{\gamma}$) and it is defined as:

$$\dot{\gamma} = \frac{\delta u}{\delta t} \tag{3.42}$$

The relation between the viscosity of the fluid and shear rate is:

$$\eta = \frac{\sigma}{\dot{\gamma}} \tag{3.43}$$

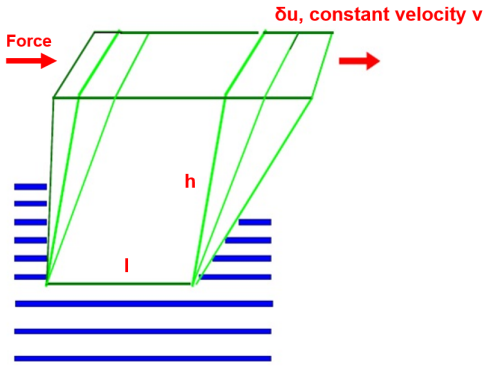

Figure 3.20.: Sketch of an ideal fluid on which a shear stress $\sigma = F/A$ is applied. A is the area of the upper surface of the cube and δu is the deformation produced by the shear stress

If a fluid has a viscosity η which is independent on the shear stress σ, then it is defined as an *ideal fluid* or a *Newtonian fluid*. However, there are complex fluids with behaviour which differ from the *Newtonian fluids*. These class of fluids are then defined as *non-newtonian fluids*. For such fluids, the relation between the viscosity η and the shear stress σ (and the shear rate $\dot{\gamma}$) is non-linear. There are different types of *non-newtonian* behaviour, but here we focus on the discussion of only two of them, which are:

- *shear thickening fluids*, also called *dilatants*. They are characterized by a viscosity that increases with the shear rate (green line in Fig. 3.21 [101]). Usually, suspensions rather than pure liquids exhibit this kind of behaviour.

- *shear thinning fluids*, also called *pseudoplastic fluids*. They are complex fluids characterized by an apparent viscosity that decreases when subjected to shear strain (blue line in Fig. 3.21 [101]).

As seen in Fig. 2.5 aqueous solutions of HEUR polymers, investigated in this work, exhibit a viscosity-shear stress profile which is a combination of *newtonian*, *shear thickening* and *shear thinning*. Indeed, the viscosity dependence on the shear rate $\dot{\gamma}$, depends on the size and of the structure of the particles in the solution.

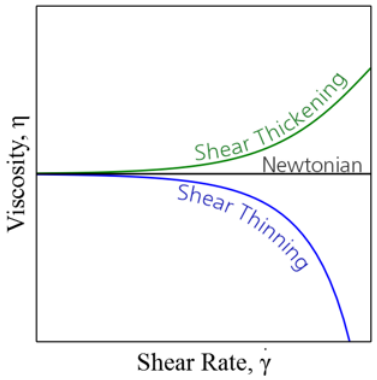

Figure 3.21.: Viscosity-shear rate curves for newtonian (black line), shear thickening (green line) and shear tinning fluids (blue line) [101]

Rheometry experimental set up

The response of the viscosity of a fluid upon the shear stress, and many other rheological properties of fluid materials, can be measured with rheometry. The measuring system, called rheometer, can be used in different geometries, depending on the nature of the material under investigation, i.e. liquid, gel, etc. The geometry used in this work for the investigation of gels is the so-called *cone and plate* geometry, which is schematically represented in Fig. 3.22.

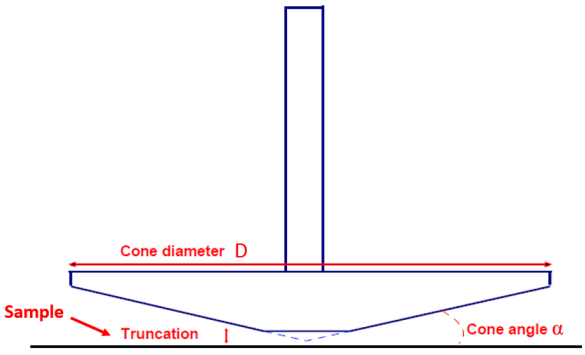

Figure 3.22.: Measuring system with cone and plate geometry. The cone has a diameter, D, and a cone angle, α. Its edge is truncated up to a height of 50 μm. The sample is placed on the plate, while the cone turns

There is a gap between the cone and the plate and strain and shear rate are calculated using the angular displacement at the gap. For high viscosity samples, a cone and plane or parallel plate is generally used; the latter is insensitive to gap setting but care must be taken due to a slight shear rate gradient across the sample. A cone geometry eliminates

this problem and is generally the choice for highly viscous pastes, gels and concentrated suspensions.

Rheology measurements on the HEUR hydrogels

The HEUR aqueous solutions were investigated by rheology in order to obtain the flow curves, i.e. the viscosity η versus the shear rate $\dot{\gamma}$. We measured the viscosity of the samples by varying the shear rate $\dot{\gamma}$ in the range between 0.1 and 1000 1/s. We analysed seven HEUR aqueous solutions with different polymer concentrations: 1 wt%, 2 wt%, 3 wt%, 4 wt%, 5 wt%, 10 wt% and 25 wt%. The flow curves of the HEUR solutions were measured using a *MCR-501 Anton Paar* stress-controlled rheometer (used in strain-controlled mode) using cone and plate geometry, which is suitable for gel-like samples.

4. Sample preparation

In this chapter, the chemicals and the preparation of the samples investigated in this work are presented. In particular, the synthesis of the MNPs is described in details, and their characterization, carried out with dynamic light scattering (DLS) and transmission electron microscopy (TEM), are also shown.

4.1. Materials

The telechelic polymer used in this work is the commercial TAFIGEL® PUR 61 (25 wt% water emulsion, M_w = 11857 g/mol ±1.3%, $D = 1.09 \pm 2.7\%$) and was purchased from Münzing Chemie GmbH (Heilbronn, Germany). Its chemical structure is depicted in Fig. 4.1. For the synthesis of the hydrophobically coated magnetite nanoparticles, Fe(III) acetylacetonate ($Fe(acac)_3$, 99.9%), 1,2 hexadecanediol ($C_{14}H_{29}CH(OH)CH_2(OH)$, 90%), oleylamine ($C_9H_{18}$=$C_9H_{17}NH_2$, 70%), oleic acid ($C_9H_{18}$=$C_8H_{15}COOH$, 99%) phenylether ($C_{12}H_{10}O$, 99%), and solvents (hexane, ethanol) were purchased from Sigma Aldrich.

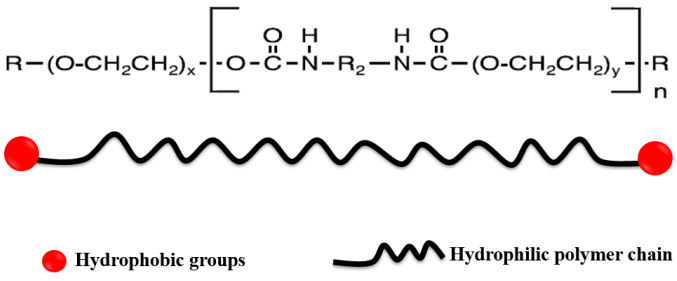

Figure 4.1.: Chemical structure of the HEUR polymer, with x=1, y=16, n=14, R_2=C4 and R=C14 [102]

4.2. Magnetite nanoparticles (MNPs) preparation

4.2.1. Synthesis of hydrophobic magnetite nanoparticles

The hydrophobically coated magnetite nanoparticles were synthesized through thermal decomposition of iron Fe(III) salt, $Fe(acac)_3$ [48]. A sketch of the hydrophobic MNPs is shown in Fig. 4.2 a). Briefly, 0.71 g $Fe(acac)_3$ (2 mmol) was mixed in 20 mL of phenylether with 2 mL of oleic acid (6 mmol) and 2 mL of oleylamine (4 mmol) under nitrogen atmosphere with vigorous magnetic stirring and 2.58 g (10 mmol) 1-2- hexadecanediol was added into the solution. The solution was heated to 200 °C and refluxed for 2 h. After refluxing, the solution was cooled to room temperature and ethanol was added to it. The product was separated by centrifuging using a Sigma 3K30 centrifuge at 10000 rpm for 20 minutes and re-dispersed in hexane in order to obtain a stock solution of magnetite nanoparticles (3.6 g/L). The product was characterized by Dynamic light scattering (DLS) in order to obtain the size distribution of the MNPs (Fig. 4.3). Transmission electron microscopy (TEM) was employed to obtain the shape and the size distribution of the MNPs (Fig. 4.4 a)).

4.2.2. Preparation of hydrophilic magnetite nanoparticles

The principle of the functionalization of MNPs is covering the hydrophobic monolayer, composed of oleic acid and oleylamine, of the MNP with a charged surfactant resulting in a bilayer structure surrounding the MNP [103]. A sketch of the hydrophilic MNPs is shown in Fig. 4.2 b). Trimethyloctadecylammonium bromide ($CH_3(CH_2)_{16}CH_2N(CH_3)_3{}^+Br^-$) ($C_{18}$TAB) was chosen as charged surfactant for the functionalization. A solution of C_{18}TAB in 2 mL of D_2O (0.0164 M) was added to 0.8 mL of hydrophobic MNPs in hexane solution (3.6 g/L). A phase separation between the two solutions occurred, and sonication was applied at 50 °C in order to evaporate the hexane slowly and to stir the MNPs and the surfactant molecules in the sample. In this way, the C_{18}TAB, interacting with the external shell of the MNPs, forms a hydrophilic external layer that promotes their transfer in the water phase during the hexane evaporation.

The final product was characterized by DLS. The intensity-weighted and the number-weighted size distribution plots are shown in Fig. 4.3. The number-weighted size distribution peaks occur at $R_H = (6.1 \pm 0.3)$ nm for the hydrophobic nanoparticles and at $R_H = (8 \pm 2)$ nm for the hydrophilic type. In the intensity weighted size distribution the presence of MNPs clusters is visible for both types of MNPs. For the hydrophilic MNPs the percentage of clusters ($R_H = (151 \pm 5)$ nm) is higher than for the hydrophobic type. In addition, the clusters composed of hydrophilic MNPs have higher hydrodynamic radius

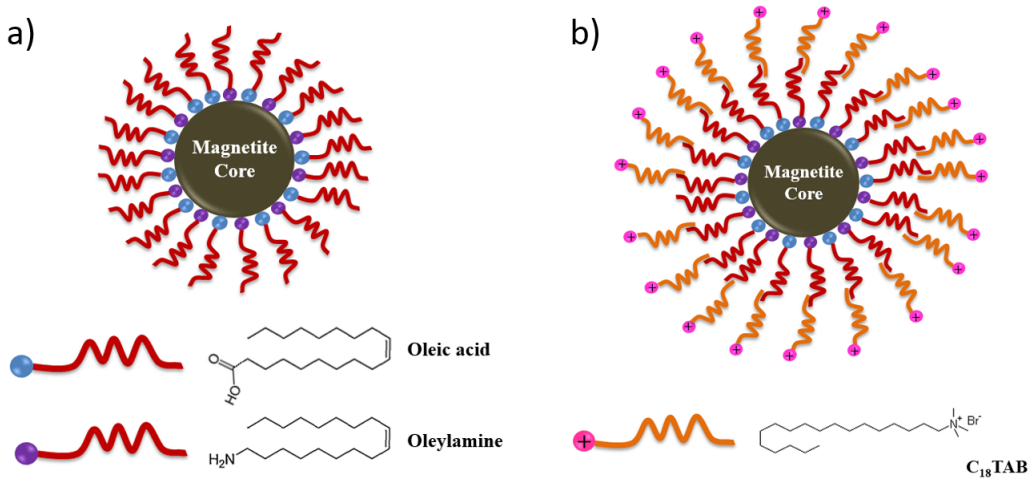

Figure 4.2.: Sketch of the a) hydrophobically coated magnetite nanoparticles b) magnetite nanoparticles coated with an additional charged shell, which makes them hydrophilic [102]

than the clusters formed by the hydrophobic ones. This is due to the functionalization procedure, because during the passage between the hexane and the water-phase the hydrophobic MNPs tend to aggregate between each other before the C_{18}TAB covers their surface.

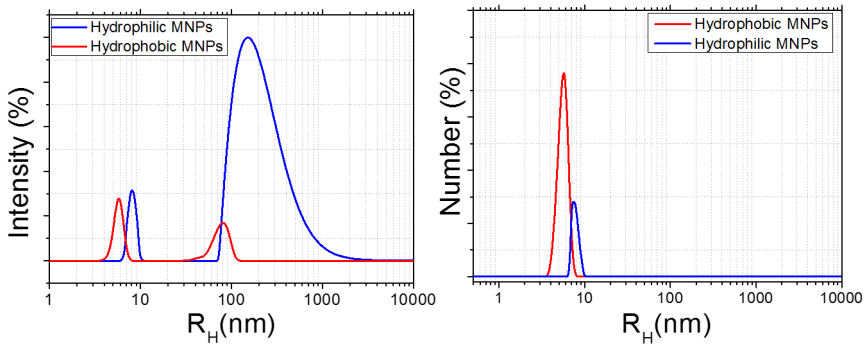

Figure 4.3.: Size distributions of hydrophobic coated MNPs (red line) and of hydrophilic coated MNPs (blue line). The error bars are smaller than the line width

In order to obtain the shape and the size distribution of the functionalized MNPs, transmission electron microscopy (TEM) was employed (Fig. 4.4 b)).

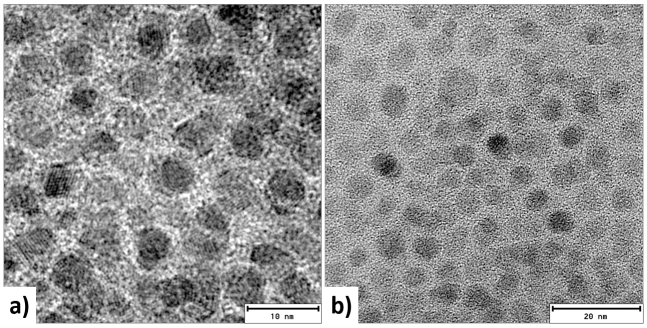

Figure 4.4.: a) TEM images of a 2.3 g/L hydrophobic MNPs solution in hexane b) TEM images of the 2.3 g/L hydrophilic MNPs solution [102]

4.3. Preparation of the HEUR-MNPs nanocomposites

4.3.1. Preparation of the HEUR-MNPs nanocomposites as hydrogels

The nanocomposites in the hydrogel state were obtained by mixing 1 mL of telechelic polymer emulsion in D_2O (25 wt %) and 0.21 mL of a 3.6 g/L hydrophobic MNPs solution in order to achieve a hydrophobic MNPs concentration of 0.23 wt% in the final gel. We prepared the hydrogel with 0.46 wt%, 0.8 wt%, 1 wt% and 3 wt% hydrophobic MNP concentration, using the same procedure. The nanocomposites as hydrogels containing hydrophilic MNPs were prepared by adding to 1 mL of telechelic polymer emulsion in D_2O (25 wt%) 0.28 mL of hydrophilic MNPs solution 2.7 g/L in D_2O for one sample, and 0.56 mL for the sample with double amount of hydrophilic MNPs. The concentration of hydrophilic MNPs in these hydrogels was 0.23 wt% and 0.46 wt% respectively. For the preparation of the nanocomposites with 1 wt% and 3 wt% hydrophilic MNP concentration, we added to 1 mL of telechelic polymer emulsion in D_2O (25 wt%), 0.97 mL and 3.0 mL of 3.4 g/L hydrophilic MNPs solution respectively. This resulted in a gel-like homogeneous solution.

4.3.2. Preparation of the HEUR-MNPs nanocomposites as dry films

The nanocomposites in the dried state were obtained through casting solution, which means evaporation of the solvent (mixture of D_2O and hexane) from the polymer-MNPs solution deposited on a solid support. A metallic frame with a specific depth of 0.1 mm was used as support for the casting procedure. A mixture of 0.74 g of the telechelic polymer emulsion in water (25 wt%) and 0.24 mL of a standard solution of hydrophobic MNPs solution in hexane 1.76 g/L, was carefully spread on the metallic frame used as support. Then the solvent was evaporated at room temperature for 48 h. Despite the different polarity of the solvents the mixing was easy, thanks to the surface active properties of

the TAFIGEL® PUR 61 polymer. The resulting nanocomposite as thin dry film, had a hydrophobic MNP concentration of 0.23 wt%. In addition, we prepared nanocomposite dry films with hydrophobic MNP concentration of 0.46 wt%, 1 wt% and 3 wt% following the same casting procedure.

5. Structural characterization

This chapter comprises the results of the structure characterization obtained for the HEUR-MNPs nanocomposites. Part of this chapter has been published in the article: "Nanocomposites composed of HEUR polymer and magnetite iron oxide nanoparticles: Structure and magnetic response of the hydrogel and dried state", *Polymer*, vol. 60, pp. 176-185, 2015 [102]. The structural characterization of the inner structure was carried out employing small angle neutron scattering (SANS). Transmission electron microscopy (TEM) was employed to provide information about the morphology of the nanocomposites. The results are shown starting from the investigation of the pure HEUR polymer matrix. The SANS results on the HEUR aqueous solutions are compared with the rheology measurements, in order to have a complete overview about the structural changes occurring in solution when the polymer concentration is increased. Then, the results of the structural investigation of the nanocomposites are shown and discussed starting from the nanocomposites in the hydrogel state. In this section, a comparison between the results on the hydrogels containing two different types of MNPs (hydrophilic and hydrophobic) is made. Furthermore, the structural investigation of the nanocomposites in the dried state is also presented. Finally, we present a comparison between the results achieved for the nanocomposites in the two different morphologies, i.e. as dry films and as hydrogels. Besides the results obtained with the fit model based on the Teubner-Strey theory [60] [68] [102], we discuss the results achieved with an alternative fit model, the "polydisperse core-shell spheres" model. Finally, the results obtained with both models are compared. The last paragraph focuses on the discussion of the magnetic response of the HEUR-MNPs nanocomposites in the dry state.

5.1. Structural investigation of the pure HEUR polymer matrix

In order to have a complete overview of the structural organization of the novel nanocomposite systems, we characterized the structure of the polymer matrix without the presence of either hydrophobic or hydrophilic MNPs. The polymer which we chose is a telechelic polymer, characterized by the presence of hydrophobic end-groups (C14 alkyl chain) which are able to aggregate in polar solvents. The behaviour of similar kinds of HEUR polymers in water was extensively studied with rheological measurements [10, 13] while the critical aggregation concentration was obtained through fluorescence and DLS measurements [104]. According to the experimental evidences collected and on the basis of the behaviour of similar associating telechelic polymers [10, 24], as explained in the paragraph 2.1.1 (chapter 2) the telechelic polymers behaves in aqueous solution as schematically drawn in Fig. 2.2. The CMC of the HEUR telechelic polymer under investigation was measured through fluorescence measurements using the anionic dye 8-anilino-1-naphtalenesulfonic acid magnesium salt (ANS) (Fig. A.1 in the appendix A, section A.1) [105, 106]. The experimental CMC value is found to be (2.89 ± 0.13) x 10^{-4} g/mL. As seen in Fig. 2.2 when the polymer concentration is $\phi_{poly} = \phi^*$ (with $\phi_{poly} >$ CMC), a reversible network is formed. This structure is characterized by attachment/detachment of the hydrophobic end-groups from the micellar domains. Therefore, we define it as "dynamical gel". We will also refer to it as "open gel" because the micellar cores are far apart between each other, and this results in a homogeneous structure similar to the liquid-like state. On the other hand, at high polymer concentrations ($\phi_{poly} > \phi^*$) a dense network structure is generated [107, 108]. In this case, the hydrophobic domains become closer between each other and entangling between the hydrophilic chains occur: Therefore, we refer to this phase as "hard gel". The scattering data obtained from the SANS measurements on the HEUR polymer solutions in D_2O at increasing polymer concentration are shown in Fig. 5.1.

All the SANS data exhibit high intensities at low values of the scattering vectors q, and a broad shoulder in the intermediate q range is observed. This latter broad shoulder increases as the telechelic polymer concentration ($\phi_{polymer}$) is raised and moves at to higher q values. A correlation peak is observed for the hydrogels with 10 wt%, 15 wt% and 25 wt% polymer concentration. Thus, the experimental evidences suggest the presence of a hierarchy of the structural organization of the polymer over several hundreds to a few nanometers. This polymer organization builds up as the polymer concentration is increased. For a quantitative understanding, the experimental SANS data are fitted with the model base on the TS theory, written in eq. 2.61 [60]. In fact, the obtained patterns

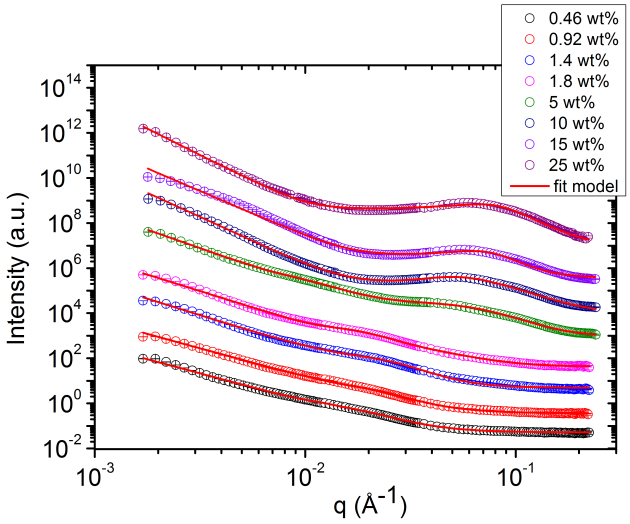

Figure 5.1.: Measured SANS data (points) of the aqueous HEUR solutions with different polymer concentrations as function of the scattering vector q. The error bars are smaller than the symbol size. The black curve is shown on absolute scale [cm^{-1}] while all other curves are shifted along the y-axis for clarity of the presentation. The solid lines refer to the equation 5.1 used to fit the data [102]

show the same features of the SANS profiles of bicontinuous microemulsions shown in Fig. 2.23. Furthermore, we justify the choice of this fit model, considering that it was used for the structural investigation of sulfonated polyether ether ketone (PEEK)/silesquioxane composite membranes. These membranes contain ionic domains in the polymer matrix, therefore they present a similar network-like structure as the HEUR one [109]. The exact fit function used to fit data reads:

$$f(q) = \mathrm{A}_1 q^{-p} + \frac{\mathrm{A}_2}{(q_{max}^2 + \xi^{-2})^2 - 2(q_{max}^2 - \xi^{-2})q^2 + q^4} + \frac{\mathrm{A}_3\ \mathrm{erf}^{12}(0.432 q R_g)}{(qR_g)^4} + bkg \quad (5.1)$$

where A_1, A_2, A_3 are amplitudes of the three different contributions, p is the exponent of the power-law at low q values, q_{max} is the position of the correlation peak, ξ is the correlation length, R_g is the radius of gyration of the scattering objects with $R_g \leq 2\pi/q_{max}$ and bkg is the constant background. By fitting the SANS data with the equation 5.1, we extract the following key-parameters:

- The exponent p of the low-q power-law ($q < 0.01$ Å^{-1}) which contains information about the fractal structure of the density fluctuations.

- The peak position q_{max}, which provides information about the distance between the hydrophobic domains ($d = 2\pi/q_{max}$) formed by the alkyl end groups of the HEUR polymers. Indeed, the presence of a correlation peak is commonly found in scattering spectra from networks with high functionality, resulting in the junction points serving as scattering centers [110–112].

The concentration dependence of the key-parameters, provides information about the phase behaviour of the HEUR polymers in aqueous solution. The plot of the exponent p as a function of the polymer concentration $\phi_{polymer}$ is shown in Fig. 5.2.

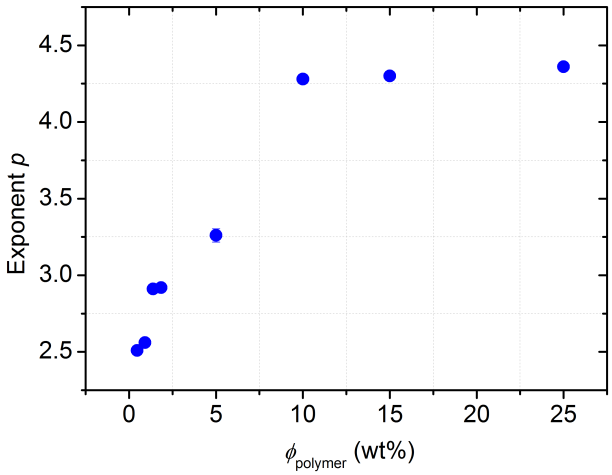

Figure 5.2.: Exponent p describing the fractal dimension of the polymer network as function of the polymer concentration. The error bars are smaller than the symbol size [102]

As explained in the chapter 2 (section 2.2.6), and according to previous studies on the mesoscopic structures of gel-like systems [75], the intensity "tail" which we observe at low q values is well described with a combination of scattering factors arising from static and dynamic density fluctuations which are typical, respectively, of the solid-phase and the liquid-phase. The static fluctuations usually result from an inhomogeneous distribution of cross-links: In our case the cross-links between the polymer chains are the hydrophobic domains formed by the hydrophobic end groups as well as the entangling of the main hydrophilic chains of the polymers. We can assume that, for hydrogels with high polymer concentration, i.e. 10 wt%, 15 wt% and 25 wt%, the number of cross-links is high and, therefore, the chain motions are impeded. Therefore, for polymer concentrations $\phi_{polymer} > 5$ wt%, we have a "hard gel" structure. In this case, the main contribution to the intensity fluctuations in the low q-region are the solid-like density fluctuations, i.e. the static scattering factor. Thus, in case of high polymer concentration the scattering function at low q-region is well described by the Debye-Bueche formalism, expressed in

the eq. 2.64 [67]. According to equation 2.64, the exponent of the scattering vector q is $p = 4$, which is in good agreement with the values which we have found for the high concentrated hydrogels (10 wt%, 15 wt% and 25 wt%) under investigation. On the other hand, at lower polymer concentrations $\phi_{polymer} < 5$ wt% we have the "dynamical gel" structure, where the hydrophobic end-groups dynamically move. In this case, the thermal density fluctuations become important contributors to the scattered intensity function in the low q-region. For this kind of homogeneous structure it is possible to employ the Ornstein-Zernike formalism to describe the scattering of the system in the low q-region (eq. 2.63) [66]. As seen in Fig. 5.2 the ideal exponent 2 is not observed in the analyzed concentration regime. Instead, we find an increase of the exponent value from 2.5 to 3.3 at polymer concentration of 0.48 wt % to 5 wt%. Such increase in the exponent can be interpreted as a change in the structure from a homogeneous "fluctuating" gel into the formation of a "hard" gel structure, where the micellar domains are closer and there are entanglements between the hydrophilic chains. Concerning the distribution of the hydrophobic domains formed by the end-groups of the HEUR polymer chains, it is possible to obtain information by plotting the peak position q_{max} of the SANS curves as a function of the polymer concentration ($\phi_{polymer}$). This plot is shown in Fig. 5.3.

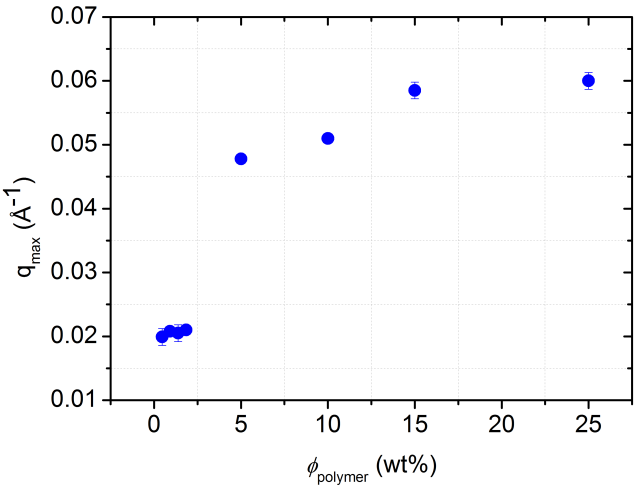

Figure 5.3.: Position of the correlation peak q_{max} in the SANS data, resembling the distance of hydrophobic domains, as function of polymer concentration ($\phi_{polymer}$). The error bars are almost of the same size of the symbols [102]

From the plot in Fig. 5.3 it is possible to observe an increase of the q_{max} position as the polymer concentration is increased. For the solution with $\phi_{polymer}$ between 0.46 wt% and 1.84 wt% we observed a shoulder instead of a peak in the SANS data shown in Fig. 5.1. The position of this shoulder is plotted in Fig. 5.3 as well. This shoulder does not

shift significantly in its position, i.e. from 0.020 $Å^{-1}$ to 0.021 $Å^{-1}$, increasing the polymer concentration ($\phi_{polymer}$). At $\phi_{polymer}$= 5 wt% the occurrence of the peak is observed at 0.048 $Å^{-1}$ and its position q_{max} increases up to 0.060 $Å^{-1}$ at $\phi_{polymer}$= 25 wt%. Increasing $\phi_{polymer}$ the polymer network becomes denser, because of the increase of cross-links (hydrophobic domains and entangling between the hydrophilic chains). Macroscopically, this effect can be observed by the increase of the viscosity of the hydrogel samples. This leads to a decrease of the domain spacing $d = 2\pi/q_{max}$ and, therefore, of the distance between the hydrophobic domains of the polymer network.

5.1.1. Rheology measurements on the pure HEUR aqueous solutions

As observed in the SANS profiles of the HEUR aqueous solutions at increasing polymer concentration (Fig. 5.1), when the concentration is increased from 1.80 wt% up to 5 wt% a visible correlation peak occurs. Furthermore, the exponent p of the scattering vector q in the low-q range, increases from ≈ 3 to ≈ 4 (Fig. 5.2), which is the typical value of solid-like structures [67]. This suggests that a structural change in the HEUR organization in water occurs when the polymer concentration is increased. To understand the nature of this *phase transition*, we performed rheology measurements on the HEUR solutions in the concentration range between 1 wt% and 5 wt%. In particular, we measured the flow curves, i.e. viscosity-shear rate curves, to understand which kind of fluid is obtained at a certain HEUR polymer concentration. We also measured highly concentrated gels, i.e. 10 wt% and 25 wt %. The obtained flow curves for the samples in the concentration range between 1 wt% and 3 wt% are shown in Fig. 5.4. The first evidence that we observe in the flow curves in Fig. 5.4 is an increase of the zero-shear viscosity η_0 with increasing HEUR polymer concentration.

For the lowest HEUR polymer concentration (1 wt%) we obtain a noisy profile of the viscosity as a function of the shear rate $\dot{\gamma}$. This is perhaps due to the very low viscosity values that are close to the transducer limit. On the other hand, when the concentration is increased to 2 wt % , we observe the typical HEUR polymer solution behaviour explained in the chapter 2 (paragraph 2.1.1, Fig.2.5). A newtonian regime is observed at low shear rates, slight shear thickening at $\dot{\gamma} \approx 40s^{-1}$ and at $\dot{\gamma} > 40s^{-1}$ a steep decrease of the viscosity is observed (highlighted by the magenta arrow in Fig. 5.4), due to shear thinning. The flow curve of the 3 wt% HEUR aqueous solution also shows the same features of the one of the 2 wt% sample, with shear thickening at $\dot{\gamma} \approx 70s^{-1}$. This indicates that a percolating network of bridged flower micelles already forms at concentrations higher than 1 wt%. Increasing the HEUR polymer concentration further, the viscosity dependence on the shear rate changes drastically. The obtained flow curves for the solutions at 4 wt%, 5 wt%, 10 wt% and 25 wt% are shown in Fig. 5.5

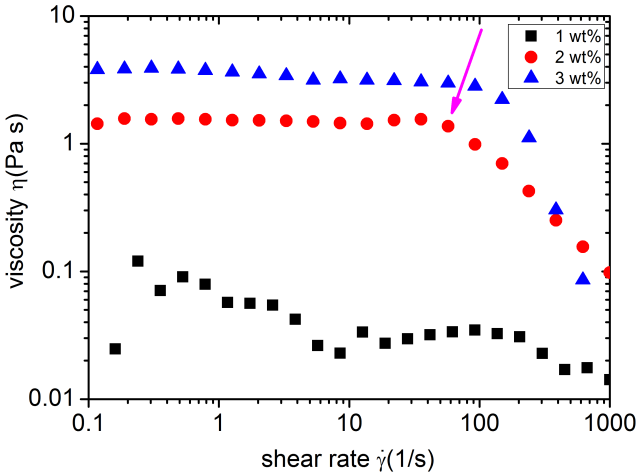

Figure 5.4.: Viscosity-shear rate curves for the HEUR aqueous solution with polymer concentration of 1 wt%, 2 wt% and 3 wt%. The error bars are smaller than the symbol size

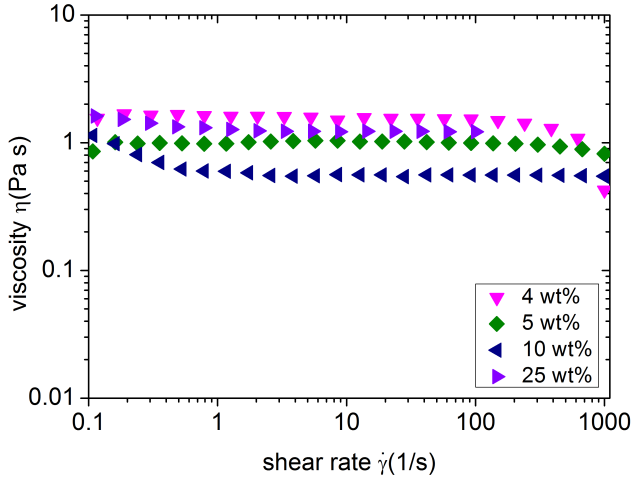

Figure 5.5.: Viscosity-shear rate curves for the HEUR aqueous solution with polymer concentration of 4 wt%, 5 wt%, 10 wt% and 25 wt%. The error bars are smaller than the symbol size

From the flow curve of the aqueous solution of HEUR at 4 wt% it is possible to observe a newtonian regime followed by shear thinning at shear rate of $\dot{\gamma} \approx 320s^{-1}$. The shear thickening effect has completely vanished. This phenomenon was also observed by Watanabe in his study on the concentration dependence of non-linear rheological properties of HEUR aqueous solutions [12]. He observed the absence of shear thickening at HEUR concentration $\phi \approx 4$ wt%. Since this concentration is similar to the concentration range in which we also observe the absence of shear thickening effect, we follow the same argu-

ment proposed by Watanabe to explain this change in the viscosity behaviour. Watanabe proposes that, the vanishing of the shear thickening effect is ascribed to the transition between a *sparse network*, composed of superbridges connecting the cores of flower-like micelles coexisting with single micelles, and a *dense network*, which is a well percolated network where all the chains are connected through the hydrophobic cores. In connection with the data of Watanabe et al, Iannirubertо and Marrucci propose a new interpretation for the lack of shear thickening in dense networks [113]. Their interpretation is based on the idea that dense networks have interpenetrating cores, while sparse networks have cores that are far apart. The presence of thickening in the latter, comes from the compression or collision between these cores when there is sufficiently strong flow. These collisions build in stress into the system and give rise to a slight increase in the viscosity (thickening). The lack of thickening can then be interpreted as an indication that the cores are already very closed and cannot be compressed. This means that for $\phi_{polymer} > 3$ wt %, the networks are now sufficiently dense. Increasing the polymer concentration further, we observe that the viscosity values decrease for polymer concentration $\phi > 3$ wt%, as shown in the plot in Fig. 5.6.

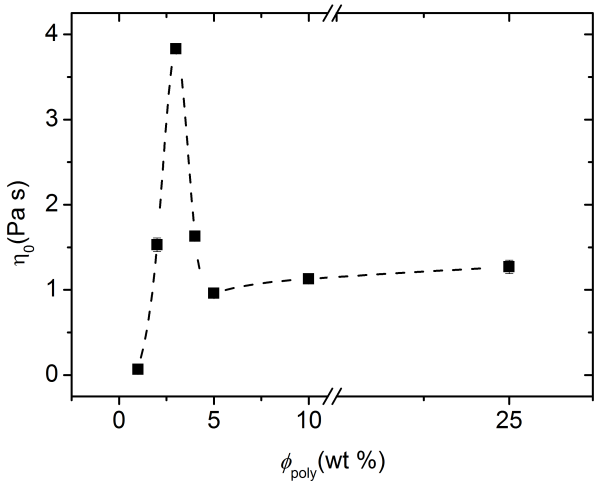

Figure 5.6.: Zero-shear rate viscosity η_0 as a function of the polymer concentration ϕ_{poly}. The error bars are smaller than the symbol size

In the flow curves shown in Fig. 5.5 at $\phi_{polymer}$ >4 wt%, the shear thinnig regime is completely lost in the measured shear rates, and we observe a constant viscosity with the shear rate. On the other hand, the decrease of the viscosity for concentrations much higher than the network formation concentration ϕ^* was explained by Semenov considering the fact that the telechelic chains forming the micelles are less stretched in a more concentrated gel. Therefore, it is easier for the micelles to change their shapes and the potential barrier

for rearrangement of the micelles is lower at higher concentration. The obtained behaviour of the viscosity as a function of the polymer concentration ϕ_{poly} (plot in Fig. 5.6) follows pretty well the theoretical prediction by Semenov [10]. The liquid-like behaviour observed for the HEUR solution at 25 wt% concentration is confirmed by the optical microscopy image shown in Fig. 5.7 which shows that there are dense polymer regions and pure water domains, meaning that when the polymer concentration is very high ($\phi > 5$ wt%), the gel ruptures and it gives rise to dense polymer domains. This ruptured structure is characterized by lower viscosity than the gel-like phase in the concentration range between 2 wt% and 4 wt%.

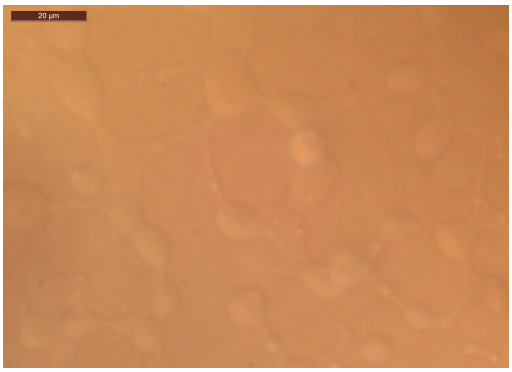

Figure 5.7.: Optical microscopy image of the ruptured hydrogel (25 wt% polymer) (scale bar 20 μm). The visible mesh-like network is composed of dense polymer networks and pure water domains [102]

Therefore, the results obtained from rheology allow us to ascribe the change in the SANS profiles from 1.80 wt% to 5 wt% HEUR polymer concentration to the transition from a sparse, less percolated network to a dense, well percolated network which gives rise to the correlation peak and to the increase of the exponent p of the scattering vector q, observed in the SANS data.

5.1.2. Scattering from polydisperse core-shell spheres applied on the SANS data analysis

The model based on the Teubner-Strey theory for the scattering of microemulsions (eq. 5.1) fits nicely our SANS data, although its use is based on the strong approximation that the systems under investigation present structural features similar to the ones of microemulsions (Fig. 2.22). Thanks to this fit model, we were able to extract two key-parameters which describe the investigated systems, such as the exponent p describing the gel fluctuations, and the domain distance d, resembling the distance between the hydrophobic domains of the HEUR network. Therefore, the SANS data analysis presented so far, can be also defined as "model independent". However, despite the complexity of the system, an attempt to describe it with a simple structural model can be done. In particular, we employed the description adopted Sarvesh and co-workers to describe hydrogels composed of telechelic polymers, based on the scattering from spherical polydisperse particles developed by Chen [58, 59]. The scattering intensity is given by the eq. 2.48, where the structure factor $S(q)$ depends on the hard sphere repulsion potential $SHS(q)$. In turn, it depends on the distance R_{HS} between the scattering centres, given by:

$$R_{HS} = \frac{2\pi}{q_{max}} \tag{5.2}$$

where q_{max} is the q values where the peak in the SANS data occurs [114]. In order to fit the SANS data of the investigated HEUR aqueous solutions with this model, we add an additional term to the scattering intensity of eq. 2.48, which is a power law that takes into account the gel fluctuations (paragraph 2.2.6). Therefore, the final fit equation reads:

$$I(q) = Aq^{-p} + NP(q)S(q) + bkg \tag{5.3}$$

The fits were obtained by fixing the SLD of the solvent (D_2O) to $\rho_0 = 6.34 \times 10^{-6}$ Å^{-2} and the SLD of the micellar core to $\rho_{core} = -4.89 \times 10^{-7}$ Å^{-2}. The latter is calculated by knowing the volume of the end alkyl chains, evaluated by Tanford [115]. The main structural parameters, such as the average core radius $\bar{R}_{core}$, the shell thickness t and the exponent p, are listed in the table 5.1, and the fit curves are shown in Fig. 5.8.

An additional fit parameter not reported in the table 5.1, is polydispersity index of the micellar core radii Zimm distribution σ. It decreases when the average core radius $\bar{R}_{core}$ increases. As seen in the table 5.1, the value of the exponent p of the q vector at low q-values, increases with increasing the HEUR polymer concentration, as observed in the plot 5.2 obtained by fitting the SANS data with the eq. 5.1. The exponent p approaches the value 4, typical of solid-like structures [67], when ϕ_{poly} >5 wt%. For the

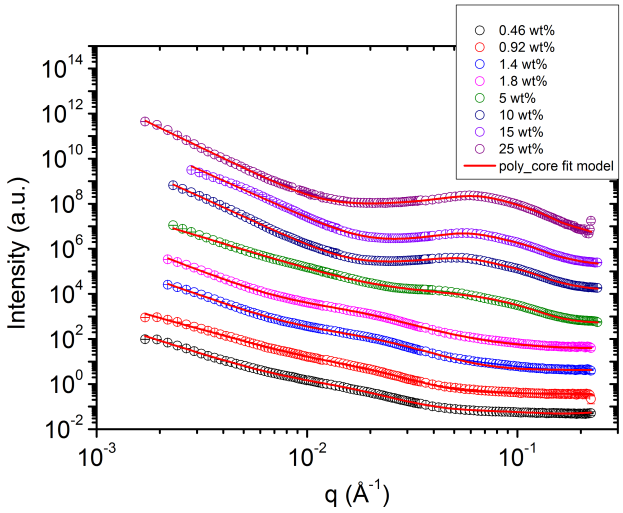

Figure 5.8.: SANS intensities as function of the scattering vector q of the HEUR aqueous solutions at increasing polymer concentrations. The black curve is to scale, and the other curves are shifted by powers of 10 along the y-axis for clarity of the presentation. The red solid lines represent the fit equation 5.3

dilute HEUR aqueous solutions, $\phi_{poly} = 0.46$ wt % and $\phi_{poly} = 0.92$ wt % we consider the structure factor $S(q)$ being the unity. Looking at the structural parameters such as the average micellar core radius $\bar{R}_{core}$ and the hydrophilic shell thickness t, we observe that the former slightly increases with increasing ϕ_{poly}, and it is consistent with the length of the alkyl chains of the HEUR polymers, being C_{14}. The non-dependence of the average core radius $\bar{R}_{core}$ on ϕ_{poly} is in agreement with the theoretical models developed for the associating polymers, according to which, the aggregation number N_{agg} of the micellar cores of the polymer network does not change significantly with increasing ϕ_{poly} [10,13,24]. On the other hand, we do not observe a clear trend of the shell thickness t with increasing

ϕ_{poly} (wt %)	ϕ (v/v)	$\bar{R}_{core}$ (Å)	t (Å)	ρ_{shell} (Å^{-2})	p
0.46	/	18.83 ± 0	56.32 ± 0.32	$(5.60 \pm 0.06) \times 10^{-6}$	2.76 ± 0.01
0.92	/	18.23 ± 0	59.60 ± 0.35	$(5.60 \pm 0.06) \times 10^{-6}$	2.62 ± 0.01
1.40	$(6.3 \pm 0.1) \times 10^{-5}$	18.80 ± 0	16.93 ± 0.31	$(9.80 \pm 0.08) \times 10^{-6}$	3.28 ± 0
1.80	0.0031 ± 0.0001	18.80 ± 0	20.12 ± 0.06	$(9.80 \pm 0.08) \times 10^{-6}$	3.58 ± 0.03
5	0.0050 ± 0.0001	18.80 ± 0	/	$(5.60 \pm 0.06) \times 10^{-6}$	2.87 ± 0.01
10	0.113 ± 0.0002	23.21 ± 0.01	22.17 ± 0.01	$(7.59 \pm 0.01) \times 10^{-6}$	4.34 ± 0
15	0.144 ± 0.0002	24.71 ± 0.026	20.85 ± 0.02	$(7.81 \pm 0.66) \times 10^{-6}$	4.17 ± 0.01
25	0.149 ± 0.0002	24.58 ± 0.03	17.08 ± 0.03	$(7.76 \pm 0.01) \times 10^{-6}$	4.26 ± 0.02

Table 5.1.: Parameters obtained by fitting the SANS data of the HEUR acqueous solutions with equation 5.3

ϕ_{poly}. Further, the SLD of the shell ρ_{shell} assumes unphysical high values. In the case of the dilute solutions at $\phi_{poly} = 0.46$ wt % and $\phi_{poly} = 0.92$ wt %, the shell thickness is consistent with half of the end-to-end distance of the hydrophilic portion of the HEUR polymer chain, being ≈ 54 Å [116]. Increasing the polymer concentration to $\phi_{poly} = 1.40$ wt %, the shell thickness drops down to $t = 16.9 \pm 0.3$ Å. Further increasing the polymer concentration to ϕ_{poly}=5 wt %, the shell thickness assumes freak value. Further increasing the polymer concentration up to 25 wt%, the shell thickness t assumes values of $\approx$ 20 Å. This change of the shell thickness t observed at $\phi^*_{poly} = 5$ wt % is most likely an indication of a structural change occurring in solution with increasing ϕ_{poly}. From the SANS curves of the HEUR aqueous solutions (Fig. 5.1) we have a first suggestion about the nature of this structural change: at $\phi_{poly} < 5$ wt % we observe a shoulder which shifts accordingly to the plot 5.3, while at $\phi_{poly} = 5$ wt % a very broad correlation peak occurs. The occurrence of the correlation peak in the SANS data is a signature of the formation of the dense HEUR network, where the hydrophobic domains are densely packed. Therefore, in this concentration range we observe the formation of the dense HEUR network from a sparse, or "dynamical" network. On the other hand, we could obtain reasonable values of the shell thickness for higher polymer concentrations, $\phi_{poly} > 5$ wt %. These values cannot be easily explained, however the eq. 5.3 fits nicely the data in this concentration range, i.e. between 10 wt % and 25 wt %. Here, we observe high values of the volume fraction ϕ of the cores: This value drastically increases from $\phi = 0.0050 \pm 0.0005$, for $\phi_{poly} = 5$ wt %, to $\phi = 0.149 \pm 0.0002$ $\phi_{poly} = 25$ wt %. This steep increase is an indication of the rupturing of the HEUR gel at high polymer concentrations. The gel rupturing is also confirmed by the decrease of the viscosity for $\phi_{poly} > 10$ wt % in the rheology data (Fig. 5.6). Furthermore, the formation of the dense HEUR network from an "open" network, was also observed in the collected rheology data at $\phi^*_{poly} = 4$ wt % (paragraph 5.1.1). Therefore, by combining the rheology results with the experimental evidence from the SANS curves, we can state that with the polydisperse core-shell model we were able to follow the formation of the dense HEUR network as well as we did by using the model based on the Teubner-Strey theory (eq. 5.1). Furthermore, we could obtain the structural parameters such as the the average micellar core radius $\bar{R}_{core}$ and the hydrophilic shell thickness t, and their dependence on the polymer concentration.

5.2. Structural investigation of the HEUR-MNPs nanocomposites

The inner structure of the nanocomposites in the hydrogel state was investigated with SANS as well. In order to compare the structural organization of the polymer-MNPs system in water by changing the polarity of the coating of MNPs, we investigated the following two types of nanocomposites in the hydrogel-state ($\phi_{polymer}$= 25 wt %):

- hydrogel nanocomposites with hydrophobic coated MNPs embedded
- hydrogel nanocomposites with hydrophilic coated MNPs embedded

We performed SANS measurements on the hydrogels with 4 different (hydrophobic and hydrophilic) MNP concentrations (ϕ_{MNP}) and we compared them with the reference system, which is thepure HEUR hydrogel without MNPs. The obtained SANS profiles are shown in Fig. 5.9 and Fig. 5.10.

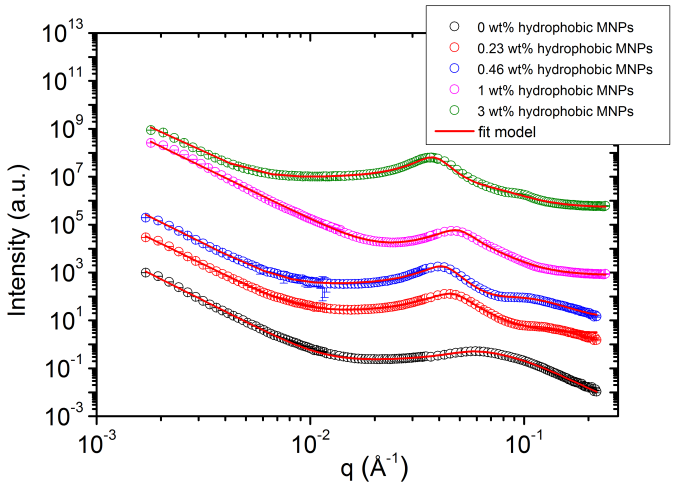

Figure 5.9.: SANS intensities of the nanocomposites hydrogels as function of the scattering vector q ($\phi_{polymer}$ = 25 wt%) at different hydrophobic MNP concentrations. The error bars have almost the same size of the symbols. The black curve is to scale, and the other curves are shifted by powers of 10 along the y-axis for clarity of the presentation. The red solid lines represent the fit equation 5.1 [102]

In addition to the hydrogel samples the nanocomposites in the dried state were investigated with SANS. We compare the scattering of the dry polymer film without MNPs embedded and the nanocomposites as dry films with 4 different hydrophobic MNP concentrations (ϕ_{MNP}), namely 0.23 wt %, 0.46 wt %, 1 wt % and 3 wt %, in order to observe an influence of the MNPs on the polymer structural organization in the dried state. The

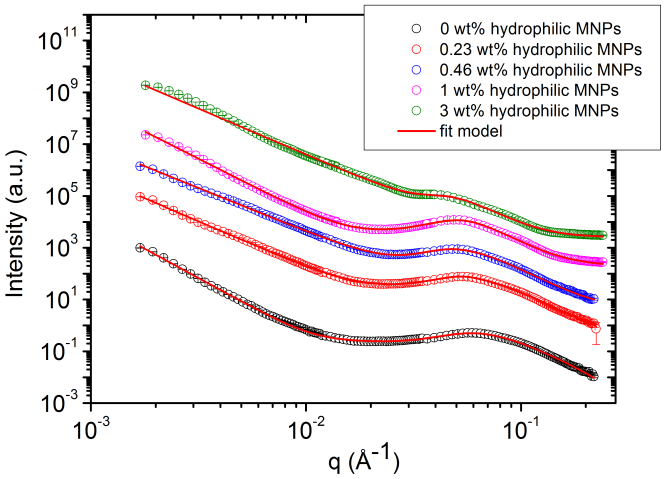

Figure 5.10.: SANS intensities of the nanocomposites hydrogels as a function of the scattering vector q of hydrogels ($\phi_{polymer} = 25$ wt%) at different hydrophilic MNP concentrations. The error bars have almost the same size of the symbols. The black curve is to scale, and the other curves are shifted by powers of 10 along the y-axis for clarity. The red solid lines represent the fit equation 5.1 [102]

SANS data obtained for the nanocomposites in the dried state are shown in Fig. 5.11 together with the corresponding fits.

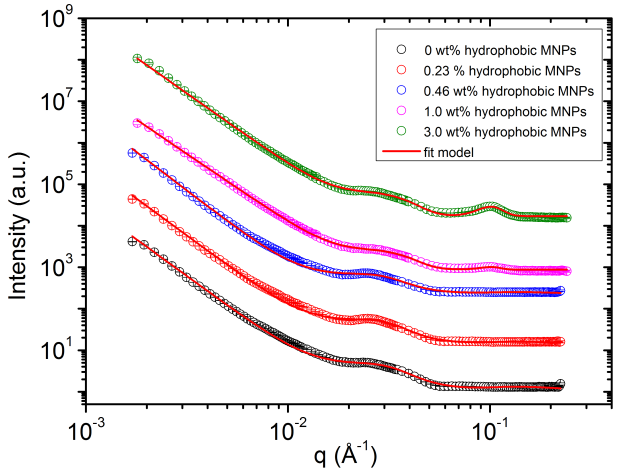

Figure 5.11.: SANS profiles of the dry films at different MNP concentrations. The error bars have almost the same size of the symbols. The black curve is to scale, and the other curves are shifted by powers of 10 along the y-axis for clarity of the presentation. The red solid lines represent the fit equation 5.1 [102]

The SANS data of all investigated nanocomposites, as hydrogels and as dry films, show

high scattering intensities at low q values ($q < 0.01$ Å^{-1}). Moreover, a correlation peak at $q_{max} = 2\pi/d$ in the intermediate q range is observed for all of them. Therefore, they have the same features of the scattering curves of the pure HEUR matrix, and they keep the similarities with the typical SANS profile of the microemulsions. Thus, we could extract the main structural information by fitting both sets of data with the model introduced above (eq. 5.1). We used this model because it fits the experimental data much more satisfactorily than the simpler "poly core-shell" model described in the paragraph 5.1.2. This is probably due to the high complexity of the investigated system, which, in this case, contains also the MNPs. The change in the slope p of the linear fit of the scattered intensity fluctuations in the low q-region and in the peak position q_{max} was evaluated as function of the MNP concentration ϕ_{MNP}. For modelling the scattering of the dry film, we added a Gaussian peak function to describe the presence of an additional peak in the SANS data at large q values (≈ 0.1 Å^{-1}) in the case of high MNP concentration (1 wt % and 3 wt %). We ascribe the occurrence of this peak to the presence of dense MNPs clusters, and its position resembles the inter-particles distance, being approximately the diameter of the MNPs core, i.e. ≈ 62.8 Å. Furthermore, in the case of the dry films, the peak observed at ≈ 0.03 Å^{-1} can be ascribed to a microphase separation between the different portions of the polymer chains, rather than to the bare distance between the hydrophobic domains of the polymer network. The Fig. 5.12 comprises the determined exponents p for the different systems as function of the MNP concentration (ϕ_{MNP}).

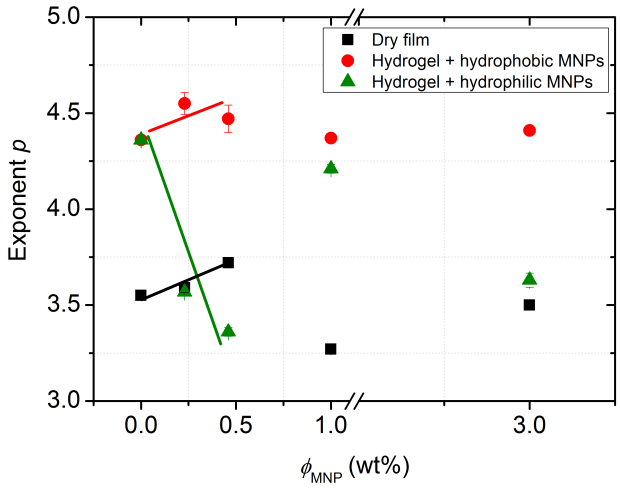

Figure 5.12.: Exponent p describing the fractal dimension of the polymer network as a function of the MNP concentration for all the investigated nanocomposites

As seen in Fig. 5.12, in the case of the hydrogels with hydrophobic MNPs embedded and of the dry films, the exponent p does only weakly depend on the MNP concentration.

In contrast, for the hydrogels containing hydrophilic MNPs the exponent decreases with increasing the MNP concentration and approaches the exponent of the "dynamical" gels, i.e. $p \approx 3.5$. Such behaviour can be explained by the interaction between the hydrophilic MNPs embedded in the polymer network, which leads to a decrease of the cross-links number. Macroscopically, this effect is visible from the decrease of the hydrogel viscosity, when the hydrophilic MNP concentration is increased. Additional insights are obtained from the structures seen with optical microscopy (Fig. 5.7). The optical micrograph shows that the dense polymer networks separate from regions of pure water. As a consequence, the addition of MNPs does not change the network structure dramatically. In the hydrophobic case, the network stays at the pure polymer hydrogel state even at higher MNP concentrations, while in the hydrophilic case, adding nanoparticles leads to a similar structure that finally is obtained in the dry state. More detailed structural information about the nanocomposites in the dried and in the hydrogel state are obtainable by plotting the peak position q_{max} of the SANS curves versus the MNP concentration ϕ_{MNP}, as shown in Fig. 5.13.

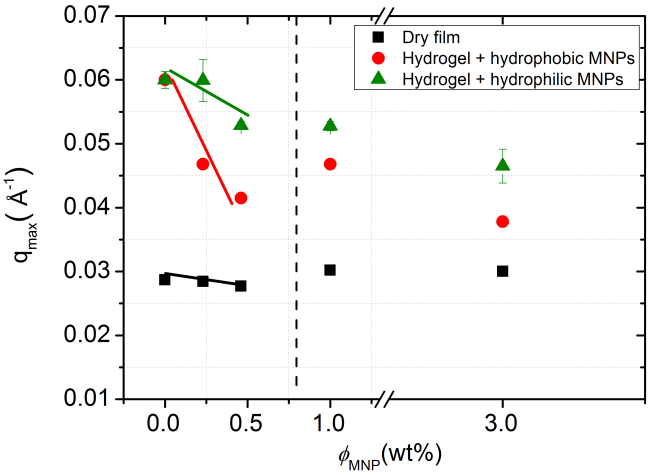

Figure 5.13.: Position of the correlation peak q_{max} in the SANS data resembling the distance of hydrophobic domains plotted as a function of the MNP concentration (ϕ_{MNP}) for the hydrogels (hydrophobic in red, hydrophilic in green) and dry films (black). The dashed line corresponds to the MNP concentration above which big and dense MNPs clusters are formed

A decrease of the peak position q_{max} and, therefore, an increase of the domain spacing $d = 2\pi/q_{max}$, increasing the MNP concentration (ϕ_{MNP}) is observed for both types of hydrogel samples (with hydrophilic and hydrophobic MNPs). The domain spacing d increases more drastically for the hydrogels containing hydrophobic MNPs than for the ones with hydrophilic MNPs. This slightly different behaviour is due to the different

interactions occurring between the polymer molecules and the two kinds of MNPs. The hydrophobic MNPs most likely interact preferably with the hydrophobic end-groups of the telechelic polymer and most probably they are embedded in the hydrophobic domains of the polymer network, which results in a considerably larger domain spacing due to the particle dimensions. On the other hand, the hydrophilic MNPs interact with the network in the aqueous phase, and most likely cut some connections between hydrophobic domains, which only results in a looser binding. Therefore, the influence of the hydrophilic MNPs on the hydrophobic domains of the HEUR network is not so important. This is the reason for which the decrease of the domain spacing d, which is related to the distance between the hydrophobic domains of the HEUR network, is weaker for the hydrogels containing hydrophilic MNPs. Concerning the nanocomposites in the dried state, the peak position q_{max} does not change drastically increasing the hydrophobic MNP concentration. The average domain spacing $d{=}2\pi/q_{max}$ is (217 ± 5)Å. TEM images of the nanocomposite in dried state with 1 wt% MNP concentration are shown in Fig. 5.14.

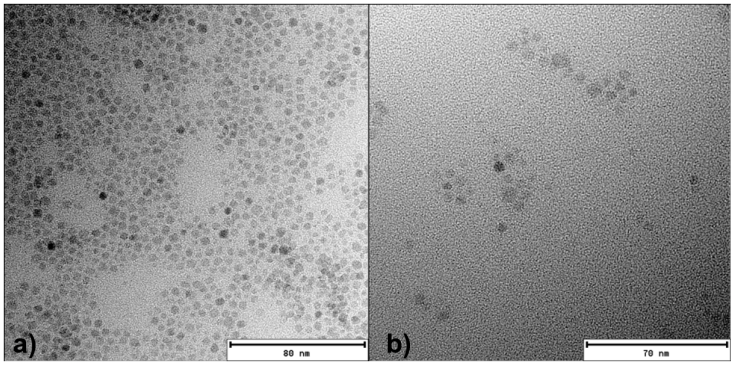

Figure 5.14.: TEM images of the nanocomposite in the dried state with 1 wt% MNP concentration. a) MNPs clusters distributed in the polymer matrix (scale bar 80 nm) b) small MNPs clusters and isolated hydrophobic MNPs with average size of 5 nm (scale bar 70 nm) [102]

The dry nanocomposite structure is characterized by the presence of clusters of single MNPs almost equally distributed in the polymer matrix (homogeneous part in the background). Besides these regions at high MNP density (Fig. 5.14 a)), there are regions with smaller clusters and single MNPs (Fig. 5.14 b)). The average domain spacing found in the SANS data is most probably an average of the distances between single MNPs and between the MNPs clusters. Indeed, in 5.14 a) it is possible to observe a mesh-like structure where the MNPs clusters are separated by the polymer matrix. The visible "holes" between the MNPs clusters have a length of approximately 25 nm. The same length can be found by measuring the distance single-single MNPs (Fig. 5.14 b)). The occurrence of the second peak at $q = 0.1$ Å^{-1} for the nanocomposite as dry film with 3 wt% MNP concentration (and slightly visible also in the SANS data of the dry film with 1 wt%

MNP concentration) is probably due to the increase of the number of big clusters with little or no polymer, which are characterized by a domain spacing (MNP-MNP distance) of roughly 6 nm. In general, the structural analysis can be summarized as following: At a MNP concentration around 0.8 wt% a phase transition occurs (see dashed line in Fig. 5.13). At concentrations below 0.8 wt% isolated MNPs are present, while at higher concentrations dense and large clusters of MNPs coexist with isolated nanoparticles. The hydrophobic MNPs are embedded in the hydrophobic domains of the network and the hydrophilic MNPs are inside the cross-linked network and thereby most likely cut some cross-links.

5.3. Magnetic response of the HEUR-MNPs nanocomposites as dry films

Magnetic response measurements were performed on the nanocomposites as dry films. Magnetic moments are measured as a function of the external magnetic field for the nanocomposites with different MNP concentrations at T = 300 K and T = 5 K. These data are shown in Fig. 5.15. The magnetization curves show the common S-shape with a very narrow hysteresis which becomes wider at low temperatures (T = 5 K). This temperature dependence of the hysteresis is the typical signature of a *superparamagnetic* behaviour (chapter 2, section 2.1.5), common to magnetic nanoparticles with diameters below the critical radius [46]. Such superparamagnetic behaviour was found in several other polymer composites with embedded iron oxide nanoparticles as well, as for example block copolymer matrices [117–119].

The saturation magnetization (M_s) increases with the increase of the MNP content in the nanocomposite. For the magnetic moments measured as a function of the external magnetic field at 300K a saturation magnetization of 0.0176 A m^2/kg is obtained for the nanocomposite with MNP loading of 0.23 wt%. It increases up to 1.27 A m^2/kg for the nanocomposite with 3 wt% MNP concentration. The coercitivity is very low ($\mu_0 H_c$ = 0.04 T) at 0.23 wt% MNP concentration and does not change with the increase of the MNP loading, indicating that the HEUR polymer matrix obviously does not affect the macroscopic magnetic anisotropy of the system and hence the overall alignment of the particle easy axes [120]. Further information about the magnetic properties and the size of the MNPs embedded in the polymer matrix are achievable by recording the zero-field cooling (ZFC) and the field-cooling (FC) magnetization curves [121]. The applied magnetic field is 0.01 T. The curves we obtained for the nanocomposites as thin dry films at increasing hydrophobic MNP concentration are shown in Fig. 5.16.

From the shape of the ZFC and FC curves one can extract several characteristics of

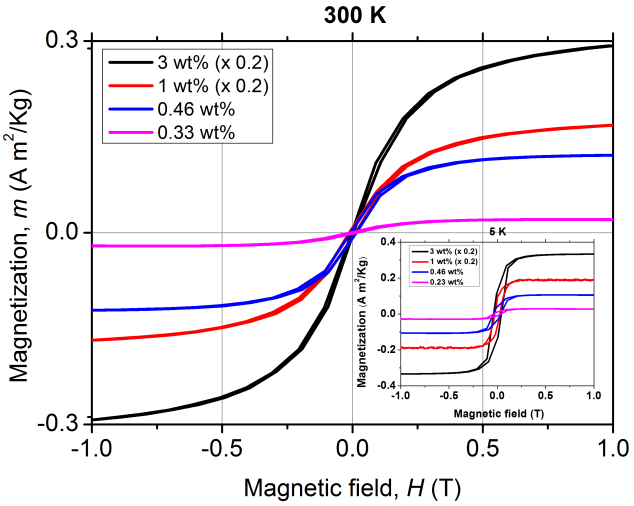

Figure 5.15.: Magnetization, m, measured as a function of the external magnetic field H of the dry MNP-HEUR nanocomposites at T = 300 K with different hydrophobic MNP concentrations. The inset shows the data at T = 5 K. The data of the nanocomposites with 1 and 3 wt% MNP concentration have been multiplied for a factor of 0.2 for clarity. The magnetic moment is normalized for the total nanocomposite mass [102]

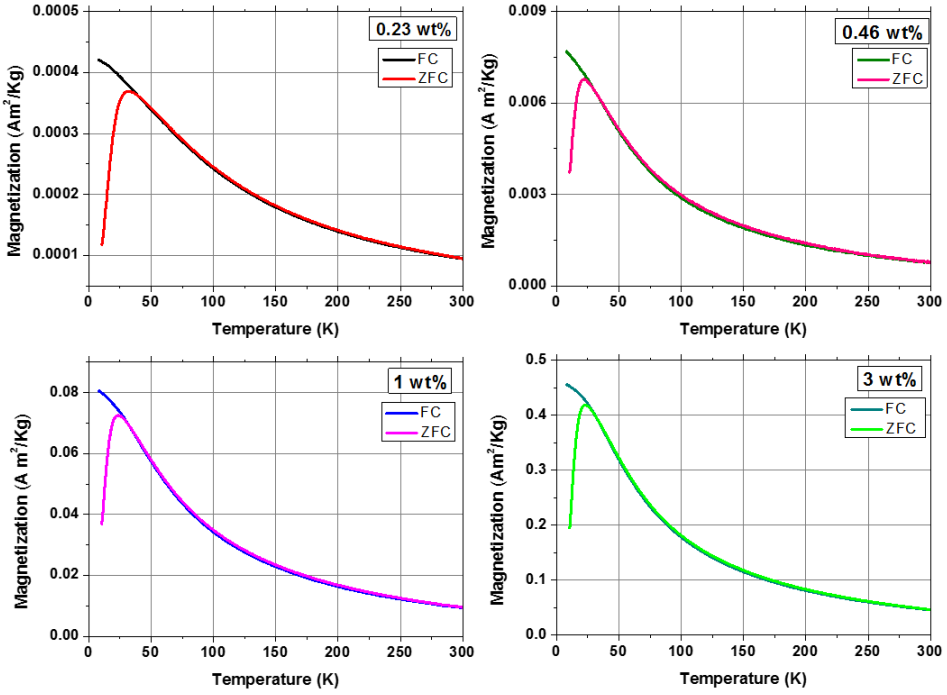

Figure 5.16.: Zero field cooling (ZFC) and field cooling (FC) curves of the nanocomposites with different hydrophobic MNP contents. The hydrophobic MNP concentrations are shown on the upper right side of each graph. The error bars are smaller than the line width [102]

the sample. The general shape of the ZFC curves typical of superparamagnetic (SPM) systems, is observed for all of the investigated nanocomposites with different MNP contents [122, 123]. The maximum in the ZFC curves marks the blocking temperature of the system, T_B. The blocking temperature does not change drastically with the increase of the hydrophobic MNP concentration in the polymer matrix. The high-temperature branches of both ZFC and FC above T_B display a typical $1/T$ Curie behaviour. The FC curve splits from the ZFC curve near the blocking temperature indicating a narrow particle size distribution. The blocking temperature of all the investigated samples is found to be (24.5 $\pm$ 3.1) K. Using this value one can estimate the size of the nanoparticles embedded into the polymer matrix, which give the superparamagnetic properties to the nanocomposite materials. In particular from the eq. 2.11, using $K = 29.7 \times 10^4$ J/m^3 [124] and T_B= (24.5 $\pm$ 3.1) K, the calculated MNPs radius is found to be (3.1 $\pm$ 1.1) nm. This value is in good agreement with the hydrophobic MNPs radius obtained by DLS measurements, that include the surfactant and the water layers (6.1 $\pm$ 0.3) nm. It seems that the separation of the hydrophobic MNPs by the surfactant (and possibly a little polymer) inside the dense clusters is enough to reach superparamagnetism. The complementary structural analysis would nonetheless favour the 0.46 wt% sample most for its homogeneity.

6. Dynamics of the HEUR-MNPs nanocomposites as hydrogels

In this chapter the results achieved from the dynamic characterization of the HEUR-MNPs nanocomposites as hydrogels are presented. Part of this chapter was published in the article "Multi-stage freezing of HEUR polymer networks with magnetite nanoparticles", *Soft Matter*, vol. 12, no. 13 pp. 3214-3225, 2016 [125]. Dynamic characterization was performed on the pure HEUR hydrogel and on the hydrogels with 0.46 wt%, 0.8 wt% MNP concentration. The dynamics of the same systems was investigated with two techniques: Dielectric relaxation spectroscopy (DRS) (paragraph 3.2.1 in the chapter 3) and neutron spin echo spectroscopy (NSE) (paragraph 3.2.2 of the chapter 3) measurements. DRS allows us to measure the imaginary part of the permittivity ε", also called dielectric loss, as a function of the frequency ω of the applied electric field, which is connected with the energy dissipation related to the dipole relaxations. The frequency range investigated by DRS is between 10^{-3} Hz and 10^{6} Hz. Therefore the investigated dynamics lies in the time range of milliseconds up to several seconds. NSE is a powerful tool to measure the coherent intermediate time-dependent scattering function, $S(q,t)$ on the time scale of several nanoseconds (10^{9} Hz), on the nanometer length scale. Even though these two techniques probe different time-scales, they often probe the same type of dynamics [126] [127], and can therefore complement each other in the study of the polymer dynamics. Besides these two techniques, the differential scanning calorimetry was also employed (paragraph 3.2.3). The DSC results are discussed before the DRS ones. The discussion continues with the presentation and the detailed discussion of the NSE results. Finally, the comparison between the DRS and the NSE results is made.

6.1. Differential scanning calorimetry analysis on the nanocomposites HEUR-MNP hydrogels

Differential scanning calorimetry measurements were performed on the investigated nanocomposite hydrogels in order to investigate the phase transitions occurring in the system. The preparation of the samples for the DSC investigation is reported in the paragraph 3.2.3. The DSC heating curve of the pure HEUR hydrogel 25 wt% (aq) is shown in Fig. 6.1 a). Starting from -160 °C, we observe the glass transition temperature (T_g) step which is enlarged in the inset in Fig. 6.1 a). The glass transition of the PEO portion of the HEUR polymer is observed for all nanocomposites as seen in Fig. 6.1 b). With increasing the MNP concentration, the T_g of the polymer slightly decreases from ∼-78 °C to ∼-84 °C. At higher temperatures, we observe an exothermic peak at -48 °C, which can be attributed to the cold crystallization of water [128]. The cold crystallization process was found in several kinds of polymer-water systems investigated by DSC, e.g. polysaccharide-water systems [129] [130]. It occurs typically when the material is cooled sufficiently fast, such that the crystallization dynamics is arrested before the phenomenon is completed during cooling. When mobility is regained during the subsequent heating, the crystallization process continues and gives an exothermic event. In particular, for the poly(ethylene glycol) (PEG)-water system, which is similar to ours, it was found that the cold crystallization of the water for a system containing ∼ 60 wt% of H_2O occurs at around -45 °C [129], which is in good agreement with the one we observe at -48 °C. At 4 °C, a deep endotherm occurs, accompanied by a shallower peak at -9 °C. They can be attributed to the melting of D_2O in the hydrogel. Please note that the heavy water (D_2O) is expected to have higher melting point than normal water [131]. Also in previous calorimetric studies on polymer membranes containing water, a "double" endotherm peak assigned to the melting of the water was found [132]. The peak at lower temperature was attributed to the melting of water clusters bound to the polymer, while the second one at higher temperature was associated to the "free" water molecules. i.e. those which are not directly bound to the polymer. It was found that in a poly(HEMA) hydrogel, the state of the water can be divided in three categories: interfacial, bound and bulk water [132]. The latter one crystallizes to ice and probably gives rise to the deep endotherm at 4 °C. The first two types supercool without crystallizing, remaining in the amorphous state, which is reflected by the presence of a glass transition. According to Pathnathan and Johari, the T_g of the supercooled water lies at -138.2 °C [132] and, according to Cerveny, at -113 – -115 °C for bulk water and around -100 °C for confined water (depending on the confining system) [133]. In our case, we observe it as a very weak step at -116 °C, highlighted in blue in the inset in Fig. 6.1 a). The thermograms of the nanocomposites present the same

phase transitions observed for the pure HEUR hydrogel 25 wt% (aq) and they are shown in Fig. A.2 in the appendix A, section A.2.

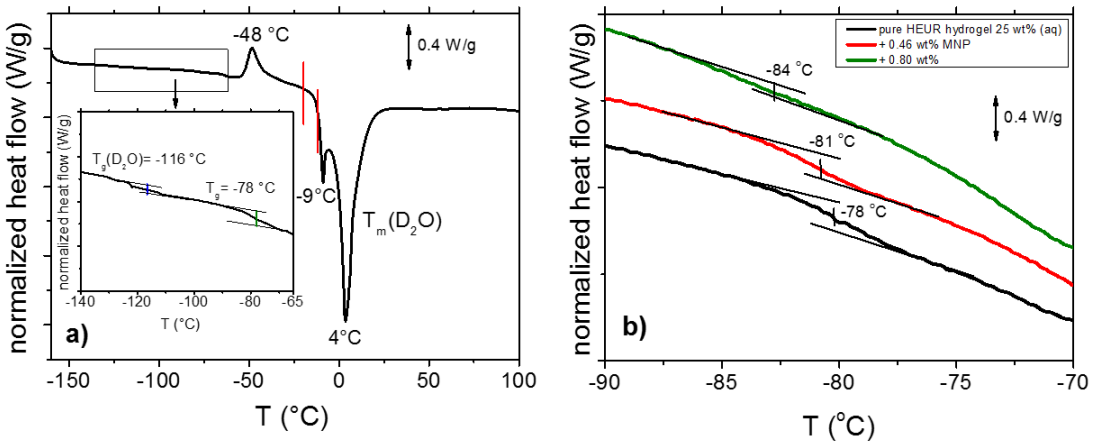

Figure 6.1.: a) DSC curve of the pure HEUR hydrogel 25 wt% (aq). For clarity, since we observed the same phase transitions for all the samples, we show only the curve of the matrix. In the inset, the glass transition temperatures T_g are highlighted in blue and green. The phase transition observed in the dielectric loss data is marked in red. b) Enlarged region in the glass transition temperature range for the all composite samples with increasing MNP concentration. The error bars are included in the line width [125]

6.2. Dielectric relaxation spectroscopy (DRS) analysis

The dielectric loss spectra recorded for the pure HEUR gel with 25 wt % (aq) are shown in Fig. 6.2 at the selected temperatures. At -95 °C a prominent dielectric loss peak occurs at $\omega_{max} \sim 100$ Hz for the pure HEUR hydrogel. Similar intense dielectric loss peaks have previously been found in other water containing systems, i.e. hydrogels [132], protein solutions [134], and hydrated PEO, where it was associated to the non-freezable water tightly bound to non-crystalline PEO segments [135]. Similar peaks were observed also in the dielectric relaxation spectra of ice [136–138]. According to Pathnathan and Johari, it is attributed to the thermally activated diffusion of molecules in supercooled water, which is identified as its α-relaxation process, and the relaxation peak is observed at 1 kHz at a temperature of -95 °C [132]. As observed in Fig. 6.2 (black curve, indicated by a black arrow) and in Fig. 6.4, in addition to the main relaxation peak and partially hidden by it, there is a shoulder at $\omega_{max} \sim 3$ Hz. In the same frequency-temperature range a relaxation peak was found for the poly(HEMA) hydrogel [132] and was attributed to the breaking and reforming of the H-bonds in the polymer network, defined as β-process. With increasing temperature, the contribution of the conductivity becomes visible, leading

to a "shoulder" at low frequency, i.e. $\omega_{max} \sim 0.1$ Hz, (see Fig. 6.2). Nevertheless, an additional relaxation can be detected at low frequencies ($\omega_{max} \sim 1$ Hz) concealed to a large extent by the conductivity slope at low frequencies. Further increasing the temperature, we observe a drastic change of the dielectric loss profiles which become flat in the low frequency range (0.01 Hz $< \omega_{max} <$ 1 Hz) and do not show any relaxation peaks in the higher frequency range, i.e. 10 Hz $< \omega_{max} < 10^5$ Hz. The transition temperature at which this change occurs is -15°C (Fig. 6.2).

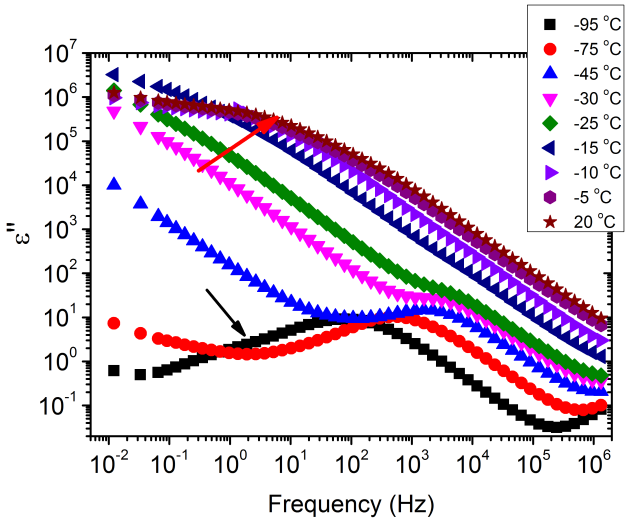

Figure 6.2.: Dielectric loss data of the pure HEUR hydrogel with 25 wt% (aq) in the temperature range between -95°C and 20°C. For clarity, only the curves at temperatures where significant changes in the DRS data occur are shown. The black arrow indicates the shoulder at $\sim$ 3 Hz at -95°C, and the red one indicates the "flat" profile of the DRS data in the low frequency range [125]

In order to follow more closely the temperature evolution of the relaxations, we plot the ε" values at selected fixed frequencies, as a function of the temperature, which are shown for the pure hydrogel in Fig. 6.3.

The step at $\sim$ -15 °C highlighted in Fig. 6.3 by a dashed line does not shift with frequency, meaning that in this temperature range a phase transition in the sample occurs. Looking at the DSC curve in Fig. 6.1 a), we observe that this temperature corresponds to the onset of the water melting (indicated by red lines in Fig. 6.1 a)). This means that the water melting in the gel is reflected in the dielectric loss spectra as a steep increase of the conductivity, as indicated by the high value of ε" ($\sim 10^6$) at low frequencies ($\omega_{max} \sim 1$ Hz) (indicated by the green arrow in Fig. 6.3). The high values of ε' ($\sim 10^6$) at low frequencies at temperatures above -25 °C is a sign of the electrode polarization process [139]. Therefore, the dielectric data between -25 °C and 25 °C, will not be

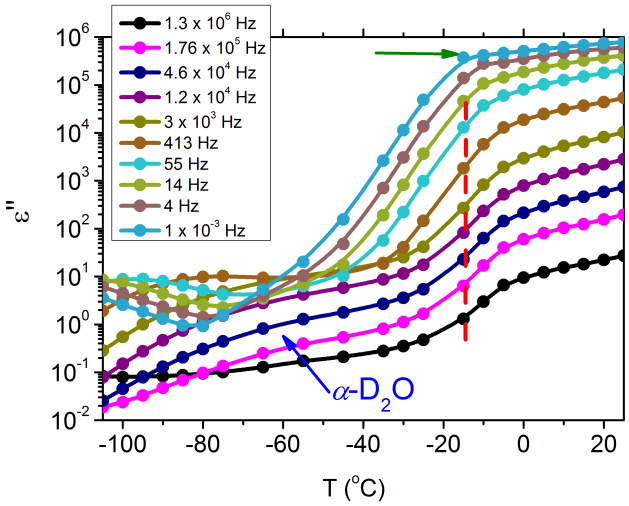

Figure 6.3.: Isochronal plot of the pure HEUR hydrogel 25 wt% (aq).The red dashed line indicates the position of the step at ∼15°C, indicating the phase transition observed in the DSC data. The error bars are smaller than the symbol size [125]

discussed in detail here. By comparing the dielectric loss data of the pure HEUR hydrogel with the ones containing MNPs, as done in Fig. 6.4, it is possible to observe the influence of the MNPs on the dielectric loss profile. We now focus on the effect of the MNPs on the α-relaxation of water. This relaxation is visible in a rather wide temperature range. In Fig. 6.4, the corresponding ε" peak is shown at two temperatures namely -95 °C and -65 °C. Interestingly, for the pure HEUR hydrogel and the hydrogel with 0.8 wt% MNP concentration, we observe only a very weak shoulder at ω_{max} ∼3 Hz (indicated by an arrow marked β in Fig. 6.4) at T= -95 °C. This peak is attributed to β-process. According to the frequency-temperature range, to the assignment done by Pathnathan and Johari for poly(HEMA) hydrogels [132] and to the relaxation process found by Huh and Cooper in polyurethane block polymers [140], this process is related to the motion of the dipolar segments –OH and –C=O along the C-O axis. The most prominent peak at -95 °C occurring at ω_{max} ∼100 Hz for the pure HEUR hydrogel and the one with 0.8 wt% MNP content is shifted to ω_{max} ∼20 Hz for the HEUR hydrogel with 0.46 wt% MNP. A similar shift is also observed at -65°C.

This shift is not well understood. In order to quantify our results in terms of time scales as a function of temperature, we performed a fitting procedure. The dielectric loss data were fitted by a sum of Havriliak-Negami (HN) model (eq. 3.23) [91]. From the fitting, we extract the relaxation time at maximum $\tau_{max} = 1/\omega_{max}$ (eq. 3.24). The contribution of the conductivity in the temperature range between -80°C and 25°C, is accounted for in the fit of the ε" spectra by including a term of the form: $i\sigma/(\omega^c\epsilon_0)$, where ε_0 is the vacuum

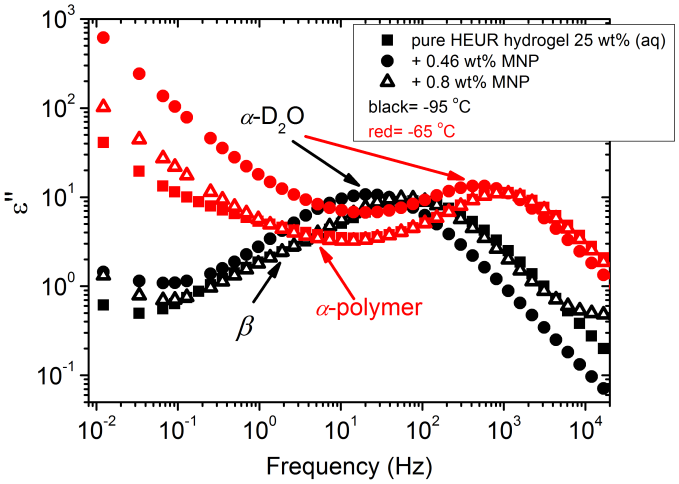

Figure 6.4.: Dielectric loss data at -95°C (black symbols) and at -65°C (red symbols) of all the investigated composites and the pure HEUR hydrogel. The error bars are smaller than the symbol size. The black arrows indicate the β-process and the α-process related to D_2O at -95°C. The red arrows indicate the α-process of the polymer and the α-process related to D_2O at -65°C

permittivity, σ the dc-conductivity of the material and c an exponent with a value close to 1. The dielectric loss data in the temperature range, i.e. between -100°C and -80°C , are fitted with two HN functions, namely the β-process and the α-process related to D_2O (the blue and the red peak in Fig. 6.5 a) respectively).

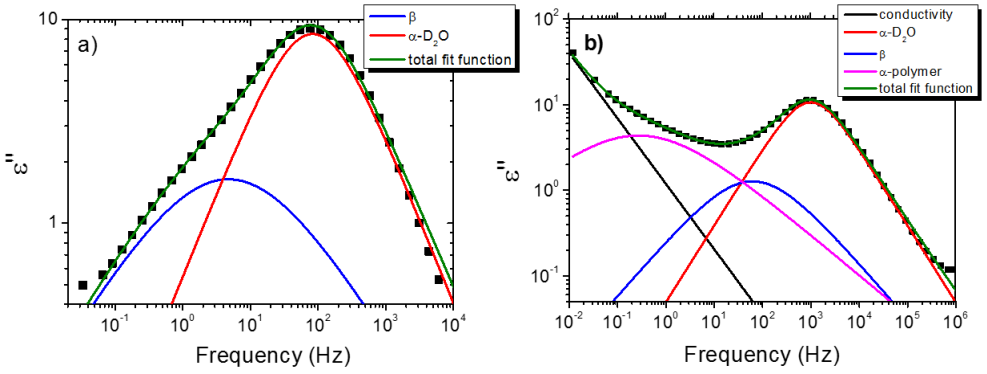

Figure 6.5.: Example of the fitting of the dielectric loss data of the pure HEUR gel 25 wt% (aq) at a) -100°C and at b) -65°C. The error bars are smaller than the symbol size. Details are explained in the text [125]

At higher temperatures, the dielectric loss data are fitted with three HN functions taking into account the β-process, the α-process related to D_2O and the α-process related to the polymer (magenta peak in Fig. 6.5 b)). The α-relaxation of the polymer starts to be visible at -70 °C. For fitting of the dielectric loss data at T > -80°C, the conductivity

contribution is also taken into account (black line in 6.5 b)). Fitting the dielectric loss data in this way allows us to construct the relaxation map, also called Arrhenius plot, of all the relaxation processes occurring in the temperature range between -100 °C and -25 °C (Fig. 6.6).

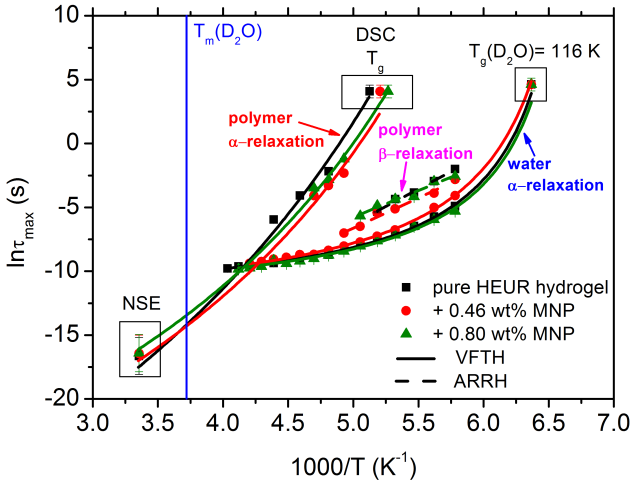

Figure 6.6.: Arrhenius map showing: the α-process related to the polymer chain including the NSE relaxation time at $q = 0.05$ Å^{-1} and the relaxation time at the T_g (100 s) (the green arrow indicates the increase of the curvature at 0.8 wt% MNP), the β-process and the α-process related to the supercooled water (α-water). The error bars are almost of the size of the symbols. The lines are VFTH fits and the dashed ones are Arrhenius fits. The vertical blue line indicates the melting of D_2O detected by DSC [125]

In the low temperature range, i.e. $-100°C < T < -25°C$, two processes are detected: one between -100°C and -25°C and another one between -100 °C and -75°C (visible up to -70°C for the sample with 0.46 wt% of MNPs). The first one is obtained collecting the relaxation times τ_{max} of the process shown in red in Fig.6.5 a) and b). Its temperature dependence follows the empirical Vogel-Fulcher-Tamman-Hesse (VFTH) model (eq. 2.66) characteristic of cooperative processes [141]. We therefore assign this relaxation to the α-process associated with the dynamic glass transition of the supercooled water.
On the other hand, the second low-temperature process, i.e. detected in the temperature range between -100°C and -75°C, shown in the fit examples in Fig. 6.5 a) and b) as the blue curves, follows the Arrhenius temperature dependence, characteristic of local, non-cooperative dynamics (eq. 2.65). The activation energies obtained from the fits are reported in the table 6.1. Because of the linear temperature dependence, the process occurring at low temperatures is a secondary process, usually related to localized motions of side chains. We assigned this process to the motion of the dipolar segments as –OH and –C=O along the C-O axis, namely the β-process. In our system, because of the presence

of water, H-bonds are present between the water molecules and the hydroxyl (–OH) and carbonyl (–C=O) groups of the polymer chains. Thus, the activation energy of the β-process is determined by the breaking and reforming of the H-bonds in the hydrogel network. As seen in the table 6.1, the activation energy E_A decreases with increasing the MNP concentration. This means that the rotation of the –OH and –C=O groups becomes "easier" in terms of energy barrier. This effect might be explained considering the blob model adopted for star polymers by Halperin [44]. As explained in the paragraph 2.1.3 in the chapter 2, according to this model, the polymer chain can be described in terms of "blobs", i.e. spherical regions occupied by segments of the polymer chain. The polymer concentration is higher nearby the branch point of the star polymer, which, in our case, is replaced by the hydrophobic domain. When the MNPs are added to the hydrogel, they interact mainly with the hydrophobic domains, being embedded into them. The increase of the hydrophobic domain size, due to the presence of the MNP clusters, leads to a "dilution" of the polymer concentration nearby the "branching point". Therefore, the "blobs" feel less constrains, and as a consequence also the rotation of the polar groups –OH and C=O becomes easier. The activation energies E_A of the β-process are shown in the table 6.1.

Sample	$T_{g,diel,D_2O}$ (°C)	T_{g,D_2O} (°C)	$T_{g,polymer}$ (°C)	$E_A(\beta)(kJ/mol)$
pure HEUR gel	-119 ± 2.3	-116	-78	45.5 ± 1.8
+ 0.46 wt %	-115.1 ± 2.2	-116	-81	39.2 ± 2.4
+ 0.80 wt %	-124.5 ± 5.2	-116	-84	34.6 ± 3.2

Table 6.1.: For each sample listed in the first column, the glass transitions T_g of the supercooled water (α-water) and of the polymer (α-polymer) and the activation energies E_A of the β-process for all the investigated hydrogels are reported

With increasing temperature, we observe an additional process in the temperature range between -70°C and -50°C for the hydrogels with 0.46 wt% and 0.8 wt% MNP concentration, and between -65°C and -35°C for the pure HEUR hydrogel (25 wt% (aq)), which is partially hidden by the conductivity and the α-water process. It is shown in one fit example in Fig. 6.5 b) (magenta curve). The relaxation time was measurable only in three temperatures and therefore it is not clear whether its trace in the activation plot (Fig. 6.6) is an Arrhenius or a VFTH one. Note however, that assuming a VFTH behaviour, it corresponds well to the points related to the glass transition of the polymer as observed by DSC. Hence, we assign it to the α-relaxation of the HEUR polymer, in particular to the PEO portion of the polymer chain [142,143]. We would like to point out that DSC shows a systematic acceleration of dynamics with MNP concentration (decrease of T_g, while DRS shows that the higher loading nanocomposite has slightly faster dynamics than its low loading counterpart. By extrapolating the fitted VTFH lines to the time $\tau = 100$ s,

we get a measure of the glass transition temperature related to the supercooled water, namely the dielectric glass transition temperature $T_{g,diel}$. The obtained values are shown in the table 6.1. These values are in agreement with the experimental T_g values obtained by DSC. The observed decrease of the T_g with increasing MNP concentration (Fig. 6.1 b)) indicates an acceleration of the dynamics at T$\sim T_g$, therefore at long relaxation times τ. This fact can be related to the change of the curvatures of the VFTH traces (Fig. 6.6). This curvature is often expressed in terms of the fragility index, which is a measure of the cooperativity of the dynamics, which reads:

$$m = \left.\frac{\mathrm{d}log\langle\tau\rangle}{\mathrm{d}(T/T_g)}\right|_{T=T_g} \tag{6.1}$$

where T_g is the glass transition of the glass-forming material and t is the relaxation time of the α-relaxation [144]. From the Arrhenius map in Fig. 6.6, we observe an increase of the cooperativity with increasing MNP concentration.

6.2.1. Conductivity data

In order gain insights into the correlation between the charge transport mechanism and the segmental relaxation (α-relaxation), the conductivity data collected in the DRS experiments turn to be useful. In Fig. 6.7, the real part of the conductivity σ' is plotted as a function of frequency at -55 °C.

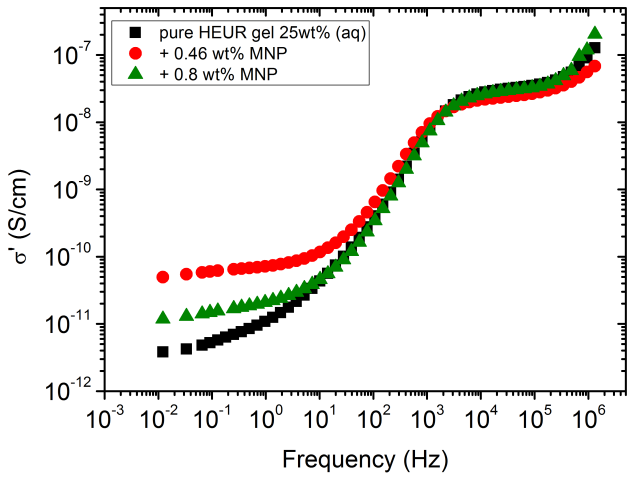

Figure 6.7.: Real part of the conductivity, σ' (Scm^{-1}), as a function of the frequency at -55 °C for the HEUR gels (25 wt% (aq)) for increasing MNP concentration. The error bars are smaller than the symbol size [125]

The plateau in the conductivity data at $\sim 10^{-1}$ Hz increases when MNPs are added to the pure HEUR hydrogel. However, for the intermediate MNP concentration (0.46 wt%), the plateau is higher than that for the composite having the highest MNP concentration (0.8 wt%). This suggests that the difference in the conductivity might be related to the difference in the polymer mobility (i.e. segmental motion) and not exclusively to the conductive nature of the MNPs [145]. Indeed, according to the classical theory [146] ionic conductivity in a polymer is inversely proportional to its segmental relaxation time τ_α. This means that ion motions are possible only when polymer segments undergo large amplitude rearrangements. In order to test this relation we compare the α-relaxation process and the conductivity of all samples. We plot the plateau value of σ' as a function of the relaxation times of the α-relaxation, τ_α, for all samples (Fig. 6.8).

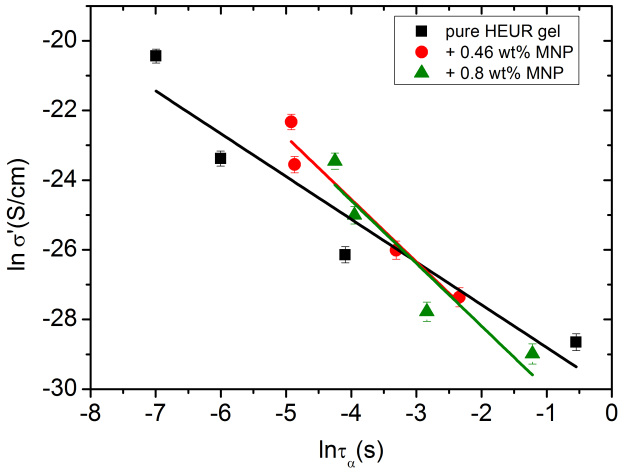

Figure 6.8.: Double logarithmic plot of the real part of the conductivity, σ' (S cm^{-1}), as a function of the relaxation times of the α-process, τ_α (s), for all the investigated gels [125]

The lines of the pure HEUR hydrogel and the nanocomposites do not coincide, meaning that a different relationship subsists between the conductivity and the α-relaxation for the pure hydrogel and for the nanocomposites. On the other hand, the traces of the nanocomposite gels in Fig. 6.8 coincide. This means that the α-relaxation of the polymer and the conductivity of the nanocomposites are directly coupled and they can be compared. Therefore, we can attribute the decrease of the conductivity observed for the nanocomposite with 0.8 wt% MNPs to a decrease of the segmental mobility of the polymer.

6.3. Neutron spin echo (NSE) measurements

In a neutron spin echo experiment, the normalized intermediate scattering function defined in the eq. 2.80 is measured. The probed intermediate scattering functions of the pure HEUR hydrogel measured at different q-values are shown in Fig. 6.9. The intermediate scattering functions of the nanocomposites hydrogels are shown in Fig. A.3 in the section A.2.2 of the appendix A.

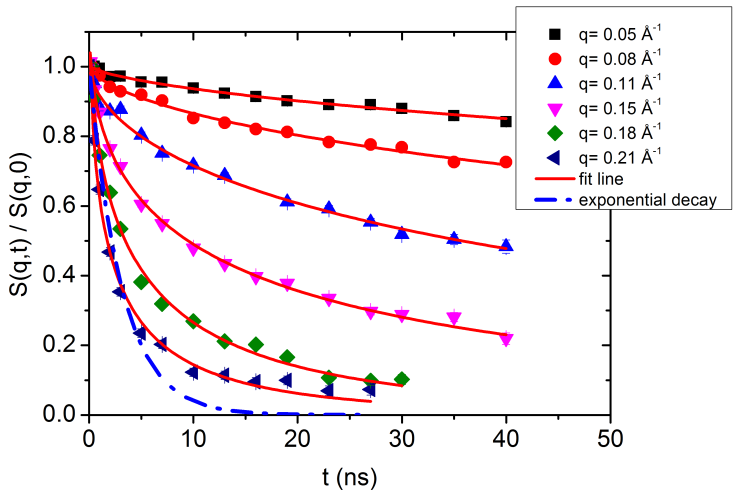

Figure 6.9.: Intermediate scattering functions of the pure HEUR hydrogel 25 wt% (aq). The error bars are almost of the size of the symbols. The red lines are the fitting curves (eq. 6.5) while the dashed line represents a simple exponential decay at $q = 0.21$ Å^{-1} [125]

The intermediate scattering functions of the pure HEUR hydrogel (25 wt% (aq)) decay exponentially with time in the q range between 0.05 Å^{-1} and 0.15 Å^{-1}, while for $q = 0.18$ Å^{-1} and $q = 0.21$ Å^{-1} they do not decay exponentially for longer Fourier times, as seen when comparing the data with a simple exponential decay (dashed line in Fig. 6.9). The same result is found for the HEUR hydrogels containing MNPs. For a better understanding the intermediate scattering functions at $q = 0.21$ Å^{-1} are compared in Fig. 6.10 for all investigated samples. It is observed that the time decay is slightly slowed down for the hydrogel with 0.8 wt% MNPs, i.e. the intermediate scattering function tends to zero more slowly than the one of the pure HEUR hydrogel. Detailed differences in the dynamic processes occurring in the investigated hydrogels in the nanosecond time-scale can be investigated by fitting the intermediate scattering function with an appropriate dynamic model. From Fig. 6.9, it is possible to observe that the intermediate scattering functions for $q > 0.08$ Å^{-1} clearly decay exponentially up to Fourier times of t $\sim$ 20 ns. In contrast, for longer Fourier times the decay is strongly delayed, and at $q = 0.18$ Å^{-1} and $q = 0.21$ Å^{-1} it reaches a plateu value within the observation time of the NSE

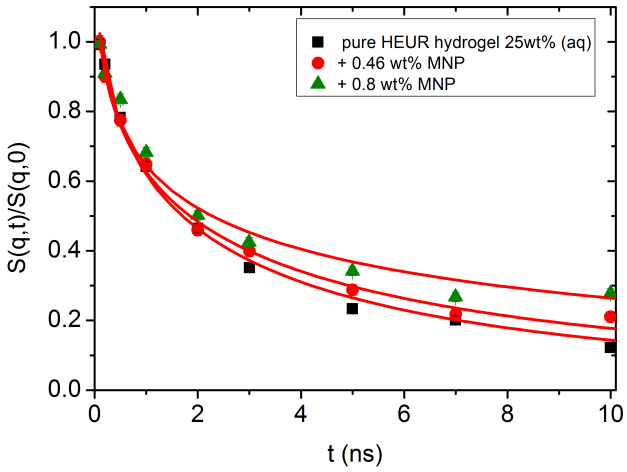

Figure 6.10.: Intermediate scattering functions of the pure HEUR hydrogel 25 wt% (aq) (black squares), with 0.46 wt% MNP content (red circles) and with 0.8 wt% MNP content (green triangles) in the time range between 0 and 10 ns at $q = 0.21$ Å^{-1}. The error bars are almost of the size of the symbols. The fit lines correspond to eq. 6.4 [125]

experiment. The origin of this effect arises from the gel structure. In fact, the dynamics probed by NSE is dominated by the segmental mobility of the polymer chain. However, in a gel-like network, cross-links and entanglements constrain the local segmental mobility of the chain, leading to a non-decaying intermediate scattering function. The scattering from these inhomogeneities such as crosslinks, entanglements and regions with different polymer densities gives an elastic contribution to the intermediate scattering function. This contribution was generally observed in polymer gels [75] and in our previous SANS investigation on the HEUR hydrogels with embedded MNPs (chapter 5) as an excess scattering, i.e. very high scattering intensity in the low-q region of $I(q)$ [147]. According to earlier studies on the mesoscopic structure of charged gels, [75] the scattering intensity in the low q-region of highly concentrated gels arises from solid-like density fluctuations, coming from an inhomogeneous distribution of crosslinks of the polymer network [147]. The scattering from these so-called *static inhomogeneities* can be described by an additional term included in the scattering function, which, according to the Debye–Bueche formalism, reads [67]:

$$S(q) = \frac{S(q=0)}{(1+\xi_s^2 q^2)^2} \tag{6.2}$$

where ξ_s is the correlation length of static density fluctuations. According to our scenario, this extra-scattering term arising from the static inhomogeneity was taken into account in the intermediate scattering function expression, in terms of a fraction of a non-decaying

components, $P(q)$. Therefore, the normalized intermediate scattering function expression reads:

$$\frac{S(q,t)}{S(q,0)} = P(q) + [1 - P(q)]F(q,t) \tag{6.3}$$

where $0 < P(q) < 1$ and $F(q,t)$ is the *stretched exponential function* (eq. 2.85).

In the case of the investigated HEUR hydrogels, the intermediate scattering functions shown in Fig. 6.9 are well fitted using the Zimm model for the segmental dynamics of polymers in solution. In particular, since we observed a time-decay up to Fourier-times of $t \sim 20$ ns, we used the limit of the short-time scale of the Zimm model, with $\beta = 0.85$. [76, 148]. Therefore, taking into account the contribution of the *static inhomogeneities* to the intermediate scattering function time-decay, the total expression of the intermediate scattering function used to fit our data reads:

$$\frac{S(q,t)}{S(q,0)} = P(q) + [1 - P(q)] \exp\left[-(\Gamma t)^{0.85}\right] \tag{6.4}$$

6.3.1. Interpretation of the NSE results

The relaxation rates Γ obtained from the fits with eq. 6.4 divided by the square of the scattering vector q give the diffusion coefficients of the diffusing objects in the investigated systems. By plotting Γ/q^2 as a function of the scattering vector q it is possible to investigate the probed dynamic regimes. The plot obtained for the investigated hydrogels is shown in Fig. 6.11. From the plot Γ/q^2 vs q shown in Fig.6.11 it is possible to observe two distinct dynamic regimes, i.e. two different dependence of the quantity Γ/q^2 with q:

- a *diffusive region* where $\Gamma \propto q^2$, in the q range between 0.05 Å^{-1} and 0.11 Å^{-1}, where the diffusion coefficient is a constant. In this case, the normalized intermediate scattering function reads:

  $$\frac{S(q,t)}{S(q,0)} = \exp[-(\Gamma t)] \tag{6.5}$$

  with $\Gamma = Dq^2$ whereas D is the diffusion coefficient of the diffusing objects. In our case, we observe the diffusion of the whole gel network, the so-called *breathing modes* [149].

- Zimm-like internal dynamic regime where $\Gamma \propto q^3$, in the q range between 0.15 Å^{-1} and 0.21 Å^{-1}. Indeed, the relaxation rate Γ_Z calculated in the Zimm model [88] is given by:

  $$\Gamma_z(q) = \frac{1}{6\pi}\frac{k_B T}{\eta_s} q^3 \tag{6.6}$$

  which represents a straight line in the plot in Fig. 6.11

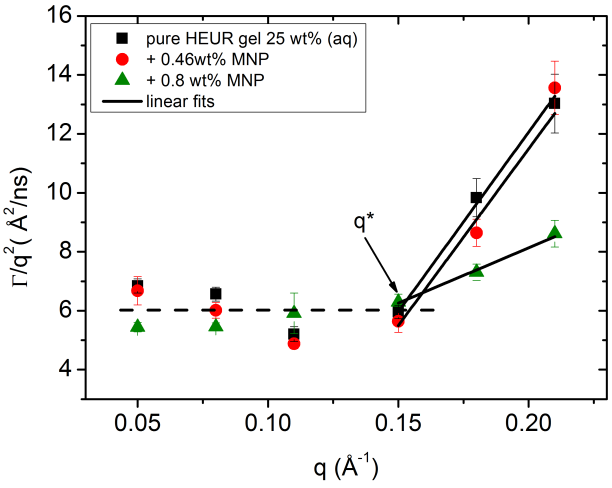

Figure 6.11.: Diffusion coefficients Γ/q^2 of the pure HEUR hydrogel (black squares), with 0.46 wt% MNPs (red circles) and with 0.8 wt% MNPs as a function of the q vector. The black lines are linear fits. The value q^* indicates the crossover between the simple diffusion and the segmental dynamics regimes [125]

The dynamic cross-over from the q^2 - to the q^3-regimes occurs at q^* (indicated by an arrow in Fig. 6.11), which is the length scale at which the two lines intersect, and it indicates the dynamic separation of the gel at large length scales and the blob scattering at smaller length scales. In simple gels, also called *topological* gel, this typical size corresponds to the size of the blob ξ, depicted in Fig. 2.8 a), which is the polymer chain between two topological cross links, $q^* = 1/\xi$. Therefore, this cross over length depends on the distance between the cross-links. In the case of the HEUR network, adopting the blobs model [25], the chain between two cross-links (namely the hydrophobic domains) can be divided in many blobs, which increase in size when the distance from the hydrophobic domain increases (Fig. 2.8 b)). In this case, the cross-over size represents the length l containing n blobs, $q^* = 1/l$. It corresponds to 42 Å, which is smaller than the hydrophobic domains distance measured by SANS, i.e. $d \sim 97$ Å (chapter 5). Furthermore, as seen in the plot Γ/q^2 vs q, the cross-over q^* does not depend on q, however from the structural characterization we found an increase of the distance between the hydrophobic domains of the HEUR network increasing the MNP concentration (chapter 5, paragraph **??**). We explain this experimental evidence considering the fact that the observed shift of the correlation peak q_{max} of the SANS profile, increasing the MNP concentration, is very small, i.e. ~ 0.015 Å^{-1}, therefore it does not affect significantly the cross-over value q^*. We focus now on the effect of the MNPs on the segmental dynamics of the polymer. In the *diffusion regime*, Γ is a constant function of the MNP concentration, ϕ_{MNP}. This can

be explained by assuming that the functionality f, i.e. the number of "arms" per micellar core, is constant, and, therefore, the entropic springs are the same. On the other hand, from the plot Γ/q^2 vs q (Fig. 6.11), we observe a decrease of the relaxation rate Γ in the *Zimm-like internal dynamic regime* when the MNP concentration is increased up to 0.8 wt%. This effect can be explained using two different interpretations. The first one involves the *blob* concept, and it considers the work of Halperin on star polymers [44]. It describes the field of blobs and the monomer density around their center. Close to the center of the star the blobs are small due to the higher polymer density, while in the remote regions the blobs are bigger. This principle is also true for our system where close to the hydrophobic domains the blobs must be smaller due to the high polymer concentration compared to the 'middle' region between the hydrophobic domains. Apart from the simple Zimm dynamics of dilute polymer solutions, the theory of Leibler et al. [150] describes the relaxation times within blobs of differing segment lengths, as in our assumption for the HEUR polymer network (Fig.2.8), like:

$$\tau_R \sim n^2 \tag{6.7}$$

with n being the number of monomers in the blob. In the q-range between 0.15 and 0.22 Å^{-1}, the largest blobs in the 'middle' region between the hydrophobic domains are highlighted, because they are the next neighbouring size in the system. According to the *blobs model* for star-shaped polymer [25, 44], the blob's size ξ is directly proportional to the distance from the center of the star (in our case the micellar core), r, and to the number of monomers within the blob, n. Therefore, in the case of a good solvent, the number of monomers in the blob is given by:

$$n \propto r^D \tag{6.8}$$

where D is the fractal dimension being 5/3 [151]. In our system, the distance r is proportional to the distance between the hydrophobic domains, i.e. *spacing* $d = 2\pi/q_{max}$. Therefore, according to the theory of Leibler et al. [150] the relaxation times should show the following proportionality:

$$\tau_R \propto [(d)^D]^2 \tag{6.9}$$

Therefore, the relaxation rate scales with the spacing like $\Gamma \sim d^{-10/3} \sim q_{max}^{10/3}$. The change of the SANS peak position q_{max} (paragraph 5.2, chapter 5) can now be compared to the different slopes in Fig. 6.11. Since we investigated by SANS only the nanocomposite

containing 1 wt% MNPs, we consider the q_{max} value at this concentration, which is close to 0.8 wt% (investigated by NSE). In particular we find that:

$$\frac{Slope1}{Slope2} \sim \left(\frac{q_{max1}}{q_{max2}}\right)^{10/3} \tag{6.10}$$

where Slope 1 and Slope 2 refer to the slopes of Γ/q^2 vs q in Fig. 6.11 for the pure hydrogels and for the hydrogel containing 0.8 wt% MNPs. In either case we observe a factor of about 3, which supports our viewpoint. Therefore, embedding of the MNPs within the hydrophobic domains of the polymer network leads to an increase of the size of the largest blobs.

A different point of view about the decrease of the slope in the plot Γ/q^2 vs q for the hydrogel with 0.8 wt % MNP concentration is based on the observation that the relaxation rate Γ in the Zimm-like regime, is inversely proportional to the viscosity of the solvent η_s, as seen in eq. 6.6. In a previous study on the cononsolvency effects on the structure and dynamics of microgels, in the case of partially collapsed microgel particles, a typical Zimm-like dynamic behaviour was found in the q-range between 0.08 and 0.18 $Å^{-1}$ [152]. By fitting the intermediate scattering functions with the Zimm model, the obtained solvent viscosity η_s was found to be seven times higher than the one of the pure solvent measured by capillary viscosimetry. This finding was explained as an effective increase of the viscosity, considering the *effective viscosity* being not barely the viscosity of the solvent, but rather of the medium made up of "solvent + other chains" in a highly crowded environment. Using the same argument, we can explain the decrease of the slope of Γ/q^2 vs q observed for the hydrogel with 0.8 wt% MNP concentration. We claim that, increasing the MNP concentration, we increase the *effective viscosity* of the medium composed of "solvent + other chains", which is now made up "solvent + other chains + MNPs". This effect is not already visible at 0.46 wt % because of the low MNP concentration. In order to obtain the solvent viscosity value according to the eq. 6.6, we performed the linear fit of the Γ/q^2 vs q data for the hydrogel with 0.8 wt%wt MNP concentration, fixing the intercept at 0, as in the pure $Zimm - dynamics$ regime. We found a solvent viscosity of $\eta_s = (0.00526 \pm 0.00040)$ Pa s, which is almost five times higher than the pure D_2O viscosity ($\eta_{D_2O} = 0.00125$ Pa s), which supports the *effective viscosity* interpretation.

6.3.2. Contribution of the *scattering inhomogeneities* to the total scattering function

The intermediate scattering functions of the investigated hydrogels were fitted with the eq. 6.4. From the non-decaying component $P(q)$ obtained from the fits, it is possible to calculate the static contribution $S_{st}(q)$ to the total scattering intensity $S(q)$ measured by us previously using SANS (chapter 5). Indeed, the total scattering intensity of a gel measured by SANS is given as an incoherent sum of the scattering from the static inhomogeneities, $S_{st}(q)$, and the scattering due to the thermal concentration fluctuations in the gel, $S_{th}(q)$ [153–156]:

$$S(q) = S_{st}(q) + S_{th}(q) \tag{6.11}$$

Thus, it is possible to calculate the static contribution $S_{st}(q)$ for the q values investigated using NSE from the relation:

$$S_{st}(q) = P(q) \times S(q) \tag{6.12}$$

The obtained static contribution $S_{st}(q)$ to the total scattering intensity $S(q)$ of all the investigated hydrogels is shown in Fig. 6.12.

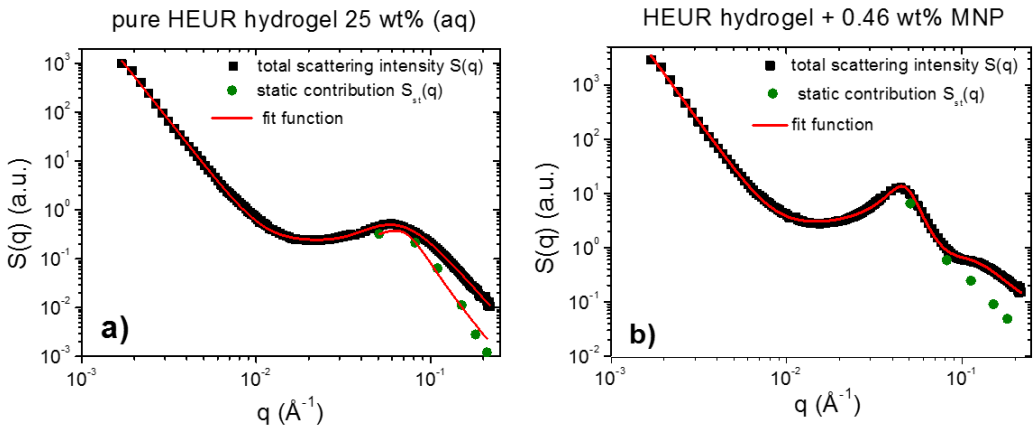

Figure 6.12.: SANS intensities of (a) the pure HEUR hydrogel and (b) the one containing 0.46 wt% MNPs. The green points represent the static scattering contribution S_{st}(q) to the total scattering intensity $S(q)$ (black squares). The error bars are smaller than the symbol size. The red lines represent the Teubner–Strey fits [125]

Despite the few q values for which it is possible to calculate $S_{st}(q)$ from the NSE data, it is possible to observe that $S_{st}(q)$ follows the shape of the $S(q)$ curve in the q-range where the correlation peak occurs, i.e. at $q_{max} \sim 0.062$ Å^{-1}. As explained in our previous SANS investigation (chapter 5) of the HEUR hydrogel nanocomposites, the scattering intensity $S(q)$ shows a correlation peak at $q_{max} = 2\pi/d$, where d is the domain spacing, i.e. the distance between the hydrophobic domains of the HEUR polymer network, having

a width proportional to $1/\xi$, where ξ is the correlation length of the density fluctuations of the dense polymer network [68]. The SANS data were fitted with a model where a simple power law describing the long range fluctuations and the Teubner–Strey (TS) theory [65] were combined. The latter theory is a thermodynamic approach with a simple order parameter indicating essentially two major phases, i.e. hydrophobic and hydrophilic domains. The used model for the fits of the SANS data of the HEUR-MNPs hydrogels is reported in the eq. 5.1. We focus now on the pure HEUR hydrogel, and analyse the correlation length calculated from the bare SANS intensities and that of the deducted static scattering contribution. The correlation length determined in the analysis of the overall SANS scattering is $\xi_{SANS} = (17.2 \pm 0.3)$ Å whereas the correlation length of the frozen density fluctuations is $\xi_{NSE} = (43 \pm 5)$ Å. In turn, this means that the system comes to a more structured state by the relaxation process. This suggests that the static scattering contribution $S_{st}(q)$ arises from a more ordered system than the one which gives the total scattering intensity $S(q)$, and it is therefore characterized by a longer correlation length ξ_{NSE}. The TS fits on the main correlation peak at $q_{max} \sim 0.062$ Å^{-1} cannot be performed for the static scattering contribution of the hydrogels containing MNPs, due to the interference of the second correlation peak of $S(q)$ at $q = 0.1$ Å^{-1} arising from the MNP clusters (Fig. 6.12 b)). This means that for the HEUR hydrogels containing MNPs, the MNP clusters contribute to the *frozen* inhomogeneities which cause the retardation in the time decay of the intermediate scattering function.

6.4. Comparison between the DRS and NSE results on the polymer segmental relaxation

The neutron spin echo (NSE) and the dielectric relaxation spectroscopy (DRS) probe the same type of dynamics, although at different time scales. Therefore it should be possible to compare the NSE and the DRS results on the segmental dynamics of the HEUR polymer for all the investigated hydrogels. The NSE results are summarized in Fig. 6.11, were the relaxation rate Γ is plotted as Γ/q^2 as a function of the scattering vector q. At $q > 0.15$ Å^{-1} we observe a decrease of the relaxation rate Γ for the sample with 0.8 wt% MNP concentration compared to the pure HEUR hydrogel. This we addressed to the change of the biggest blob size upon adding considerable MNPs to the system. From the activation energies of the β-relaxation (see Arrhenius plot in Fig. 6.6 and table 6.1) we see the similar trend of changing blob sizes just from the smallest blobs, that act on the polymer segments in terms of differing monomer density. So the evidence of the blob field as a function of the MNP concentration is found in both the DRS and the NSE results. Furthermore, we compare the relaxation times obtained with NSE, $\tau_{NSE} = 1/\Gamma$, with the relaxation

times of the α-relaxation obtained with DRS. Assuming that we probe the same kind of dynamics with DRS and NSE , i.e. polymer segmental motions, we would expect the τ_{NSE} in the segmental dynamics regime ($q > 0.15$ Å^{-1}) to follow the VTFH trend of the α-relaxation times obtained with DRS. Astonishingly, by plotting the τ_{NSE} in the activation plot in Fig. 6.6, we found that only the τ_{NSE} at $q < 0.15$ Å^{-1}, i.e. in the diffusion regime, follow the VFTH temperature dependence of the α-relaxation times. This indicates that the two techniques probe different length scales. Indeed, although the direct comparison between NSE and DRS data on the segmental dynamics has been made in some previous studies, it is still an open question [126, 127, 157]. On the other hand, quite astonishing was the conductivity, which increased strongly for the middle concentration of MNP, and dropped down for the highest MNP concentration. Apart from the blob interpretation we saw initial trends of interpretation from the conductivity/relaxation time plot (Fig. 6.8) that displayed different mechanisms for the system without and with MNPs. Following this plot (Fig. 6.8) on the fast relaxation times, and reading the relaxation times from the NSE data at higher q (Fig. 6.11), one would expect two steps: from 0 to 0.46 wt% MNPs the relaxation time does not change, but the mechanism of conductivity changes, which leads to a considerable increase of conductivity. From 0.46 wt% to 0.8 wt% of MNP concentration, the relaxation time increases, but the mechanism is identical, which leads to a moderately decreased conductivity. So, two competing trends finally can explain the conductivity dependence of our system.

7. Dynamics of the HEUR-MNPs nanocomposites as dry films

In this chapter, the results obtained from the dynamic investigation of the HEUR-MNPs nanocomposites in the dry state are presented. Part of this chapter has been published in the article "Dielectric relaxations of nanocomposites composed of HEUR polymers and magnetite nanoparticles", *Polymer*, vol. 96, pp. 70-80, 2016 [158]. The dynamic and the thermal behaviour of the nanocomposites as dry films was investigated and compared with the results achieved in the case of the hydrogels. As seen in the chapter 6, the MNPs influence the segmental dynamics of the HEUR polymer matrix for the hydrogel nanocomposites. In the following we will see whether the same kind of effect is observed in the dry state. We employed dielectric relaxation spectroscopy (DRS), which is a powerful tool for studying the polymer dynamics in a broad temperature and frequency range (chapter 3, paragraph 3.2.1). Along with the conventional alternating current (AC)-dielectric spectroscopy, we employed the technique of thermally stimulated depolarization current (TSDC) (chapter 3, paragraph 3.2.4). The results from the dielectric measurements are compared with those from differential scanning calorimetry (DSC) (chapter 3, paragraph 3.2.3), which was useful in investigating the thermal behaviour. First of all, the DSC results are presented, and some of the observed phase transitions were clarified through water sorption measurements. Then, the DRS data are presented and discussed and we relate the dielectric behaviour to the morphology of the system. We finally determine the relation between the polymer dynamics and the MNP concentration. A detailed discussion of the analysis of the DRS data in the low-frequency region is reported in the last paragraph of this chapter.

7.1. Determination of the water content: water sorption measurements

In order to characterize the presence of water in the polymer matrix of the dry films, the water content in the HEUR polymer film and in the nanocomposites was quantified by water sorption measurements. The confirmation of the presence of the water trapped in the prepared films and its quantification is important to understand the thermal and dielectric behaviour of the investigated systems. In Fig. 7.1, the evolution of the sample mass (pure HEUR film) with time during the water sorption process is shown.

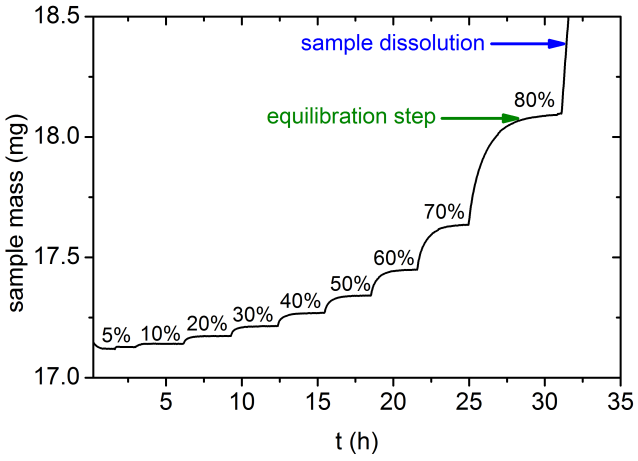

Figure 7.1.: Mass of the pure HEUR film as a function of the time at different relative humidity values *rh*, as indicated in the graph. The error bars are smaller than the line width [158]

The step-like increase of the sample mass is due to the water uptake during the water sorption process. For relative humidities rh between 5 % and 80 %, the mass vs time profiles reach a plateau within 2 h, i.e. they reach saturation within this time (green arrow in Fig. 7.1). For rh higher than 80 %, saturation is not reached, which is due to the fact that the sample starts to dissolve (blue arrow in Fig. 7.1). The sorption isotherm at 25 °C for the pure HEUR film is shown in Fig.7.2.

It shows the water content as a function of the water activity α_w or relative humidity rh.

$$h_d = \frac{m_w}{m_d} \tag{7.1}$$

where m_w is the mass of the absorbed water and m_d the mass of the dry sample. In the present case, the mass of the dry sample refers to the mass of the sample after vacuum drying at room temperature for 24 h. The data points marked by black squares are the ones which are out of equilibration during the sorption process, and the one marked by the

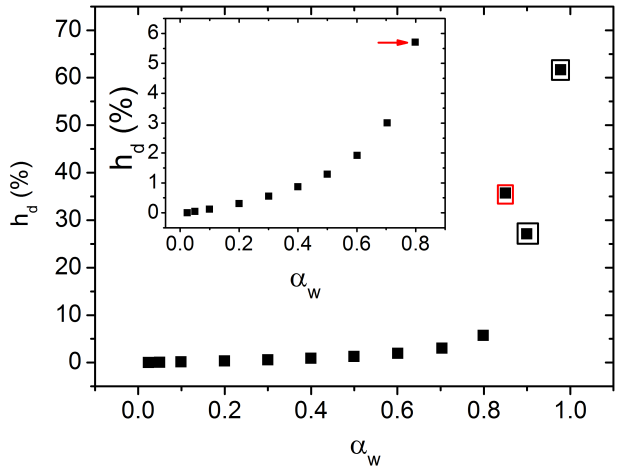

Figure 7.2.: Water content h_d (%) in the pure HEUR film as a function of the water activity α_w. The error bars are smaller than the symbol size. The inset graph is the sorption isotherm for the equilibrated steps. The red arrow highlights the water content at 80 % *rh*, the highest value where equilibrium is reached. The data points surrounded by black squares are the ones acquired out of equilibration during the sorption process, and the one marked by the red square was acquired during the desorption process [158]

red square is measured during the water desorption process. The sample absorbs up to 6% of water at $\alpha_w = 0.8$ (relative humidity $rh = 80\%$). Furthermore, the water content h_d vs the water activity α_w does not show a linear behaviour for $\alpha_w > 0.6$. This behaviour is typical of hydrogel systems and is due to the formation of clusters of water molecules [159]. Therefore, we can state that in usual conditions, i.e. in a relative humidity range rh of 40% and 80%, the pure HEUR film has a water content, h_d , between 1% and 6%. The water sorption measurements on the nanocomposites monitoring both, the sorption and the desorption process, imply that no hysteresis is observed for a relative humidity below 85%. In this case, the nanocomposite absorbs up to 6 % of water at $\alpha_w = 0.8$ (relative humidity $rh = 80$ %), as for the pure HEUR film, meaning that the presence of the MNPs does not influence the water uptake of the polymer matrix. The presence of water in all the investigated samples has to be taken into account in the investigation of their thermal behaviour and in the interpretation of their dielectric relaxation spectra.

7.2. Thermal behaviour: Differential scanning calorimetry (DSC)

The phase transitions of the pure HEUR polymer film and the nanocomposites with MNP concentration of 1 wt% and 3 wt% were followed using DSC. The DSC curves of all samples feature the same phase transitions at the same temperatures. Therefore, for clarity, in Fig. 7.3, the whole DSC curve (heating scans on the top and cooling scans at the bottom) is only shown for the pure HEUR film (the DSC heating curves of the nanocomposites are shown in Fig. A.4 in the section A.3.1 of the appendix A).

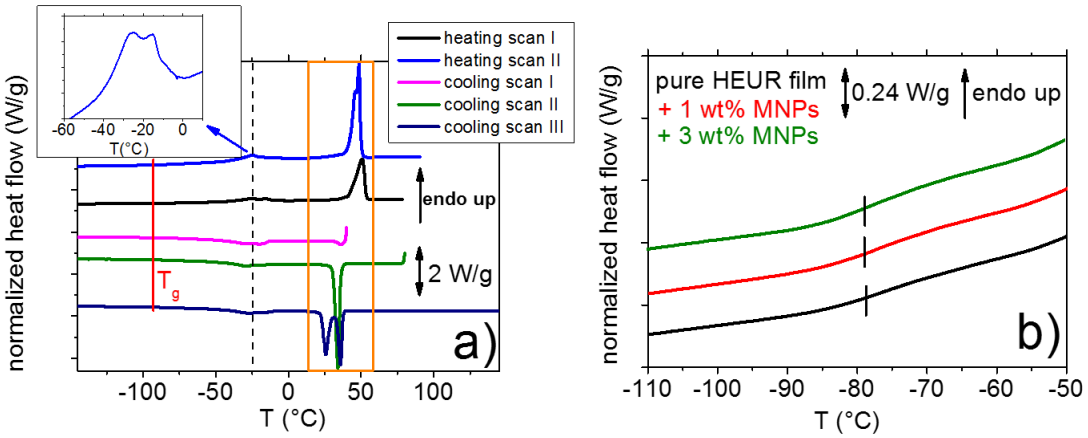

Figure 7.3.: a) DSC heating (scan I from -150 °C to 80 °, scan II from -150°C to 90°C) and cooling curves (scan I from 40°C to -150°C, scan II from 80°C to -150°C, scan III from 150°C to -150°C) of the pure HEUR film with 10°C/min. For clarity, the curves are shifted vertically. The dashed line indicates the melting/crystallization peak of the PEO crystallites at $\sim$ -22°C (the peak of the heating scan II is enlarged in the inset). The melting/crystallization peak of the crystalline PEO portion is highlighted by the orange rectangle. b) DSC heating thermograms showing the glass transition steps of the 3 nanocomposites. For clarity, the curves are shifted vertically. The glass transition temperatures T_g are calculated as the midpoint of the heat flow step and are indicated by short lines. For all the curves, the error bars are smaller than the line width [158]

In previous calorimetric studies on polymer membranes containing water [160], a very similar endotherm transition was found in the same temperature range. According to previous studies, one might tentatively assign the more intense endotherm peak at lower temperature to the melting of the water clusters bound to the polymer chains and the second one at higher temperature to the "free" water molecules which are not directly bound to the polymer. From the water sorption measurements, we find that, in the relative humidity range rh of 40% and 80% (which can be defined as usual conditions),

the investigated "dry" films contain a certain amount of water (h_d between 1% and 6%). Therefore, we might also ascribe the observed melting/crystallization peaks at ∼-22 °C to the water trapped in the polymer matrix. However, in order to clarify whether the origin of this endothermic transition at ∼-22 °C is related to the water content, we acquired DSC cooling curves starting from three different temperatures, namely 40 °C, 80 °C and 150 °C (curves I,II and III shown at the bottom in Fig. 7.3). The aim of heating up to different temperatures prior to the run is to affect the state of the water absorbed in the film. Especially for scan III, the sample was heated up to 150 °C in order to be sure that any "clustered" water was fully evaporated. In the cooling curves, the low temperature exotherm (corresponding to the "double" melting peak in heating) is located in all the scans in the temperature range between -40 °C and -10 °C. The fact that these phase transitions appear similar in shape and that they occur at the same temperature in all scans, irrespectively of the water content, suggests that they are not related to the crystallization or melting of water. These crystallization/melting peaks may rather be attributed to the PEO chains, or PEO crystallites, that experience constraints different from the bulk PEO phase, leading to a remarkably strong suppression of crystallization. It is worth noticing at this point that, contrary to what would be expected in such systems, these crystallization (in the cooling scan) and melting (in the subsequent heating scan) peaks appear at the same temperature. Probably, the polyurethane (PU) segments interact with these PEO chains, leading to the observed thermal behaviour. Due to the presence of these PEO crystallites, the system is quite heterogeneous. The well-known and documented crystallization/melting of PEO [161] is observed in all scans in Fig. 7.3 a) at 50 °C (orange rectangle in Fig. 7.3) indicating that the HEUR polymer is, at least partially, crystalline. The degree of crystallinity of the polymer can be calculated by:

$$X_c = \frac{\Delta H^*_{PEG}}{\Delta H^0_{PEG}} \tag{7.2}$$

Where ΔH^*_{PEG} is the enthalpy of fusion of the PEG portion of the HEUR polymer (0.095 kJ/g from the DSC curve) and ΔH^0_{PEG} the enthalpy of fusion of 100% crystalline PEG ($\Delta H^0_{PEG} = 0.19$ kJ/g) [162]. Similar DSC results were obtained for the nanocomposites. The degree of crystallinity, X_c (with respect to the total polymer mass) and the enthalpy of melting, ΔH_m, of all investigated samples are listed in table 7.1 and demonstrate that the addition of MNPs only slightly affect the degree of crystallinity. Also in the presence of the MNPs at concentrations of 1 wt% and 3 wt%, the crystallization/melting process of the small fraction of PEO displaying strong supercooling is observed between -40°C and -10 °C. Furthermore, the nanocomposites also show the crystallization/melting of the main crystalline PEO portion at $\sim 50°C$ and the glass transitions at $T_g \sim -75°C$, as shown in Fig. 7.3 b)). From the DSC measurements, we conclude that all the investigated systems

Sample	ΔH_m(J/g)	X_c	T_g (°C)	Δ c_p (J/g°C)
pure HEUR film	73.7 ± 2.2	0.37 ± 0.01	-79 ± 2	0.05 ± 0.01
+ 1 wt% MNPs	75.1 ± 2.3	0.38 ± 0.01	-78 ± 2	0.06 ± 0.01
+ 3 wt% MNPs	77.8 ± 2.3	0.39 ± 0.01	-80 ± 2	0.04 ± 0.01

Table 7.1.: Enthalpy of melting ΔH_m , degree of crystallinity X_c, calorimetric T_g and heating capacities from DSC of the pure HEUR film and of the nanocomposites with 1 wt% MNPs and 3 wt% MNPs

are very heterogeneous. They consist of a main crystalline PEO portion, a small fraction of crystalline PEO which crystallizes/melts at lower temperature, and an amorphous part which gives rise to the observed glass transition. The MNPs do neither seem to affect the relative proportions of these phases nor their dynamics. We only observe a slight increase of the crystallinity degree X_c with increasing the MNP concentration (table 7.1). This result is in agreement with the SANS data shown in the chapter 5 on the structural investigation of the HEUR-MNPs nanocomposites: The correlation peak at $q = 0.03$ Å^{-1} which is related to the domain size of the polymer structure, i.e. the distance between the hydrophobic domains formed by the alkyl end groups of the HEUR polymer, does not shift with increasing MNP concentration. Therefore, the morphology and the dynamics of the sample are nearly not affected by the presence of the MNPs.

7.3. Dynamic behaviour in the temperature domain: Thermally stimulated depolarization current (TSDC) measurements

In order to investigate the dynamics of the systems under investigation in the temperature domain, TSDC measurements were performed. The thermograms of the pure HEUR film and of the nanocomposites at two different polarization temperatures, i.e. $T_p = 20$ °C and at $T_p =$ -60 °C are shown in Fig. 7.4. At T $\sim$ 20°C, a very high depolarization current, I_n, is observed, and it reveals strong dc electrical conductivity for all the investigated samples. Besides the conductivity contribution, for all the samples, two dielectric dispersions are found. Starting from low temperatures, in the global TSDC thermograms obtained with $T_p = 20$ °C and $T_p =$ -60 °C, we observe a peak (indicated by an arrow in Fig. 7.4) at $\sim$ -75 °C for the pure HEUR sample and at $\sim$ -79 °C and $\sim$ -80 °C for both nanocomposites. This dispersion is attributed to the so-called α]-relaxation of the polymer, corresponding to the dynamic glass transition of the amorphous PEO, and its peak temperature is a good measure of the calorimetric T_g [163, 164].

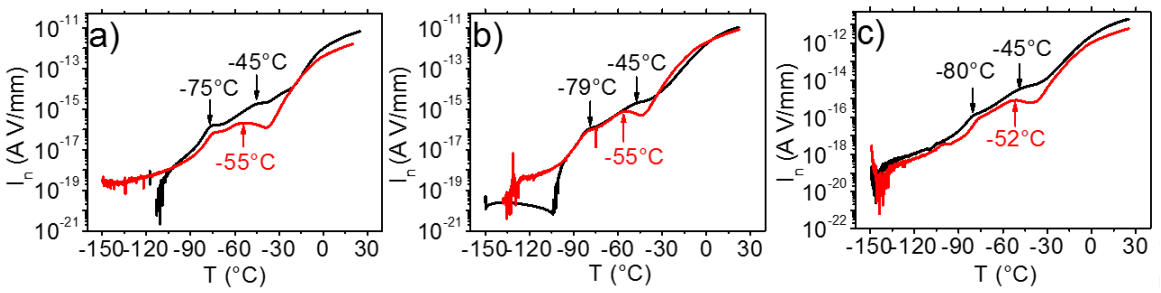

Figure 7.4.: TSDC thermograms of a) the pure HEUR film,b) the nanocomposites with 1 wt% MNPs and c) with 3 wt% MNPs polarized at $T_p = 20$ °C (black curve) and at $T_p =$ -60 °C (red curve). The error bars are smaller than the line width. The peak temperatures dispersions are annotated [158]

In contrast to the TSDC results, no decrease of T_g with increasing MNP concentration is observed in the DSC data (Fig. 7.3 b)), but rather a step at $\sim$ -75°C for all the samples. We need to consider that the dispersion peak in the TSDC thermograms is affected by the depolarization current; thus, the observed decrease in the peak temperature cannot be attributed to a decrease in the glass transition of the amorphous PEO in a straightforward manner. At higher temperatures, an additional dispersion is observed with the peak temperature depending on the polarization temperature, T_p: It is located at $\sim$ -45°C for $T_p = 20$°C, and at $\sim$ -55°C for $T_p =$ -60°C, indicated by the arrows in Fig. 7.4. The dependence of the position of this process on the polarization temperature implies that

a charge polarization process may contribute to the electric dispersion. We also need to consider that the temperature at which this dispersion occurs corresponds to the onset of the melting/crystallization process at ∼ -40°C, as detected in the DSC measurements (Fig. 7.3 a)). We remind here that we attributed this process to the melting/crystallization of strongly supercooled, small PEO crystallites that coexist with the main crystalline PEO phase and the amorphous PEO phase. Therefore, at this temperature, the sample is strongly heterogeneous. Thus, the detected dispersion at ∼ -45°C may be attributed to a dipolar-like process as the Maxwell-Wagner-Sillars (MWS) polarization which usually occurs in samples which are microphase-separated [165].

7.4. Dynamic behaviour in the frequency domain: Dielectric relaxation spectroscopy (DRS) measurements

The dielectric relaxation spectroscopy measurements were performed in order to investigate the molecular dynamics of the systems. The dielectric loss spectra of the pure HEUR film at selected temperatures are shown in Fig. 7.5. The dielectric loss data of the nanocomposites are shown in Fig. A.5 in the section A.3.2 of the appendix A.

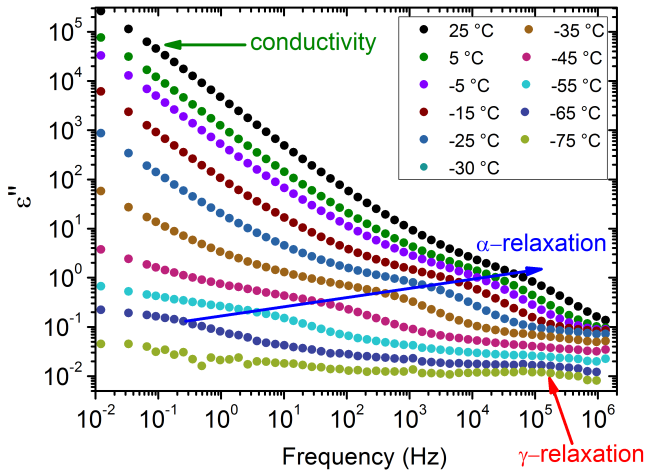

Figure 7.5.: Dielectric loss (ϵ'') data of the pure HEUR film. The error bars are smaller than the symbol size. The blue arrow indicates the segmental relaxation of the polymer (α), the red one the secondary γ-process and the green one the conductivity contribution [158]

Following those spectra starting from low temperatures, we observe between -85°C and -45°C a weak relaxation process at frequencies of ∼ 10^5 Hz. This process is attributed

to the crankshaft motion of the methylene sequences in the PEO chain [142, 166], often termed as the γ-relaxation. At -65°C, a stronger relaxation enters the experimental window from the side of low frequencies. The α-relaxation in PEO has previously been observed at –50°C at $\sim$ 100 Hz [143]. Since the observed relaxation process is located in the same frequency range, we ascribe it to the α-relaxation of the amorphous PEO portions in the HEUR polymer, associated to its dynamic glass transition. At even lower frequencies (0.01 Hz – 1 Hz) and higher temperatures, a steep decay related to the DC-conductivity dominates the spectra, especially between -20°C and 25°C. In the following, we will show that more relaxations coexist in the DC-conductivity dominated region. At this point, we would like to stress, that none of the three secondary relaxations, δ, γ and β that are typically observed in PU-based systems [140] are found in the present systems. Instead, the dielectric spectra are dominated by the PEO contribution. By comparing the dielectric loss data (ε") of the three films with increasing MNP concentration at the same temperature, it is possible to observe differences in the dielectric behaviour of the systems. For instance, in Fig. 7.6, we show the dielectric loss data of the three films at -45°C. It is possible to observe an increase of the imaginary permittivity ε" in the low frequency range (0.01 Hz-1 Hz) as well as a moderate shift of the relaxation "shoulder" (black arrow in Fig. 7.6) to higher frequencies with increasing MNP concentration. This may be related to an acceleration of the segmental dynamics in the presence of nanoparticles, but may also just be an apparent acceleration due to the influence of the increased conductivity in the dielectric spectra of the nanocomposites.

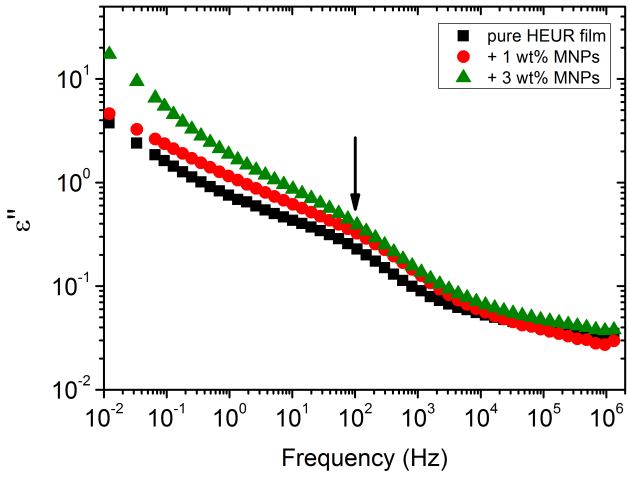

Figure 7.6.: Comparison of the dielectric loss data, ε", of the 3 samples with increasing MNP concentration at -45°C. The error bars are smaller than the symbol size. The black arrow indicates the position of the shoulder related to the α-process

7.4.1. Analysis of the DRS results

In order to quantify the effects on the segmental mobility and to investigate in detail the frequency region dominated by the conductivity, we performed an analysis based on fitting appropriate model functions. The dielectric loss spectra were fitted by a sum of Havriliak-Negami (HN) model function terms (eq. 3.23). From the data fitting, the relaxation time at the maximum of the processes, $\tau_{max} = 1/\omega_{max}$, is extracted from eq. 3.24. The effect of the conductivity in the temperature range between -80°C and 25°C was accounted for in the fit of the ε" spectra by including a term of the form: $i\sigma/\omega^c\varepsilon_0$, with σ being the DC-conductivity of the material and c is an exponent with a value close to 1 [91]. We fitted all the data by one relaxation process for the data collected between -35°C and 25°C and two relaxation processes for the data collected at lower temperatures, i.e. -45°C, -55°C and -65°C. Two examples of the fit with two relaxation processes at -45°C and at -65°C for the pure HEUR film are shown in Fig. 7.7.

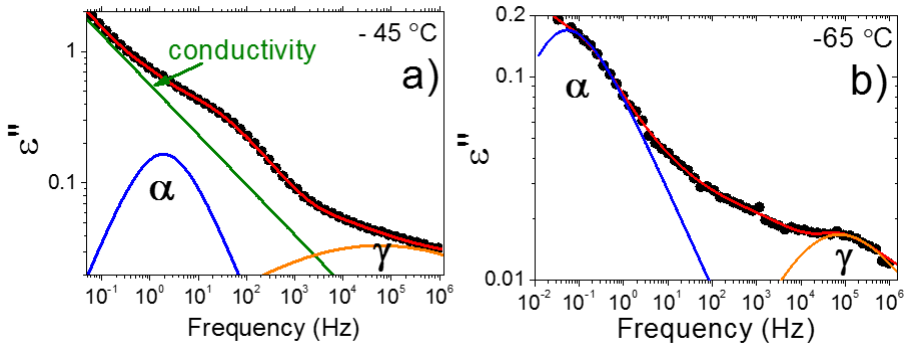

Figure 7.7.: Example of the fitting curves for the pure HEUR film at a) -45°C and b) -65°C. At -45°C, the contribution of the conductivity is shown. The error bars are smaller than the symbol size. At -65°C, the contribution of the γ-relaxation is better visible (the contribution of the conductivity is not shown in order to emphasize the contributions of the relaxation processes) [158]

The results about the involved time scales, τ, are given in an Arrhenius map in Fig. 7.8. For comparison, in the same plot, we also include the temperatures of the TSDC peaks, at the equivalent relaxation time of 100 s.

The γ-relaxation follows the Arrhenius behaviour described in the eq. 2.65. This confirms its local nature.

On the other hand, for all the samples, the main relaxation process occurring in the whole analyzed temperature range shows the Vogel-Fulcher-Tamman-Hesse (VFTH) temperature dependence (eq. 2.66), typical of cooperative processes, i.e. the α-process (dynamic glass transition) [91].

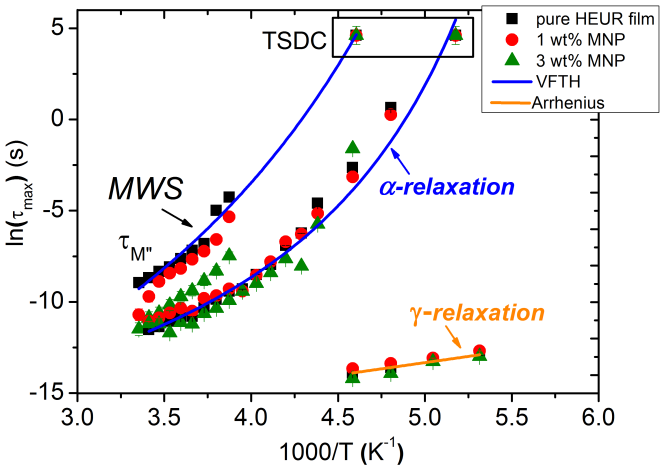

Figure 7.8.: Relaxation map showing the main processes and related fitting curves found for the 3 samples (pure HEUR polymer and nanocomposites), namely the VFTH-like polarization process (Mawell-Wagner-Sillars), the VFTH-like segmental relaxation (α) and the Arrhenius-like secondary relaxation (γ). The error bars have almost the same size of the symbols. $\tau_{M"}$ indicates that the relaxation times of the MWS polarization process are obtained from the $M"$ data (Fig. 7.9). Representative VFTH and Arrhenius fits are for the sample with 3 wt% are also shown. The dispersion peaks at -55°C observed by TSDC are plotted at the equivalent relaxation time of 100 s [158]

In order to compare the DRS results with those from TSDC and DSC, we use the so-called dielectric glass transition temperature, $T_{g,diel}$. It is calculated by extrapolation of the VFTH fits (eq. 2.66) to a standard relaxation time of 100 s. The glass transition temperatures T_g of the films are reported in the table 7.2 and it is not affected by the MNP concentration in the polymer film. Therefore, we conclude that the presence of MNPs has no remarkable effect on the time scale of the main process in the nanocomposites. The glass transition temperatures calculated with eq. 2.66 are, within the uncertainties, in agreement with the experimental values obtained by DSC. A difference in the VFTH fits is revealed by the limiting values of the relaxation time for infinite temperature, τ_0

MNP (wt %)	$E_A(\gamma)$	$T_{\alpha,TSDC}$ (°C)	$T_{g,diel}$ (°C)	D	τ_0 (ns)	T_0(°C)
0	11.3 ± 0.7	-75 ± 5	-71.1 ± 1.2	3.3 ± 0.5	71 ± 3	-98.3 ± 1.6
1	11.1 ± 0.3	-80 ± 5	-71.5 ± 5.7	2.8 ± 0.6	250 ± 30	-97.4 ± 2.9
3	16.5 ± 0.9	-80 ± 51	-67.3 ± 7.1	1.5 ± 0.8	680 ± 90	-81.4 ± 6.7

Table 7.2.: Activation energies E_A related to the γ-process, T_α from TSDC, $T_{g,diel}$ calculated from the VFTH fits, and the parameters used in the VFTH fits (according to the Angell's formalism [83]) of the α-relaxation

(table 7.2). It increases with increasing the MNP concentration. The quantity τ_0 is usually assumed to be equal to a typical phonon frequency, which is of the order of 2-10 THz [91]. Deviations from the expected range of τ_0 can be explained by a transition to a different temperature dependence at very high temperatures. Another interesting difference in the relaxation map regards the γ-relaxation detected at low temperatures [167]. Despite the limited number of experimental points related to the γ-relaxation, we fit them using the Arrhenius equation (eq. 2.65), and obtained the activation energy values $E_A(\gamma)$ reported in the table 7.2. The results suggest a slightly elevated activation energy for the nanocomposite with 3 wt% MNP concentration. We believe that this effect might be related to the changes in nano-morphology as demonstrated by the slight increase of the degree of crystallinity (table 7.1) and the changes in the degree of microphase separation. The methylene sequences, whose crankshaft motion gives rise to the γ-relaxation, are expected to face in the interfaces between different energy landscapes that inhibit slightly their mobility. The same kind of effects on the activation energy of the γ-relaxation, was observed in PU systems [168]. In general, the relaxation map shows no big difference between the dynamics of the pure HEUR film and the nanocomposites, meaning that the MNPs do not seem to influence the dynamics of the HEUR polymer. This is most probably due to the fact that the MNPs, being coated with oleic acid and oleylamine, interact mainly with the hydrophobic ends of the telechelic HEUR polymer. Therefore, they do not influence the motions associated to the main PEO (polar) chain. This result is in agreement with the structural characterization previously performed by SANS measurements (chapter 5, paragraph 5.2) in which we did not observe any influence of the MNPs on the domain spacing of the polymer matrix. Therefore, the MNPs addition neither affects the structure nor the dynamics of the polymer matrix. This means that the morphology is not modified and that the fragility of the material is not increased upon the addition of MNPs. However, as detailed below, the MNPs have an effect on the conductive behaviour of the materials.

7.4.2. High conductivity region-charge transport effects

In the following section, the details about the MWS relaxation are discussed. Increasing the temperature to the range -20 °C to 25 °C, a very high conductivity contribution is observed in the low frequency region. This region, however, cannot be fitted adequately by a simple DC-conductivity process. In addition, following the results by TSDC, one more relaxation is expected in this temperature range. For conductive systems, it is advantageous to describe the conduction mechanism using the formalism of the electrical modulus M^* (ω)= $1/\varepsilon^*$ (ω) [169,170]. In the following, by comparing different formalisms for the description of the dielectric response, we will try to extract information on the underlying mechanisms. In Fig. 7.9, the dielectric loss data of the pure HEUR film at 10 °C are shown together with the corresponding M"(ω) data. They exhibit a low-frequency peak, highlighted in Fig. 7.9 with a magenta arrow. The peak at higher frequency (indicated by the blue arrow) is attributed to the segmental relaxation associated with the glass transition of the amorphous PEO, i.e. the α-relaxation.

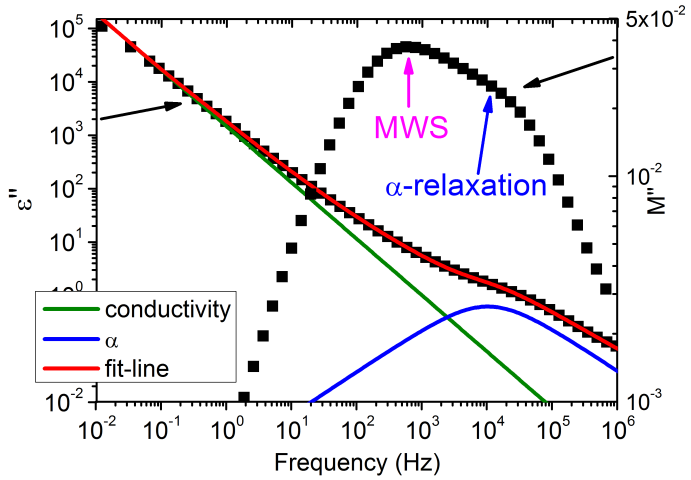

Figure 7.9.: Example of the fitting curve (at 10°C) used for the dielectric loss data of the pure HEUR film in the temperature range between -15°C and 25°C. The error bars are smaller than the symbol size. The corresponding data in the modulus representation are shown, and the assigned relaxation processes are highlighted (see text) [158]

In Fig. 7.10, the M"(ω) curves at 4 different temperatures, namely 20°C, 5°C, -10°C and -20°C, are shown. At this temperatures we observed very high conductivity in the corresponding dielectric loss data. It is known that the M"(ω) curves should exhibit low frequency peaks at frequency ω_{max}, at the crossover frequency of the corresponding conductivity data, $\sigma'(\omega)$. The crossover frequency in the conductivity data is the frequency value where the $\sigma'(\omega)$ curves start to change from the dc plateau values at lower

frequencies to the power law dependence at higher frequencies [171]. We compare the M"(ω) curves with the conductivity data $\sigma'(\omega)$ in Fig. 7.10, and the crossover frequency is highlighted in the conductivity data. The expected peak at such crossover frequencies in the electrical modulus formalism are the manifestation of the so-called conductivity relaxation [169]. However, in the case of the pure HEUR film we note that, except for the data at -20°C, the maximum frequency of the low-frequency peak in the M"(ω) is located at higher frequency than the crossover of the conductivity data (see dashed lines in Fig. 7.10).

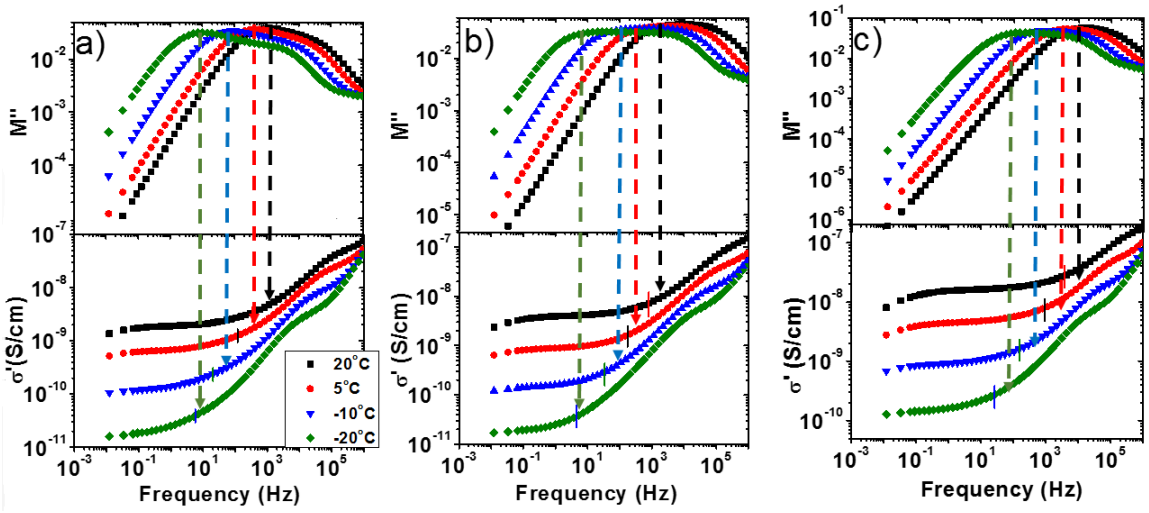

Figure 7.10.: Real part of the conductivity σ' and imaginary part of the modulus M" as a function of the frequency of a) the pure HEUR film, b) with 1 wt% MNPs and c) with 3 wt% MNPs at 4 different temperatures (20°C, 5°C, -10°C, -20°C). The error bars are smaller than the symbol size. The dashed arrows connect the maxima of the M"(ω) curves at low frequency with the crossover frequency in the conductivity data which are marked by short vertical lines [158]

For the nanocomposites, we observe the same "shift" of ω_{max} of the low frequency peak in the M"(ω) curves to a higher frequency than the crossover frequency in the $\sigma'(\omega)$ curves, also at -20°C. In this case, the peak at low frequency in the modulus formalism is not very well separated from the one related to the α-process, as it is for the pure HEUR film. This result suggests that another process occurs in the low frequency region in addition to the conductivity relaxation. This process is most probably due to an interfacial polarization mechanism, because of the low frequency region of occurrence ($10^{-1} - 10$ Hz), probably of the type of the Maxwell-Wagner-Sillars (MWS) which occurs typically in systems comprised of regions with different conductivities [165]. Additional information about the processes occurring in the low frequency region in the temperature range between -20°C and 25°C can be extracted from the first derivative of the real part of the dielectric permittivity $\varepsilon_{der}" = \delta\varepsilon'/\delta ln\omega$. The ε_{der}" data turn out to be useful for

systems which exhibit low-frequency relaxations alongside an appreciable Ohmic conductivity [172], as the $\varepsilon'(\omega)$ values are in principle not affected by the Ohmic conductivity, and according to the Kramers-Kroning relationships, its derivative is proportional to the part of ε"(ω) which arises from dipolar processes. Indeed, in the derivative formalism, the relaxation processes visible in the dielectric loss data appear as sharper peaks and without the conductivity contribution [173]. In Fig. 7.11, we compare the dielectric loss data ε" and the corresponding derivative data $\delta\varepsilon'/\delta ln\omega$ at 20°C for the pure HEUR film (the data of the nanocomposites show identical results).

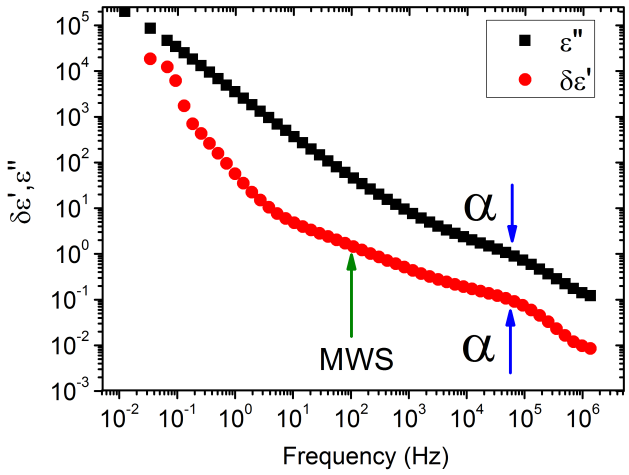

Figure 7.11.: Dielectric loss data ε" (black squares) and derivative of the real part of the permittivity $\delta\varepsilon'$ (red squares) at 20°C for the pure HEUR film. The error bars are smaller than the symbol size. The processes detected in the derivative data (the α-process and the MWS polarization process) are highlighted by the arrows [158]

From the derivative ε_{der}" $= \delta\varepsilon'/\delta ln\omega$ data, we identify three processes. The one occurring at high frequencies ($\sim 10^5$ Hz) is the α-relaxation of the polymer as observed earlier in the conventional dielectric loss data. At low frequencies, we observe two shoulders which are not visible in the ε" formalism, namely at $\sim 10^{-1}$ Hz and at $\sim$ 70 Hz, respectively (highlighted by a green arrow in Fig. 7.11). The origin of the process at $\sim 10^{-1}$ Hz is not yet completely understood. In the TSDC measurements, we observed a dispersion depending on the polarization temperature at T $\sim$ -45°C and at T $\sim$ -55°C at low frequency ($\sim 10^{-1}$ Hz), which originates from a charge polarization process. The low-frequency processes observed in the modulus and in the derivative formalisms can be associated to the dispersion found in TSDC. Thus, they could originate from a polarization mechanism, most likely of the type of MWS, since it usually reflects a microphase separation within the sample [174, 175]. According to the small angle neutron scatter-

ing data of the investigated HEUR polymer-based nanocomposites (chapter 5, paragraph 5.2), indeed, a microphase separation is observed. It originates from the phase separation between the hydrophobic domains (composed of the alkyl ends of the HEUR telechelic polymer) and the hydrophilic backbone of the polymer chain, mainly composed of PEO. The addition of MNPs up to 3 wt% leads to the formation of clusters of MNPs. On the other hand, according to the DSC and TSDC measurements, the pure HEUR film, as well as the nanocomposites, are characterized by high heterogeneity mainly caused by the PEO portion which is present in three phases:

- the amorphous PEO, giving rise to the glass transition at $\sim$ -75°C
- small crystalline PEO regions where strong confinement of the PEO chains occurs
- the main crystalline PEO phase which gives rise to the melting process at $\sim$ 50°C.

Therefore, we tend to attribute the MWS interfacial polarization process, which contributes to the detected low-frequency dispersions, to the heterogeneity of the PEO domains. The dispersion process observed in the TSDC data at -55°C, which we assigned to the MWS polarization process (Fig. 7.4), most likely corresponds to the relaxation process detected in the derivative of the real part of the permittivity ε_{der}" at $\sim 10^2$ Hz (indicated by the green arrow in Fig. 7.11). We do this assignment also taking into account the frequency where the peak at low frequency occurs in the modulus representation (Fig. 7.9, magenta arrow), which is at $\omega_{max} \sim 600$ Hz. In fact, the ω_{max} values of the relaxation processes detected in the modulus representation are shifted to higher frequencies than in the permittivity formalism [91]. In the Arrhenius plot presented in Fig. 7.8, we included the M" peak frequencies of the slower component of the composite peak which corresponds to this low frequency peak in ε_{der}". Its trace follows a VFTH temperature dependence and agrees well with the peaks observed with TSDC around -55°C. This implies that the dispersion observed in the TSDC data corresponds to the same mechanism as the one detected in the DRS data in the temperature range between -20°C and 25°C. The origin of the smaller relaxation at $\sim 10^{-1}$ Hz is yet unclear, however it may be related to slower dynamics of PEO at the interfaces between amorphous and crystalline domains (the so called α') or in amorphous areas inside the crystallites (the so-called α_c) [176, 177].

7.4.3. Comparison of the conductivity data of the pure HEUR film and the nanocomposites-polymer conductivity effect

In the high temperature region of the Arrhenius map shown in Fig.7.8, it is possible to observe a faster dynamics for the nanocomposite with 3 wt% MNPs. In fact, the relaxation times $\tau_{M"}$ associated to the interfacial polarization mechanism (MWS-relaxation) are smaller than those of the other two samples. This effect on the relaxation times $\tau_{M"}$ of the MWS relaxation can be explained by considering the proportionality between the relaxation time and the conductivity, σ', of the material. In particular, the relaxation time is known to be inversely proportional to the conductivity of the sample [91]. Indeed, looking at the conductivity data, σ', at -10°C shown in Fig. 13, we may observe that the plateau of the conductivity profile is one order of magnitude higher for the sample with the 3 wt% MNPs than for the other two samples.

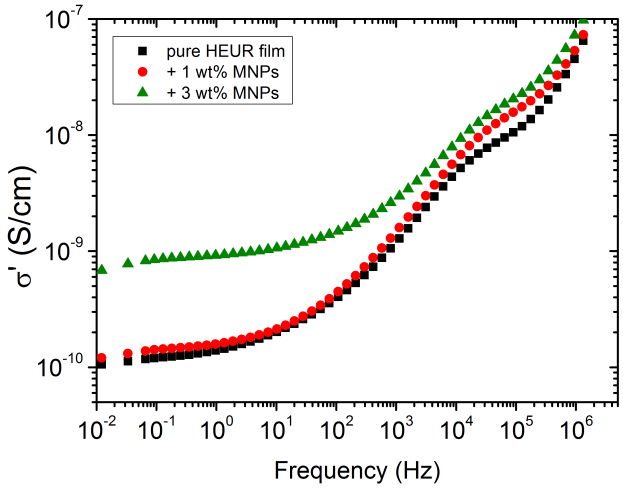

Figure 7.12.: Conductivity data σ' (S/cm) of all the investigated nanocomposites at -10°C. The error bars are smaller than the symbol size [158]

The increase of the conductivity for the nanocomposite containing 3 wt% MNPs, is reflected also in the increase of the permittivity value, ε", as seen in Fig. 7.6. In order to understand the origin of such a steep increase of the conductivity upon an increase of the MNP concentration to 3 wt%, we constructed the Arrhenius plot for the conductivity by plotting the conductivity plateau values as a function of inverse temperature (Fig. 7.13).

The Arrhenius plot gives information about the conductivity mechanism occurring in the samples. However, as shown in Fig. 7.13, for all the samples, the conductivity shows the same kind of temperature dependence, i.e. a VFTH-like, with only small differences in the curves. Therefore, the conductive mechanism occurring in the films must be the same for all the samples. The fact that, upon addition of MNPs, we observe

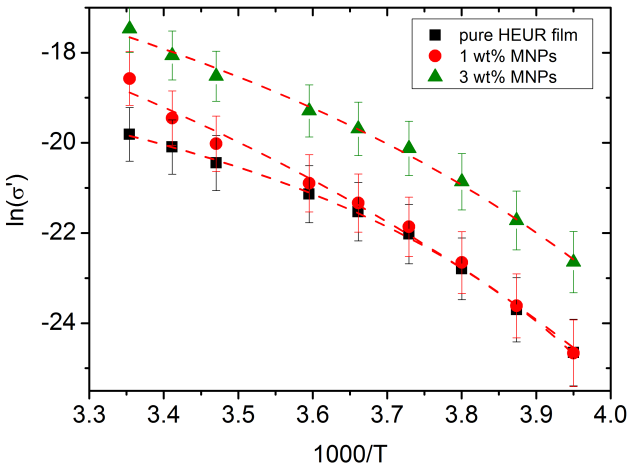

Figure 7.13.: Arrhenius map of the conductivity for all the samples. The dashed lines are guides for the eyes [158]

the same kind of conductive mechanism as in the pure HEUR film, implies that the MNPs affect only indirectly the conductive phase of the film, which is the amorphous PEO phase. In the structural characterization of the nanocomposites (chapter 5, paragraph 5.2), we observed the formation of large clusters of MNPs at an MNP concentration of 3 wt% (Fig. 7.14). However, single MNPs coexist with the MNPs clusters in the final nanocomposite formulation (Fig. 7.14 b)), indicating that the HEUR polymers partially disperse the hydrophobic MNPs. As observed in the investigation of the dynamics of HEUR hydrogel network with embedded MNPs (chapter 6, paragraph 6.2) the presence of the MNPs clusters close to the hydrophobic domains of the network leads to a "dilution" of the polymers near the hydrophobic domains, allowing a higher mobility of the polymer backbone. Indeed, in presence of the big clusters of MNPs, the hydrophobic domains become larger, leading to a considerably different grafting of the sticky hydrophobic ends of the polymer on the hydrophobic domains. This gives more space to the amorphous PEO to re-arrange. We believe that we observe the same effect in the dry films, thus, the higher degrees of freedom gained by the amorphous PEO allows an easier charge transport, leading to the observed increase of the conductivity.

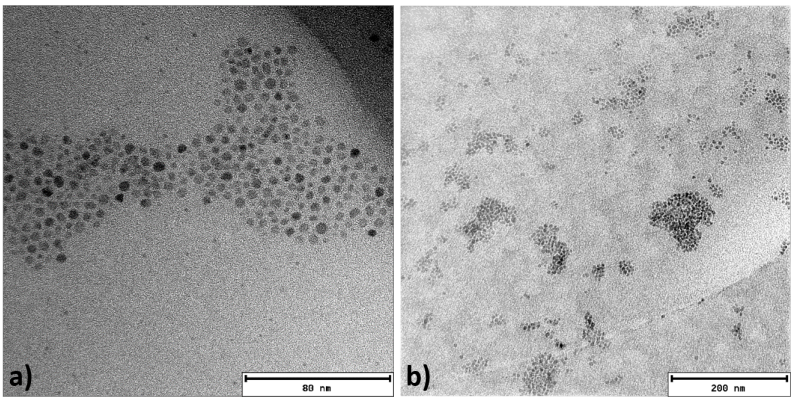

Figure 7.14.: TEM image of the HEUR dry film with a concentration of MNPs of 3 wt% showing a) large cluster of MNPs and b) large clusters of MNPs coexisting with single MNPs, indicating that the HEUR polymer matrix partially disperses the MNPs [158]

8. Conclusion and outlook

In this work I presented the structural and the dynamic characterization of a novel type of nanocomposites based on hydrophobically modified ethoxylated urethanes (HEUR) and coated magnetite nanoparticles (MNPs). The nanocomposites were studied in two different morphologies: as dry films and as hydrogels. The structural characterization of these novel materials was carried out with experimental techniques like small angle neutron scattering (SANS) and transmission electron microscopy (TEM). In the structural analysis, because of the complexity of the investigated system, at first we focused on the study of pure polymer matrix. For this purpose, rheology measurements were also performed. Together with the structural characterization, the magnetic response of the nanocomposites in the dry state was evaluated. On the other hand, the dynamic analysis was performed by employing several experimental techniques such as neutron spin echo (NSE), dielectric relaxation spectroscopy (DRS), thermally stimulated depolarization current (TSDC) and differential scanning calorimetry (DSC). The neutron spin echo spectroscopy was employed for the dynamic analysis of the systems in the hydrogel state. In the following, I summarize separately the results achieved with the structural and with the dynamic characterization respectively.

8.1. Structural characterization

The structural characterization of the pure HEUR polymer matrix was carried out analysing HEUR aqueous solutions at increasing at increasing polymer concentration ϕ_{poly} employing SANS. Because of the complexity of the system, the experimental data were fitted with two different models:

- A model developed for bicontinuous microemulsions based on the Teubner-Strey (TS) theory, and afterwards applied also on composite systems (chapter 2 paragraph 2.2.5) [65, 68, 109]. The use of this model is based on the assumption that the investigated system can be approximated to a bicontinuous microemulsion because of the presence of microscopic interfaces between different domains.

- A model originally developed for a system of polydisperse interacting colloids [58], called "poly-core shell model" . It describes our system as a collection of flower-like micelles, connected between each other by hydrophilic bridges, having spherical poly-disperse cores.

Both models described well the experimental data. In particular, with the model based on the TS theory, we followed the change of the domain spacing $d = 2\pi/q_{max}$ of the HEUR network as a function of the polymer concentration ϕ_{poly} and with the "poly core-shell model" we studied the concentration dependence of other structural parameters such as the radii of the micellar cores R_{core} of the polymer network, and the shell thickness of the hydrophilic shells t. In general, by combining the results obtained with these two different data analysis, we could follow the formation of a well percolated, inhomogeneous gel network at high polymer concentration (ϕ_{poly} >5 wt%) from an "open" or "dynamical" gel structure for low ϕ_{poly} (0.46 wt% and 0.92 wt%). In the "open" network regime, the interactions between the hydrophilic main polymer chains are negligible. We find an agreement between these results and the rheology data, obtained for HEUR aqueous solutions at increasing ϕ_{poly}. In fact, the transition between the "open" network to a "dense" one was found to be the cause of the absence of shear thickening in HEUR solutions with $\phi > 4$ wt%. Thus, the rheology results confirmed the structural results achieved by the different analysis of the SANS data of the pure HEUR aqueous solutions.
In the second step, we investigated the structure of the nanocomposite hydrogels containing coated MNPs with SANS and TEM. We prepared the hydrogels using separately two different types of coatings for the MNPs, one hydrophobic (consisting of oleic acid and oleylamine) and the second one hydrophilic (with an extra layer of C_{18}TAB) and we compared the results. The analysis of the SANS data was performed with the model based on the TS theory, because the complexity of the system did not allow a good description of the experimental data with the simpler "poly core-shell model". We found that both types of MNPs tend to form large clusters above a concentration of roughly 0.8 wt% and above this value the coexistence of large, dense MNPs clusters with isolated MNPs is observed. We believe that the hydrophobic MNPs are embedded in the hydrophobic domains of the HEUR network, while the hydrophilic MNPs stay in the aqueous phase within the polymeric network and cut or suppress some cross-links.
We prepared the nanocomposites as dry films containing only hydrophobic MNPs. In this case, from the SANS results, we did not observe a significant influence of the MNPs on the structure of the pure polymer matrix. Since we cannot assume the network-like structure in the dry state, the peak at q_{max} detected in the SANS curves in better ascribed to a microphase separation between domains with different chemical nature than to the bare distance between the hydrophobic domains of the HEUR network. On the

dry films we performed magnetic response measurements and we could observe a high magnetic response. Thus, the superparamagnetic properties of the MNPs are kept in the final formulation.

8.2. Dynamic characterization

Dynamic characterization on the nanocomposite hydrogels

The dynamics of nanocomposite hydrogels composed of HEUR polymers and MNPs was investigated by DRS and NSE. From the DRS results, we detected three relaxation processes in the temperature range between -100 °C and 25 °C:

1. The so-called α-water relaxation, associated with the glass transition of the supercooled water inside the hydrogels. This relaxation is not affected by the MNPs.

2. The segmental polymer relaxation, the α-relaxation, related to the glass transition of the polymer. In calorimetry, we observe that the T_g is decreased by $\approx$ 4°C with increasing the MNP concentration, indicating an acceleration of the segmental dynamics at long time scales ($\tau \approx 100$ s).

3. The β-relaxation, which we relate to the rotation of dipolar segments like C=O and O-H, forming H-bonds with the water. We observe a decrease of the activation energy E_A associated with this process, with increasing the MNP concentration. This result suggests that the MNP clusters lead to an increase of the sizes of the hydrophobic domains, which results in a dilution of the polymer blobs near the hydrophobic domain. As a consequence, the mobility of the smallest blobs is higher. In contrast, the smallest blobs of the pure HEUR hydrogel freeze stepwise at low temperatures and effectively shorten the mobile connecting arms. This results in a more mobile network with suppressed collective motions.

In general, due to the use of three different techniques, i.e. DSC, DRS and NSE, we can observe the different effects of the MNPs on the segmental dynamics of the polymer at different time and length scales. In particular, we observed:

- At long time scales ($\tau \approx 100$ s), probed by DSC, an acceleration of the segmental dynamics.

- At intermediate time scales ($\tau \approx 10$ ms), probed by DRS, a cross-over region is found, where the α-relaxation times of the different nanocomposites overlap.

- At short time scales ($\tau \approx 10$ ns), probed by NSE, a deceleration of the segmental dynamics appears.

We explain this difference with the change of the curvature of VFTH traces, which is related to the cooperativity of the α-relaxation. We find an increase of the cooperativity with increasing the MNP concentration. Therefore, the present systems qualify as absorbers for electromagnetic fields, since decreased energies or slowing down facilitates the energy dissipation. The addition of MNPs is a way to decrease the glass transition of the polymer, and therefore to modify the viscoelastic properties of the material.

Dynamic characterization on the nanocomposite dry films

As final step of this work, we investigated the dynamics and the thermal behaviour of the nanocomposites as dry films using three different techniques: DSC, TSDC and DRS. Therefore we could have a complete overview on the dynamics of the nanocomposites in the dried state. The thermal characterization of the systems yielded to the detection of three main phase transitions, which reveal a high heterogeneity for all the investigated samples:

1. the glass transition of the amorphous PEO portion at $\approx -75°C$
2. the crystallization/melting between $\approx -40°C$ and at $\approx 10°C$ of the PEO crystallites which experience different constraints as compared with the PEO bulk phase
3. the crystallization/melting at $\approx 50°C$ of the crystalline PEO phase.

The pure HEUR sample is found to be semi-crystalline with a degree of crystallinity of 37% with a water content of 6% (at relative humidity $rh = 80\%$). The dynamical characterization was at first carried out with TSDC measurements, which was directly related with DSC experimental findings, reveal the existence of two main dispersions. The one at $\approx -75°C$, which does not depend on the polarization temperature, T_p, is attributed to the segmental relaxation of the amorphous portion of PEO (α-relaxation). The second dispersion observed at higher temperature, namely at $\approx -75°C$, has been found to depend on T_p, meaning that a dipolar-like mechanism, like the Mawell-Wagner-Sillar (MWS) polarization process may be involved. The MWS process is usually observed when the sample is microphase-separated. Since in the structural characterization we detected a microphase separation between different parts of the polymer chains, this was expected. The TSDC results were compared with the ones obtained with DRS. From the dielectric measurements, three relaxation processes were detected:

1. at -20 °C < T < 25 °C a low-frequency process, which we suggest to be related to the MWS polarization
2. at -65 °C < T < 25 °C the α-process associated to the dynamic glass transition of the amorphous PEO

3. at T < -55 °C, the γ-relaxation attributed to the crankshaft motion of the methylene groups.

Nearly no influence of the addition of MNPs on the α-relaxation of the HEUR polymer was observed. This means that the structural properties of the material, such as the glass transition T_g and its fragility, are not affected by the presence of the MNPs. This result is in agreement with the structural characterization of the nanocomposites, which revealed no change in the domain spacing of the polymer network with increasing concentration of MNPs. We believe that the MNPs do not influence the α-relaxation of the HEUR polymer because, being coated with an hydrophobic shell, they interact mainly with the its hydrophobic ends and not with the amorphous PEO portion. Therefore, the change of polarity of the MNPs coating could lead to stronger interactions with the PEO chains, resulting in a modification of the dynamics of the nanocomposites compared to the pure HEUR film. On the other hand, the addition of MNPs influences the γ-relaxation at low temperatures. In particular, we observe an increase of its activation energy $E_A(\gamma)$ for the nanocomposite with 3 wt % MNP concentration. We ascribe this effect to the slight increase of the crystallinity degree of the PEO portion upon increasing the MNP concentration. We believe that the increase of the crystallites size inhibits the crankshaft motion of the methylene sequences of the polymer backbone. Finally, we observe a steep increase of the DC-conductivity in the temperature range -20 °C < T < 25 °C upon increasing the MNP concentration. We ascribe this increase to the formation of large clusters of MNPs which leads to a lower "grafting density" of the hydrophobic ends of the HEUR polymer than in the case of the pure film (characterized by smaller hydrophobic domains). The lower polymer concentration near the clusters allows the polymer to re-arrange more easily, thus, promoting the charge transport. This effect leads to an increase of the conductivity of the system. Despite the not perfect MNPs dispersion into the polymer matrix, we manage to achieve two main results upon the addition of MNPs: the increase of the conductivity and the keeping of the glass transition temperature.

8.3. Results in brief

We can summarize in the following points the main results achieved in this work on the preparation and characterization of the novel magnetic nanocomposites:

1. Identification of the best mixture composition.
2. Connection between the conductivity and the dynamics.
3. Achievement of a first picture of the response to external stimuli; how does the material behave in external fields.

8.4. Future plans

In this work, we focused particular attention on the understanding of the structure and the dynamics of the HEUR polymer matrix and on their dependence on the MNPs concentration. Another interesting point of view for future investigations would be to focus on the magnetic properties of the MNPs, for instance, by performing magnetic relaxation measurements. In fact, they would give information about the relaxation of the dispersed nanoparticles and allow to distinguish between physically trapped and mobile nanoparticles [178]. Furthermore, NSE measurements carried out in paramagnetic mode would be of some interest in order to have additional insights into the dynamics of the MNPs. However, both types of measurements are beyond the scope of the present study. On the other hand, future improvements regarding the preparation of the novel nanocomposites, would be a shift from hexane to DMF or DMAC as solvent. This would improve the final dispersion quality since both, the polymer and the MNPs, are soluble in those solvents.

A. Appendix

A.1. Supporting information to the chapter 5

A.1.1. HEUR CMC determination through fluorescence measurements

In order to obtain the critical micelle concentration (CMC) of the HEUR polymer under investigation, a simple fluorimetric method was used. The anionic dye 8-anilino-1-naphtalenesulfonic acid magnesium salt (ANS) (0.50 g) was added to 3 mL of H_2O. The fluorescence measurements were carried out using the Spectrofluorometer Jasco FP-750, at room temperature (300 K), using an excitation wavelength λ of 375 nm. The dye ANS is not easily soluble in water, therefore the fluorescence intensity recorded at 480 nm was very low. The TAFIGEL® PUR 61 was gradually added to the ANS-H_2O mixture. The plot of the fluorescence intensity recorded at 480 nm versus the HEUR polymer concentration ($\phi_{polymer}$) is shown in Fig. A.1.

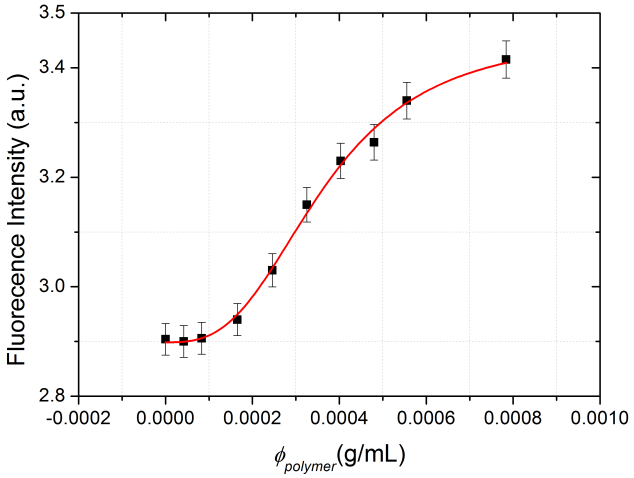

Figure A.1.: Fluorescence intensity at 480 nm of the dye ANS as function of the HEUR polymer concentration ($\phi_{polymer}$). The red line is a guide for eyes

The fluorescence intensity increases increasing the polymer concentration. This effect is

due to the solubility of the dye ANS within the hydrophobic core of the micelle composed of the HEUR polymer molecules. We could extract the CMC value from the inflection point of the fitting function of the experimental data (red line in Fig. A.1). The calculated CMC value is: $(2.89 \pm 0.13) \times 10^{-4}$ g/mL.

A.2. Supporting information to the chapter 6

A.2.1. Differential scanning calorimetry measurements of the nanocomposites as hydrogels

The DSC heating curves of the HEUR hydrogels with 0.46 wt% MNP and 0.8 wt% MNP are shown in Fig. A.2. Three main phase transitions are observed: the glass transition (T_g) of the PEO portion of the HEUR polymer at $\sim$ -80°C, the cold crystallization of water at -48°C and the melting of deuterated water at -4°C.

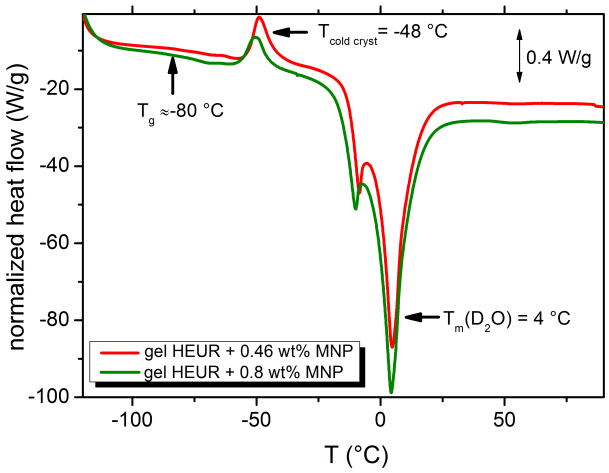

Figure A.2.: DSC heating curves of the nanocomposite hydrogels. The glass transition T_g, the cold crystallization temperature of D_2O, and the melting point of D_2O are highlighted by arrows

Besides the slight decrease of the glass transition of few degrees for the nanocomposite with 0.8 wt% MNPs (T_g = -83 °C), there are no significant differences between the DSC curves of the pure HEUR gel and of the nanocomposites.

A.2.2. Neutron spin echo measurements on the nanocomposites as hydrogels

The intermediate scattering functions of the nanocomposite hydrogels with 0.46 wt% and 0.8 wt% MNPs are shown in Fig. A.3 a) and b). The time decays of the scattering function for the nanocomposites present the same features as the one of the pure HEUR gel 25 wt% (aq) Fig. 6.9.

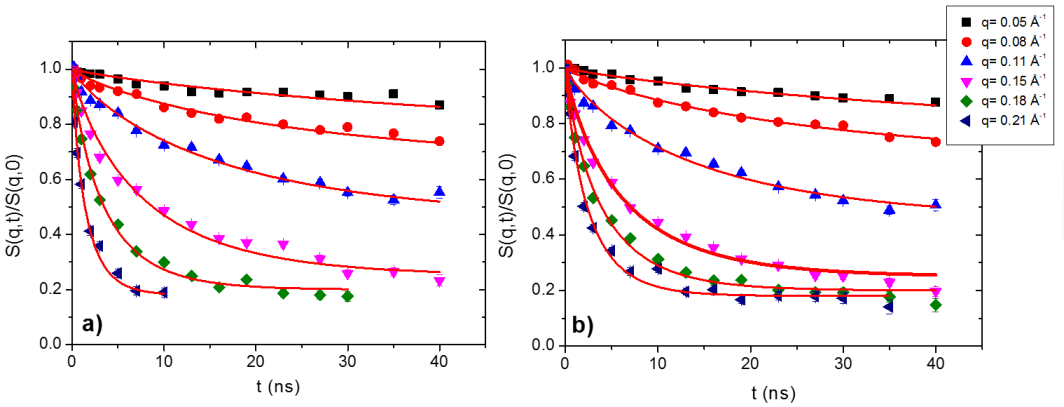

Figure A.3.: Intermediate scattering functions of the nanocomposite hydrogels containing a) 0.46 wt% MNP and b) 0.8 wt% MNP. The red lines are fits with equation 6.5

The data were fitted with equation 6.5 explained in the chapter 6, paragraph 6.3.

A.3. Supporting information to the chapter 7

A.3.1. Differential scanning calorimetry (DSC) on the nanocomposites as dry films

The phase transitions of the nanocomposites under investigation were followed by Differential Scanning Calorimetry. The heating DSC curves from -150 °C up to 150 °C with 10 °C/min, of the nanocomposites are shown in Fig. A.4. The phase transitions observed are the same as those observed in the DSC heating curve of the pure HEUR film (Fig. 7.3), i.e. the glass transition T_g at $\sim$ -80 °C, the melting peak of the small PEO crystallities at $\sim$-22 °C and the melting peak of the crystalline PEO portion at 49 °C. As for the pure HEUR film, the degree of crystallinity, X_c, of the nanocomposites was calculated according to the equation 7.2.

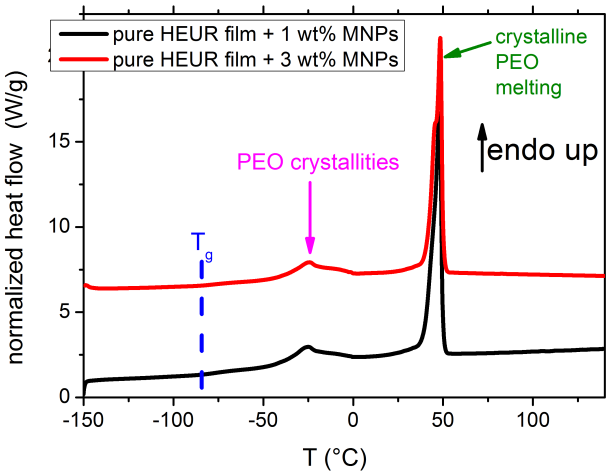

Figure A.4.: DSC heating curves of the nanocomposites from -150°C to 90°C with 10 °C/min. The glass transition temperatures T_g are highlighted by the dashed blue line. The magenta arrow indicates the melting peak at $\sim$ -22°C and the green one indicated the melting peak of the PEO crystalline portion. For clarity, the curves are shifted vertically

A.3.2. Dielectric relaxation spectroscopy (DRS) measurements on the nanocomposites as dry films

The dielectric loss data of the nanocomposites at all the measured temperatures are shown in Fig. A.5 and A.6. The main features, i.e. the high conductivity contribution at low frequencies, the shoulder related to the α-relaxation and the one related to the γ-relaxation, the of the dielectric loss profile of the pure HEUR film shown in Fig. 7.5 in the main text are conserved. Furthermore, we observe the increase of the conductivity value in the low-frequency region of one order of magnitude for the nanocomposite with 3 wt% MNP compared to the pure HEUR film (Fig. 7.5).

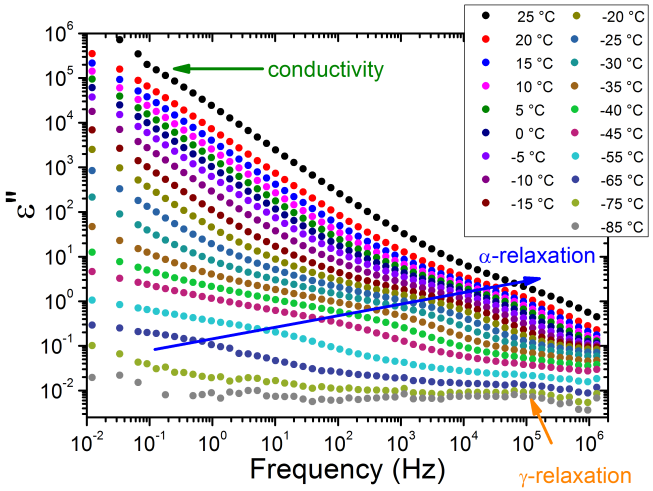

Figure A.5.: Dielectric loss data of the HEUR film with 1 wt% MNP concentration

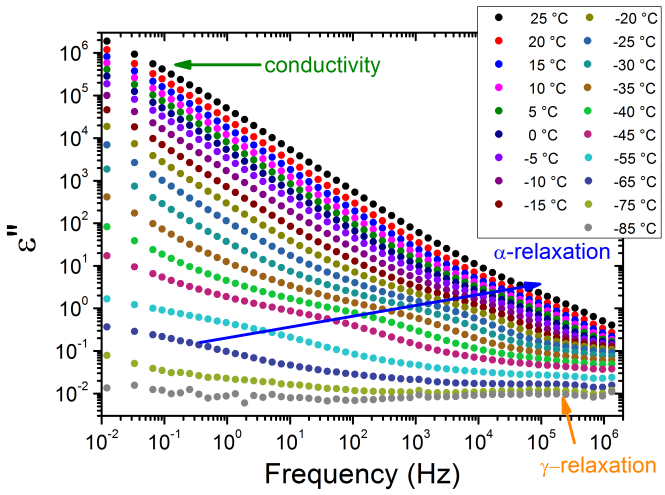

Figure A.6.: Dielectric loss data of the HEUR film with 3 wt% MNP concentration

Bibliography

[1] S. Kalia, S. Kango, A. Kumar, Y. Haldorai, B. Kumari, and R. Kumar, "Magnetic polymer nanocomposites for environmental and biomedical applications," *Colloid and Polymer Science*, vol. 292, no. 9, pp. 2025–2052, 2014.

[2] Q. Wei, Y. Lin, E. R. Anderson, A. L. Briseno, S. P. Gido, and J. J. Watkins, "Additive-driven assembly of block copolymer-nanoparticle hybrid materials for solution processable floating gate memory," *ACS Nano*, vol. 6, no. 2, pp. 1188–1194, 2012.

[3] M. Kus, F. Ozel, N. M. Varal, and M. Ersoz, "Luminescence enhancement of oled performance by doping colloidal magnetic fe_3o_4 nanoparticles," *Progress In Electromagnetics Research*, vol. 134, pp. 509–524, 2013.

[4] D. M. González, V. Körstgens, Y. Yao, L. Song, G. Santoro, S. V. Roth, and P. Müller-Buschbaum, "Improved power conversion efficiency of p3ht:pcbm organic solar cells by strong spin-orbit coupling-induced delayed fluorescence," *Advanced Energy Materials*, vol. 5, no. 8, pp. n/a–n/a, 2015.

[5] V. B. Bregar, "Advantages of ferromagnetic nanoparticle composites in microwave absorbers," *IEEE Transactions on Magnetics*, vol. 40, no. 3, pp. 1679–1684, 2004.

[6] Z. Guo, S. Park, H. T. Hahn, S. Wei, M. Moldovan, A. B. Karki, and D. P. Young, "Magnetic and electromagnetic evaluation of the magnetic nanoparticle filled polyurethane nanocomposites," *Journal of Applied Physics*, vol. 101, no. 9, pp. 1–3, 2007.

[7] V. Lauter-Pasyuk, H. J. Lauter, G. P. Gordeev, P. Müller-Buschbaum, B. P. Toperverg, M. Jernenkov, and W. Petry, "Nanoparticles in block-copolymer films studied by specular and off-specular neutron scattering," *Langmuir*, vol. 19, no. 19, pp. 7783–7788, 2003.

[8] M. M. A. Kashem, J. Perlich, A. Diethert, W. Wang, M. Memesa, J. S. Gutmann, E. Majkova, I. Capek, S. V. Roth, W. Petry, and P. Müller-Buschbaum, "Array of magnetic nanoparticles via particle co-operated self-assembly in block copolymer thin film," *Macromolecules*, vol. 42, no. 16, pp. 6202–6208, 2009.

[9] K. Aissou, T. Alnasser, G. Pecastaings, G. Goglio, O. Toulemonde, S. Mornet, G. Fleury, and G. Hadziioannou, "Hierarchical assembly of magnetic l10-ordered fept nanoparticles in block copolymer thin films," *J. Mater. Chem. C*, vol. 1, pp. 1317–1321, 2013.

[10] A. N. Semenov, J. Joanny, and A. R. Khokhlov, "Associating polymers: Equilibrium and linear viscoelasticity," *Macromolecules*, vol. 28, no. 4, pp. 1066–1075, 1995.

[11] G. Marrucci, S. Bhargava, and S. L. Cooper, "Models of shear-thickening behavior in physically crosslinked networks," *Macromolecules*, vol. 26, no. 24, pp. 6483–6488, 1993.

[12] S. Suzuki, T. Uneyama, and H. Watanabe, "Concentration dependence of nonlinear rheological properties of hydrophobically modified ethoxylated urethane aqueous solutions," *Macromolecules*, vol. 46, no. 9, pp. 3497–3504, 2013.

[13] K. C. Tam, R. D. Jenkins, M. A. Winnik, and D. R. Bassett, "A structural model of hydrophobically modified urethane-ethoxylate (heur) associative polymers in shear flows," *Macromolecules*, vol. 31, no. 13, pp. 4149–4159, 1998.

[14] T. Annable, R. Buscall, R. Ettelaie, and D. Whittlestone, "The rheology of solutions of associating polymers: Comparison of experimental behavior with transient network theory," *Journal of Rheology*, vol. 37, no. 4, pp. 695–726, 1993.

[15] D. Calvet, A. Collet, M. Viguier, J.-F. Berret, and Y. Séréro, "Perfluoroalkyl end-capped poly(ethylene oxide). synthesis, characterization, and rheological behavior in aqueous solution," *Macromolecules*, vol. 36, no. 2, pp. 449–457, 2003.

[16] H.-W. Engels, H.-G. Pirkl, R. Albers, R. W. Albach, J. Krause, A. Hoffmann, H. Casselmann, and J. Dormish, "Polyurethanes: Versatile materials and sustainable problem solvers for today's challenges," *Angewandte Chemie International Edition*, vol. 52, no. 36, pp. 9422–9441, 2013.

[17] W.-T. Liu, "Nanoparticles and their biological and environmental applications," *Journal of Bioscience and Bioengineering*, vol. 102, no. 1, pp. 1–7, 2006.

[18] S. Guo, D. Li, L. Zhang, J. Li, and E. Wang, "Monodisperse mesoporous superparamagnetic single-crystal magnetite nanoparticles for drug delivery," *Biomaterials*, vol. 30, no. 10, pp. 1881–1889, 2009.

[19] J. Kim, H. S. Kim, N. Lee, T. Kim, H. Kim, T. Yu, I. C. Song, W. K. Moon, and T. Hyeon, "Multifunctional uniform nanoparticles composed of a magnetite nanocrystal core and a mesoporous silica shell for magnetic resonance and fluorescence imaging and for drug delivery," *Angewandte Chemie International Edition*, vol. 47, no. 44, pp. 8438–8441, 2008.

[20] C. A. Uraneck, H. L. Hsieh, and O. G. Buck, "Telechelic polymers," *Journal of Polymer Science*, vol. 46, no. 148, pp. 535–539, 1960.

[21] F. L. Verso and C. N. Likos, "End-functionalized polymers: Versatile building blocks for soft materials," *Polymer*, vol. 49, no. 6, pp. 1425–1434, 2008.

[22] G. T. Gotzamanis, C. Tsitsilianis, S. C. Hadjiyannakou, C. S. Patrickios, R. Lupitskyy, and S. Minko, "Cationic telechelic polyelectrolytes synthesis by group transfer polymerization and self-organization in aqueous media," *Macromolecules*, vol. 39, no. 2, pp. 678–683, 2006.

[23] R. R. Taribagil, M. A. Hillmyer, and T. P. Lodge, "Hydrogels from aba and abc triblock polymers," *Macromolecules*, vol. 43, no. 12, pp. 5396–5404, 2010.

[24] A. N. Semenov, I. A. Nyrkova, and M. E. Cates, "Phase equilibria in solutions of associating telechelic polymers: rings vs reversible network," *Macromolecules*, vol. 28, no. 23, pp. 7879–7885, 1995.

[25] M. Daoud and J. Cotton, "Star shaped polymers : a model for the conformation and its concentration dependence," *J. Phys. France*, vol. 43, no. 3, pp. 531–538, 1982.

[26] T. A. Witten and P. A. Pincus, "Colloid stabilization by long grafted polymers," *Macromolecules*, vol. 19, no. 10, pp. 2509–2513, 1986.

[27] G. Broze, R. Jerome, P. Teyssie, and C. Marco, "Halato-telechelic polymers. 6. viscoelastic properties of solutions of alkaline earth α,ι-dicarboxylato polybutadiene," *Macromolecules*, vol. 16, no. 6, pp. 996–1000, 1983.

[28] J. P. Gouin, C. E. Williams, and A. Eisenberg, "Microphase structure of block ionomers. 1. study of molded styrene-4-vinylpyridinium aba blocks by saxs and sans," *Macromolecules*, vol. 22, no. 12, pp. 4573–4578, 1989.

[29] T. A. Witten, "Heterogeneous polymers and self-organization," *Journal of Physics: Condensed Matter*, vol. 2, no. S, p. SA1, 1990.

[30] M. A. Winnik and A. Yektaf, "Associative polymers in aqueous solution," *Current Opinion in Colloid and Interface Science*, vol. 2, pp. 424–436, 1997.

[31] L. M. Landoll, "Nonionic polymer surfactants," *Journal of Polymer Science: Polymer Chemistry Edition*, vol. 20, no. 2, pp. 443–455, 1982.

[32] L. M. Landoll *U.S. Patent 4228277, United States*, 1979.

[33] U. P. Strauss, *Hydrophobic Polyelectrolytes*, ch. 17, pp. 317–324. American Chemical Society, 1979.

[34] J. Glass, "A perspective on the history of and current research in surfactant-modified, water-soluble polymers," *Journal of Coatings Technology*, vol. 73, no. 913, pp. 79–98, 2001.

[35] K. C. Tam, R. D. Jenkins, M. A. Winnik, and D. R. Bassett, "A structural model of hydrophobically modified urethane-ethoxylate (heur) associative polymers in shear flows," *Macromolecules*, vol. 31, no. 13, pp. 4149–4159, 1998.

[36] R. May, J. P. Kaczmarski, and J. E. Glass, "Influence of molecular weight distributions on heur aqueous solution rheology," *Macromolecules*, vol. 29, no. 13, pp. 4745–4753, 1996.

[37] S. X. Ma and S. L. Cooper, "Shear thickening in aqueous solutions of hydrocarbon end-capped poly(ethylene oxide)," *Macromolecules*, vol. 34, no. 10, pp. 3294–3301, 2001.

[38] P. DeGennes, *Scaling concepts in polymers physics*. Cornell University Press, Ithaca, 1979.

[39] P. Flory, *Statistical Mechanics of Chain Molecules*. Wiley, New York, 1969.

[40] M. Rubinstein and R. Colby, *Polymers physics*, vol. 767. Oxford Oxford, UK, 2003.

[41] B. H. Zimm and W. H. Stockmayer, "The dimensions of chain molecules containing branches and rings," *The Journal of Chemical Physics*, vol. 17, no. 12, pp. 1301–1314, 1949.

[42] D. S. Gaunt, J. E. G. Lipson, J. L. Martin, M. F. Sykes, G. M. Torrie, S. G. Whittington, and M. K. Wilkinson, "Lattice trees with specified topologies," *Journal of Physics A: Mathematical and General*, vol. 17, no. 1, p. 211, 1984.

[43] K. Kajiwara and C. A. M. Ribeiro, "Dilute solution properties of randomly branched polymer systems. i. the particle scattering factor," *Macromolecules*, vol. 7, no. 1, pp. 121–128, 1974.

[44] A. Halperin and S. Alexander, "Confined star polymers," *Macromolecules*, vol. 20, no. 5, pp. 1146–1152, 1987.

[45] A. Halperin, "Polymeric micelles: a star model," *Macromolecules*, vol. 20, no. 11, pp. 2943–2946, 1987.

[46] G. B. K. S.P. Gubin, Yu A. Koksharov and G. Y. Yurkov, "Magnetic nanoparticles: preparation, structure and properties," *Russian Chemical Reviews*, vol. 74, no. 6, pp. 489–520, 2005.

[47] G. K. Louis X. Tiefenauer and R. Y. Andres, "Antibody-magnetite nanoparticles: In vitro characterization of a potential tumor-specific contrast agent for magnetic resonance imaging," *Bioconjugate Chemistry*, vol. 4, no. 5, pp. 347–352, 1993. PMID: 8274518.

[48] S. Sun, , and H. Zeng, "Size-controlled synthesis of magnetite nanoparticles," *Journal of the American Chemical Society*, vol. 124, no. 28, pp. 8204–8205, 2002. PMID: 12105897.

[49] G. C. Papaefthymiou, "Nanoparticle magnetism," *Nano Today*, vol. 4, no. 5, pp. 438 – 447, 2009.

[50] "Nanoparticle magnetism," *Nano Today*, vol. 4, no. 5, pp. 438–447, 2009.

[51] E. C. Stoner and E. P. Wohlfarth, "A mechanism of magnetic hysteresis in heterogeneous alloys," *Philosophical Transactions of the Royal Society of London A: Mathematical, Physical and Engineering Sciences*, vol. 240, no. 826, pp. 599–642, 1948.

[52] J. Park, E. Lee, N.-M. Hwang, M. Kang, S. C. Kim, Y. Hwang, J.-G. Park, H.-J. Noh, J.-Y. Kim, J.-H. Park, and T. Hyeon, "One-nanometer-scale size-controlled synthesis of monodisperse magnetic iron oxide nanoparticles," *Angewandte Chemie International Edition*, vol. 44, no. 19, pp. 2872–2877, 2005.

[53] Q. A. Pankhurst, J. Connolly, S. K. Jones, and J. Dobson, "Applications of magnetic nanoparticles in biomedicine," *Journal of Physics D: Applied Physics*, vol. 36, no. 13, p. R167, 2003.

[54] A. J. Jackson, *Introduction to Small-Angle Neutron Scattering and Neutron Reflectometry*, pp. 1–24. NIST Center for Neutron Research, 2008.

[55] E.Fermi, *Nuclear Physics*. Chicago: 1st edition, Chicago univ. Press, 1950.

[56] G. Squires, *Introduction to thermal neutron scattering*. NY: Dover Publication, 1978.

[57] M. Meyer, *The Microscopic Structure of Polymer Grafted Nanoparticles*. Dr. (fh), WW. Münster, 2012. Record converted from VDB: 16.11.2012; Münster, WWU, Diss., 2012.

[58] M. Kotlarchyk and S. Chen, "Analysis of small angle neutron scattering spectra from polydisperse interacting colloids," *The Journal of Chemical Physics*, vol. 79, no. 5, pp. 2461–2469, 1983.

[59] S. K. Agrawal, N. S. DeLong, G. N. Tew, and S. R. Bhatia, "Structural characterization of solutions PLA –PEO-PLA and hydrogels: Crystalline vs amorphous PLA domains," *Macromolecules*, vol. 41, no. 5, pp. 1774–1784, 2008.

[60] L. D. Landau and E. M. Lifschitz, *Statistische PhysiK*. Berlin: Akademie, 1979.

[61] G. H. Lander, R. A. Robinson, and M. Kotlarchyk, "Neutron scattering structure of concentrated microemulsions studied by small-angle neutron scattering," *Physica B+C*, vol. 136, no. 1, pp. 274 – 280, 1986.

[62] L. Auvray, J. P. Cotton, R. Ober, and C. Taupin, "Structure of concentrated winsor microemulsions by sans," *Physica B+C*, vol. 136, no. 1–3, pp. 281 – 283, 1986. Neutron ScatteringProceedings of the International Conference on Neutron Scattering.

[63] E.Caponetti, L. J.Magid, J. B.Hayter, and J. S.Johnson, "Small-angle neutron scattering from water-in-oil microemulsions," *Langmuir*, vol. 2, no. 6, pp. 722–731, 1986.

[64] A. de Geyer and J. Tabony, "Evidence for intercontiguous structures in concentrated microemulsions. neutron small-angle scattering results," *Chemical Physics Letters*, vol. 113, no. 1, pp. 83 – 88, 1985.

[65] M. Teubner and R. Strey, "Origin of the scattering peak in microemulsions," *The Journal of Chemical Physics*, vol. 87, no. 5, pp. 3195–3200, 1987.

[66] L. S. Ornstein and F. Zernike, "Accidental deviations of density and opalescence at the critical point of a single substance," *Proc. Acad. Sci.*, vol. 17, p. 793–806, 1914.

[67] P. Debye and A. M. Bueche, "Scattering by an inhomogeneous solid," *Journal of Applied Physics*, vol. 20, no. 6, pp. 518–525, 1949.

[68] C. Frank, H. Frielinghaus, J. Allgaier, and H. Prast, "Nonionic surfactants with linear and lranched hydrocarbon tails compositional analysis, phase behavior, and film properties in bicontinuous microemulsions," *Langmuir*, vol. 23, no. 12, pp. 6526–6535, 2007.

[69] G. Beaucage, "Small-Angle Scattering from Polymeric Mass Fractals of Arbitrary Mass-Fractal Dimension," *Journal of Applied Crystallography*, vol. 29, pp. 134–146, Apr 1996.

[70] T. Tanaka, "Collapse of gels and the critical endpoint," *Phys. Rev. Lett.*, vol. 40, pp. 820–823, Mar 1978.

[71] T. Tanaka, D. Fillmore, S.-T. Sun, I. Nishio, G. Swislow, and A. Shah, "Phase transitions in ionic gels," *Phys. Rev. Lett.*, vol. 45, pp. 1636–1639, Nov 1980.

[72] Y. Hirokawa and T. Tanaka, "Volume phase transition in a nonionic gel," *The Journal of Chemical Physics*, vol. 81, no. 12, pp. 6379–6380, 1984.

[73] M. Shibayama and T. Tanaka, *Responsive Gels: Volume Transitions I*, ch. Volume phase transition and related phenomena of polymer gels, pp. 1–62. Berlin, Heidelberg: Springer Berlin Heidelberg, 1993.

[74] S. Panyukov and Y. Rabin, "Polymer gels: frozen inhomogeneities and density fluctuations," *Macromolecules*, vol. 29, no. 24, pp. 7960–7975, 1996.

[75] M. Sugiyama, M. Annaka, K. Hara, M. E. Vigild, and G. D. Wignall, "Small-angle scattering study of mesoscopic structures in charged gel and their evolution on dehydration," *The Journal of Physical Chemistry B*, vol. 107, no. 26, pp. 6300–6308, 2003.

[76] D. Richter, M. Monkenbush, A.Arbe, and J. Colemenero, *Neutron Spin Echo in Polymer Systems*, pp. 1–221. Springer Berlin Heidelberg, 2005.

[77] K. L. Ngai, *Relaxation and Diffusion in Complex Systems*, vol. 1. Springer-Verlag New York, 2011.

[78] S. Arrhenius, "On the reaction velocity of the inversion of cane sugar by acids," *Zeitschrift für physikalische Chemie*, vol. 4, p. 226, 1889.

[79] M. D. Ediger, C. A. Angell, and S. R. Nagel, "Supercooled liquids and glasses," *J. Phys. Chem.*, vol. 100, pp. 13200–13212, 1996.

[80] C. A. Angell, K. L. Ngai, G. B. M. P. F. McMillan, and S. W. Martin, "Relaxation in glassforming liquids and amorphous solids," *J. Appl. Phys.*, vol. 88, pp. 3113–3157, 2000.

[81] K. Ngai, "Dynamic and thermodynamic properties of glass-forming substances," *Journal of Non-Crystalline Solids*, vol. 275, no. 1–2, pp. 7–51, 2000.

[82] G. Tammann and W. Hesse, "Die abhängigkeit der viscosität von der temperatur bie unterkühlten flüssigkeiten," *Zeitschrift für anorganische und allgemeine Chemie*, vol. 156, no. 1, pp. 245–257, 1926.

[83] C. A. Angell and R. D. Bressel, "Fluidity and conductance in aqueous electrolyte solutions. approach from the glassy state and high-concentration limit. i. calcium nitrate solutions," *The Journal of Physical Chemistry*, vol. 76, no. 22, pp. 3244–3253, 1972.

[84] R. Böhmer, K. L. Ngai, C. A. Angell, and D. J. Plazek, "Nonexponential relaxations in strong and fragile glass formers," *The Journal of Chemical Physics*, vol. 99, no. 5, pp. 4201–4209, 1993.

[85] P. E. Rouse, "A theory of the linear viscoelastic properties of dilute solutions of coiling polymers," *The Journal of Chemical Physics*, vol. 21, no. 7, pp. 1272–1280, 1953.

[86] P. G. De Gennes, "Dynamics of entangled polymer solutions. i. the rouse model," *Macromolecules*, vol. 9, no. 4, pp. 587–593, 1976.

[87] M. Rubinstein and R. Colby, *Polymers physics*, vol. 767. Oxford Oxford, UK, 2003.

[88] B. H. Zimm *The Journal of Chemical Physics*, vol. 24, p. 269, 1956.

[89] A. V. Feoktystov, H. Frielinghaus, Z. Di, S. Jaksch, V. Pipich, M.-S. Appavou, E. Babcock, R. Hanslik, R. Engels, G. Kemmerling, H. Kleines, A. Ioffe, D. Richter, and T. Brückel, "Kws-1 high-resolution small-angle neutron scattering instrument at jcns: current state," *Journal of Applied Crystallography*, vol. 48, no. 1, pp. 61–70, 2015.

[90] D. Williams and C. B. Carter, *Transmission electron microscopy*. 233 Spring Street, NY: Springer Science+Busness Media, 2009.

[91] F. Kremer, "Dielectric spectroscopy – yesterday, today and tomorrow," *Journal of Non-Crystalline Solids*, vol. 305, no. 1–3, pp. 1–9, 2002.

[92] F. Kremer and A. Schönhals, *Broadband Dielectric Spectroscopy*. Berlin Heidelberg: Springer-Verlag Berlin Heidelberg, 2003.

[93] P. Debye, *Polare molekeln*. Leipzig: S. Hirzel, 1929.

[94] F. Mezei, *The principles of neutron spin echo*, ch. 1, pp. 1–26. Springer Berlin Heidelberg, 1980.

[95] B.Farago, *Time-of-Flight Neutron Spin Echo: Present Status*, ch. 17, pp. 15–34. Springer Verlag Berlin, 2003.

[96] O. Holderer, M. Monkenbusch, R. Schätzler, H. Kleines, W. Westerhausen, and D. Richter, "The jcns neutron spin-echo spectrometer J-NSE at the FRM II," *Measurement Science and Technology*, vol. 19, no. 3, p. 034022, 2008.

[97] I. K, I. Fujite, K. Wada, and J. Nakamura, "Effect of dielectric insert on surface charge density of electrets," *Journal of Electrochem. Soc.*, vol. 121, no. 4, pp. 591–593, 1974.

[98] M. M. Perlman, "Thermally stimulated currents and voltages and dielectric properties," *Journal of The Electrochemical Society*, vol. 119, no. 7, pp. 892–898, 1972.

[99] R. G. Larson, *The structure and rheology of complex fluids*, vol. 33. New York: Oxford university press, 1999.

[100] H. A. Barnes, J. F. Hutton, and K. Walters, *An introduction to rheology*, vol. 3. Elsevier, 1999.

[101] A. Sojoudi and S. C. Saha, "Shear thinning and shear thickening non- newtonian confined fluid flow over rotating cylinder," *American Journal of Fluid Dynamics*, vol. 2, no. 6, pp. 117–121, 2012.

[102] A. Campanella, Z. Di, A. Luchini, L. Paduano, A. Klapper, M. Herlitschke, O. Petracic, M. Appavou, P. Müller-Buschbaum, H. Frielinghaus, and D. Richter, "Nanocomposites composed of HEUR polymer and magnetite iron oxide nanoparticles: Structure and magnetic response of the hydrogel and dried state," *Polymer*, vol. 60, pp. 176–185, 2015.

[103] S. Sun, H. Zeng, D. B. Robinson, S. Raoux, P. M. Rice, S. X. Wang, and G. Li, "Monodisperse MFe_2O_4 (M = Fe, Co, Mn) nanoparticles," *Journal of the American Chemical Society*, vol. 126, no. 1, pp. 273–279, 2004.

[104] G. U. Baek, B. S. Kim, E. R. Kim, and D. W. Son, "Aggregation prodesses of hydrophobically modified polythylene oxide," *Bulletin of the Korean Chemical Society*, vol. 21, no. 6, pp. 623–627, 2000.

[105] E. D. Vendittis, G. Palumbo, G. Parlato, and V. Bocchini, "A fluorimetric method for the estimation of the critical micelle concentration of surfactants," *Analytical Biochemistry*, vol. 115, no. 2, pp. 278–286, 1981.

[106] C. L. Zhao, M. A. Winnik, G. Riess, and M. D. Croucher, "Fluorescence probe techniques used to study micelle formation in water-soluble block copolymers," *Langmuir*, vol. 6, no. 2, pp. 514–516, 1990.

[107] J. Sprakel, N. A. M. Besseling, and F. A. M. L. M. A. Cohen Stuart, "Phase behavior of flowerlike micelles in a scf cell model," *The European Physical Journal E*, vol. 25, no. 2, pp. 163–173, 2008.

[108] F. Tanaka, "Intramolecular micelles and intermolecular crosslinks in thermoreversible gels of associating polymers," *Journal of Non-Crystalline Solids*, vol. 307–310, pp. 688 – 697, 2002.

[109] S. Yun, J. Parrondo, F. Zhang, and V. Ramani, "Microstructure-property relationships in sulfonated polyether ether ketone/silsesquioxane composite membranes for direct methanol fuel cells," *Journal of the Electrochemical Society*, vol. 161, pp. F815–F822, 2014.

[110] D. J. Waters, K. Engberg, R. Parke-Houben, L. Hartmann, C. N. Ta, M. F. Toney, and C. W. Frank, "Morphology of photopolymerized end-linked poly(ethylene glycol) hydrogels by small-angle x-ray scattering," *Macromolecules*, vol. 43, no. 16, pp. 6861–6870, 2010.

[111] S. Lin-Gibson, R. L. Jones, N. R. Washburn, and F. Horkay, "Structure-property relationships of photopolymerizable poly(ethylene glycol) dimethacrylate hydrogels," *Macromolecules*, vol. 38, no. 7, pp. 2897–2902, 2005.

[112] E. Mendes, P. Lutz, J. Bastide, and F. Boue, "Soft order in high-functionality star polymer solutions and gels: A small-angle neutron scattering study," *Macromolecules*, vol. 28, no. 1, pp. 174–179, 1995.

[113] G. Ianniruberto and G. Marrucci, "New interpretation of shear thickening in telechelic associating polymers," *Macromolecules*, vol. 48, no. 15, pp. 5439–5449, 2015.

[114] G. Mangiapia, R. Ricciardi, F. Auriemma, C. D. Rosa, F. L. Celso, R. Triolo, R. K. Heenan, A. Radulescu, A. M. Tedeschi, G. D'Errico, and L. Paduano, "Mesoscopic and microscopic investigation on poly(vinyl alcohol) hydrogels in the presence of sodium decylsulfate," *The Journal of Physical Chemistry B*, vol. 111, no. 9, pp. 2166–2173, 2007.

[115] C. Tanford, "Micelle shape and size," *The Journal of Physical Chemistry*, vol. 76, no. 21, pp. 3020–3024, 1972.

[116] W. H. Stockmayer, "Introduction to physical polymer science, by l. h. sperling, wiley-interscience, new york, 1986," *Journal of Polymer Science Part C: Polymer Letters*, vol. 27, no. 4, pp. 146–146, 1989.

[117] V. Lauter-Pasyuk, H. J. Lauter, G. P. Gordeev, P. Müller-Buschbaum, B. P. Toperverg, M. Jernenkov, and W. Petry, "Nanoparticles in block-copolymer films studied by specular and off-specular neutron scattering," *Langmuir*, vol. 19, no. 19, pp. 7783–7788, 2003.

[118] A. Horechyy, N. E. Zafeiropoulos, B. Nandan, P. Formanek, F. Simon, A. Kiriy, and M. Stamm, "Highly ordered arrays of magnetic nanoparticles prepared via block copolymer assembly," *J. Mater. Chem.*, vol. 20, pp. 7734–7741, 2010.

[119] Y. Yao, E. Metwalli, M. A. Niedermeier, M. Opel, C. Lin, J. Ning, J. Perlich, S. V. Roth, and P. Müller-Buschbaum, "Nano- and microstructures of magnetic field-guided maghemite nanoparticles in diblock copolymer films," *ACS Applied Materials and Interfaces*, vol. 6, no. 7, pp. 5244–5254, 2014. PMID: 24621173.

[120] I. Kong, S. H. Ahmad, M. H. Abdullah, D. Hui, A. N. Yusoff, and D. Puryanti, "Magnetic and microwave absorbing properties of magnetite–thermoplastic natural rubber nanocomposites," *Journal of Magnetism and Magnetic Materials*, vol. 322, no. 21, pp. 3401–3409, 2010.

[121] L. Schulz, W. Schirmacher, A. Omran, V. R. Shah, P. Böni, W. Petry, and P. Müller-Buschbaum, "Elastic torsion effects in magnetic nanoparticle diblock-copolymer structures," *Journal of Physics: Condensed Matter*, vol. 22, no. 34, p. 346008, 2010.

[122] G. F. Goya, T. S. Berquó, F. C. Fonseca, and M. P. Morales, "Static and dynamic magnetic properties of spherical magnetite nanoparticles," *Journal of Applied Physics*, vol. 94, no. 5, pp. 3520–3528, 2003.

[123] C. P. Bean and I. S. Jacobs, "Magnetic granulometry and superparamagnetism," *Journal of Applied Physics*, vol. 27, no. 12, pp. 1448–1452, 1956.

[124] W. Palmer, "Magnetocrystalline anisotropy of magnetite at low temperature," *Phys. Rev.*, vol. 131, pp. 1057–1062, Aug 1963.

[125] A. Campanella, O. Holderer, K. N. Raftopoulos, C. M. Papadakis, M. P. Staropoli, M. S. Appavou, P. Müller-Buschbaum, and H. Frielinghaus, "Multi-stage freezing of HEUR polymer networks with magnetite nanoparticles," *Soft Matter*, vol. 12, pp. 3214–3225, 2016.

[126] A. Arbe, J. Colmenero, B. Frick, M. Monkenbusch, and D. Richter, "Investigation of the dielectric β-process in polyisobutylene by incoherent quasielastic neutron scattering," *Macromolecules*, vol. 31, no. 15, pp. 4926–4934, 1998.

[127] A. Faivre, C. Levelut, D. Durand, S. Longeville, and G. Ehlers, "Influence of the microstructure of ppo-based glass-formers on their dynamics as investigated by neutron spin echo," *Journal of Non-Crystalline Solids*, vol. 307–310, pp. 712 – 718, 2002.

[128] M. Tanaka, T. Motomura, N. Ishii, K. Shimura, M. Onishi, A. Mochizuki, and T. Hatakeyama, "Cold crystallization of water in hydrated poly(2-methoxyethyl acrylate) (pmea)," *Polymer International*, vol. 49, no. 12, pp. 1709–1713, 2000.

[129] T. Hatakeyma, H. Kasuga, M. Tanaka, and H. Hatakeyama, "Cold crystallization of poly(ethylene glycol)–water systems," *Thermochimica Acta*, vol. 465, no. 1–2, pp. 59 – 66, 2007.

[130] H. Yoshida, T. Hatakeyama, and H. Hatakeyama, "Phase transitions of the water-xanthan system," *Polymer*, vol. 31, no. 4, pp. 693–698, 1990.

[131] P. Hill, R. MacMillan, and V. Lee, *Tables of thermodynamic properties of heavy water in SI units*. Canada, 1981.

[132] K. Pathmanathan and G. P. Johari, "Dielectric and conductivity relaxations in poly(HEMA) and of water in its hydrogel," *Journal of Polymer Science Part B: Polymer Physics*, vol. 28, no. 5, pp. 675–689, 1990.

[133] S. Cerveny, G. A. Schwartz, R. Bergman, and J. Swenson, "Glass transition and relaxation processes in supercooled water," *Phys. Rev. Lett.*, vol. 93, p. 245702, Dec 2004.

[134] N. Shinyashiki, W. Yamamoto, A. Yokoyama, T. Yoshinari, S. Yagihara, R. Kita, K. L. Ngai, and S. Capaccioli, "Glass transitions in aqueous solutions of protein (bovine serum albumin)," *The Journal of Physical Chemistry B*, vol. 113, no. 43, pp. 14448–14456, 2009.

[135] X. Jin, S. Zhang, and J. Runt, "Dielectric studies of poly(ethylene oxide)/poly(styrene-co-p-hydroxystyrene) blends influence of hydrogen bonding on the dynamics of amorphous blends," *Macromolecules*, vol. 36, no. 21, pp. 8033–8039, 2003.

[136] R. P. Auty and R. H. Cole, "Dielectric properties of ice and solid d2o," *The Journal of Chemical Physics*, vol. 20, no. 8, pp. 1309–1314, 1952.

[137] G. P. Johari and E. Whalley, "The dielectric properties of ice ih in the range 272–133 k," *The Journal of Chemical Physics*, vol. 75, no. 3, pp. 1333–1340, 1981.

[138] A. R. von Hippel, "The dielectric relaxation spectra of water, ice, and aqueous solutions, and their interpretation. i. critical survey of the status-quo for water," *IEEE Transactions on Electrical Insulation*, vol. 23, no. 5, pp. 801–816, 1988.

[139] A. Serghei, M. Tress, J. R. Sangoro, and F. Kremer, "Electrode polarization and charge transport at solid interfaces," *Phys. Rev. B*, vol. 80, p. 184301, Nov 2009.

[140] D. S. Huh and S. L. Cooper, "Dynamic mechanical properties of polyurethane block polymers," *Polymer Engineering und Science*, vol. 11, no. 5, pp. 369–376, 1971.

[141] E.J.Donth, *Relaxation and Thermodynamics in Polymers: Glass Transition.* Akademie-Verlag, Berlin, 1992.

[142] X. Jin, S. Zhang, and J. Runt, "Observation of a fast dielectric relaxation in semi-crystalline poly(ethylene oxide)," *Polymer*, vol. 43, no. 23, pp. 6247–6254, 2002.

[143] J. J. Fontanella, M. C. Wintersgill, P. J. Welcher, J. P. Calame, and C. G. Andeen, "Electrical relaxation in poly(ethylene oxide)," *IEEE Transactions on Electrical Insulation*, vol. EI-20, pp. 943–946, Dec 1985.

[144] R. Böhmer, K. L. Ngai, C. A. Angell, and D. J. Plazek, "Nonexponential relaxations in strong and fragile glass formers," *The Journal of Chemical Physics*, vol. 99, no. 5, pp. 4201–4209, 1993.

[145] A. Killis, J. LeNest, H. Cheradame, and A. Gandini, "Ionic conductivity of polyether-polyurethane networks containing nabph4: A free volume analysis," *Die Makromolekulare Chemie*, vol. 183, no. 11, pp. 2835–2845, 1982.

[146] M. A. Ratner and D. F. Shriver, "Ion transport in solvent-free polymers," *Chemical Reviews*, vol. 88, no. 1, pp. 109–124, 1988.

[147] A. M. Hecht, F. Horkay, P. Schleger, and E. Geissler, "Thermal fluctuations in polymer gels investigated by neutron spin echo and dynamic light scattering," *Macromolecules*, vol. 35, no. 22, pp. 8552–8555, 2002.

[148] M. Doi and S. F. Edwards, *The theory of polymer dynamics*. Oxford University Press, 1994.

[149] T. Hellweg, K. Kratz, S. Pouget, and W. Eimer, "Internal dynamics in colloidal PNIPAM microgel particles immobilised in mesoscopic crystals," *Colloids and Surfaces A: Physicochemical and Engineering Aspects*, vol. 202, no. 2-3, pp. 223–232, 2002.

[150] L. Leibler, M. Rubinstein, and R. H. Colby, "Dynamics of reversible networks," *Macromolecules*, vol. 24, no. 16, pp. 4701–4707, 1991.

[151] T. G. Dewey, *Fractals in Molecular Biophysics,*. New York: Oxford University Press, 1997.

[152] S. Maccarrone, C. Scherzinger, O. Holderer, P. Lindner, M. Sharp, W. Richtering, and D. Richter, "Cononsolvency effects on the structure and dynamics of microgels," *Macromolecules*, vol. 47, no. 17, pp. 5982–5988, 2014.

[153] S. Panyukov and Y. Rabin, "Polymer gels frozen inhomogeneities and density fluctuations," *Macromolecules*, vol. 29, no. 24, pp. 7960–7975, 1996.

[154] A. Onuki, "Scattering from deformed swollen gels with heterogeneities," *J. Phys. II France*, vol. 2, no. 1, pp. 45–61, 1992.

[155] S. Koizumi, M. Monkenbusch, D. Richter, D. Schwahn, and B. Farago, "Concentration fluctuations in polymer gel investigated by neutron scattering: Static inhomogeneity in swollen gel," *The Journal of Chemical Physics*, vol. 121, no. 24, pp. 12721–12731, 2004.

[156] S. Koizumi, M. Monkenbusch, D. Richter, D. Schwahn, B. Farago, and M. Annaka, "Observation of concentration fluctuations in polymer gels performed by neutron spin echo," *Journal of Neutron Research*, vol. 10, no. 3-4, pp. 155–162, 2002.

[157] R. Zorn, D. Richter, B. Farago, B. Frick, F. Kremer, U. Kirst, and L. Fetters, "Comparative study of the segmental relaxation in polyisoprene by quasi-elastic neutron scattering and dielectric spectroscopy," *Physica B: Condensed Matter*, vol. 180, pp. 534–536, 1992.

[158] A. Campanella, A. Brás, K. Raftopoulos, C. Papadakis, O. Vassiliadou, A. Kyritsis, M. Appavou, P. Müller-Buschbaum, and H. Frielinghaus, "Dielectric relaxations of nanocomposites composed of HEUR polymers and magnetite nanoparticles," *Polymer*, vol. 96, pp. 70–80, 2016.

[159] A. Panagopoulou, A. Kyritsis, R. S. i Serra, J. G. Ribelles, N. Shinyashiki, and P. Pissis, "Glass transition and dynamics in bsa-water mixtures over wide ranges of composition studied by thermal and dielectric techniques," *Biochimica et Biophysica Acta (BBA) - Proteins and Proteomics*, vol. 1814, no. 12, pp. 1984–1996, 2011.

[160] "Shimadzu." http://www.shimadzu.com/an/industry/electronicselectronic/fc160306010.htm. 2015.

[161] K. Pielichowski and K. Fleituch, "Differential scanning calorimetry studies on poly(ethylene glycol) with different molecular weights for thermal energy storage materials," *Polym. Adv. Technol.*, vol. 13, no. 10-12, pp. 690–696, 2002.

[162] A. Bartolotta, G. Marco, M. Lanza, and G. Carini, "The fusion of ethylene oxide polymers," *Il Nuovo Cimento D*, vol. 16, no. 7, pp. 825–830.

[163] E. Martuscelli, C. Silvestre, and C. Gismondi, "Morphology, crystallization and thermal behaviour of poly(ethylene oxide)/poly(vinyl acetate) blends," *Die Makromolekulare Chemie*, vol. 186, no. 10, pp. 2161–2176, 1985.

[164] T. M. Connor, B. E. Read, and G. Williams, "The dielectric, dynamic mechanical and nuclear resonance properties of polyethylene oxide as a function of molecular weight," *Journal of Applied Chemistry*, vol. 14, no. 2, pp. 74–81, 1964.

[165] R. W. Sillars, "The properties of a dielectric containing semiconducting particles of various shapes," *Wireless Section, Institution of Electrical Engineers - Proceedings of the*, vol. 12, pp. 139–155, June 1937.

[166] P. Pissis and A. Kyritsis, "Electrical conductivity studies in hydrogels," *Solid State Ionics*, vol. 97, no. 1-4, pp. 105–113, 1997.

[167] J. C. Mauro, Y. Yue, A. J. Ellison, P. K. Gupta, and D. C. Allan, "Viscosity of glass-forming liquids," *Proceedings of the National Academy of Sciences*, vol. 106, no. 47, pp. 19780–19784, 2009.

[168] K. Raftopoulos, B. Janowski, L. Apekis, K. Pielichowski, and P. Pissis, "Molecular mobility and crystallinity in polytetramethylene ether glycol in the bulk and as soft component in polyurethanes," *European Polymer Journal*, vol. 47, no. 11, pp. 2120–2133, 2011.

[169] P. Macedo, C. Moynihan, and R. Bose, "Role of ionic diffusion in polarization in vitreous ionic conductors," *Phys Chem Glasses*, vol. 13, pp. 171–179, 1972.

[170] A. Kyritsis, P. Pissis, and J. Grammatikakis, "Dielectric relaxation spectroscopy in poly(hydroxyethyl acrylates)/water hydrogels," *Journal of Polymer Science Part B: Polymer Physics*, vol. 33, no. 12, pp. 1737–1750, 1995.

[171] A. Kyritsis, K. Raftopoulos, M. A. Rehim, S. S. Shabaan, A. Ghoneim, and G. Turky, "Structure and molecular dynamics of hyperbranched polymeric systems with urethane and urea linkages," *Polymer*, vol. 50, no. 16, pp. 4039–4047, 2009.

[172] M. Wübbenhorst and J. van Turnhout, "Analysis of complex dielectric spectra. i. one-dimensional derivative techniques and three-dimensional modelling," *Journal of Non-Crystalline Solids*, vol. 305, no. 1-3, pp. 40–49, 2002.

[173] M. Wübbenhorst, E. M. Van Koten, J. C. Jansen, W. Mijs, and J. van Turnhout, "Dielectric relaxation spectroscopy of amorphous and liquid-crystalline side-chain polycarbonates," *Macromolecular Rapid Communications*, vol. 18, no. 2, pp. 139–147, 1997.

[174] K. N. Raftopoulos, S. Koutsoumpis, M. Jancia, J. P. Lewicki, K. Kyriakos, H. E. Mason, S. J. Harley, E. Hebda, C. M. Papadakis, K. Pielichowski, and P. Pissis, "Reduced phase separation and slowing of dynamics in polyurethanes with three-dimensional poss-based cross-linking moieties," *Macromolecules*, vol. 48, no. 5, pp. 1429–1441, 2015.

[175] A. Vatalis, A. Kanapitsas, C. Delides, and P. Pissis, "Relaxation phenomena and morphology in polymer blends based on polyurethanes investigated by various thermal analysis techniques," *Thermochimica Acta*, vol. 372, no. 1-2, pp. 33–38, 2001.

[176] K. Se, K. Adachi, and T. Kotaka, "Dielectric relaxations in poly(ethylene oxide): Dependence on molecular weight," *Polymer Journal*, vol. 13, pp. 1009–1017, 1981.

[177] Y. Ishida, "Dielectric relaxation of high polymers in the solid state," *Journal of Polymer Science Part A-2: Polymer Physics*, vol. 7, no. 11, pp. 1835–1861, 1969.

[178] R. Kötitz, W. Weitschies, L. Trahms, W. Brewer, and W. Semmler, "Determination of the binding reaction between avidin and biotin by relaxation measurements of magnetic nanoparticles," *Journal of Magnetism and Magnetic Materials*, vol. 194, no. 1-3, pp. 62–68, 1999.

List of publications

Publications related to the dissertation

- A. Campanella, Z. Di, A. Luchini, L. Paduano, A. Klapper, M. Herlitschke, O.Petracic, M.S. Appavou, P. Müller-Buschbaum, H. Frielinghaus, D. Richter, "Nanocomposites composed of HEUR polymer and magnetite iron oxide nanoparticles: Structure and magnetic response of the hydrogel and dried state", *Polymer*, vol. 60, pp. 176-185, 2015

- A. Campanella, O. Holderer, K. N. Raftopoulos, C. M. Papadakis, and M. P. Staropoli, M. S. Appavou, P. Müller-Buschbaum and H. Frielinghaus, "Multi-stage freezing of HEUR polymer networks with magnetite nanoparticles", *Soft Matter*, vol. 12, no. 13 pp. 3214-3225, 2016

- A. Campanella, A. Brás, K.N. Raftopoulos, C.M. Papadakis, O. Vassiliadou, A. Kyritsis, M.S. Appavou, P. Müller-Buschbaum and H. Frielinghaus, "Dielectric relaxations of nanocomposites composed of HEUR polymers and magnetite nanoparticles", *Polymer*, vol. 96, pp. 70-80, 2016

Other publications

- Federica Acampora, Alberto Maria Marzaioli,Antonella Capuozzo, Marie-Sousai Appavou, Antonella Campanella, Gerardino D'Errico, Carlo Irace, Daniela Montesarchio, Domenica Musumeci, Noemi Kinga Szekely, Rita Santamaria, Cristina De Castro, Luigi Paduano "Lipooligosaccharides as Amphiphiles to Build Liposomes for Effective Drug Delivery: The Case of Anticancer Ruthenium Complex-Based Aggregates", *ChemistrySelect*, accepted manuscript, 2016

Scientific reports

- A. Campanella, H. Frielinghaus, P. Müller-Buschbaum, "Nanocomposites composed of HEUR polymer and magnetite iron oxide nanoparticles: structure and magnetic

response of the hydrogel and dried state" *Lehrstuhl für Funktionelle Materialien, Annual Report*, 2014.

- A. Campanella, H. Frielinghaus, P. Müller-Buschbaum, "Dynamics of nanocomposites composed of HEUR polymer and magnetite iron oxide nanoparticles", *Lehrstuhl für Funktionelle Materialien, Annual Report*, 2015.

Conference talks

- A. Campanella, H. Frielinghaus, D. Richter, "Telechelic polymers and magnetic nanoparticles nanocomposites: thin dry films and hydrogels", *DPG Spring Meeting 2014*, Dresden (Germany), 30.03–4.04.2014.

- A. Campanella, Z. Di, A. Luchini, L. Paduano, A. Klapper, O. Petracic, M. S. Appavou, P. Müller-Buschbaum, H. Frielinghaus, D. Richter, "Nanocomposites composed of HEUR Polymer and Magnetite nanoparticles: Structure and magnetic response of the hydrogel and dried state", *SISN (Neutron Spectroscopy Italian Society) XXV Annual Conference*, Naples (Italy), 3.–4.07.2014.

- A. Campanella, Z. Di, A. Luchini, L. Paduano, A. Klapper, O. Petracic, M. S. Appavou, P. Müller-Buschbaum, H. Frielinghaus, D. Richter, "Nanocomposites composed of HEUR polymer and magnetite iron oxide nanoparticles.", *DPG Spring Meeting 2014*, Berlin (Germany), 15.–20.03.2015.

- A. Campanella, Z. Di, A. Luchini, L. Paduano, A. Klapper, O. Petracic, M. S. Appavou, P. Müller-Buschbaum, H. Frielinghaus, D. Richter, "Nanocomposites composed of HEUR polymer and magnetite iron oxide nanoparticles.", *SoftComp annual meeting 2015*, Ancona (Italy), 9.–11.06.2015.

- A.Campanella, O. Holderer, K. N. Raftopoulos, P. Müller-Buschbaum, H. Frielinghaus, "Structure and dynamics of nanocomposite hydrogels based on HEUR polymers and coated magnetite nanoparticles.", *DPG Spring Meeting 2016*, Regensburg (Germany), 6.–11.03.2016.

- A.Campanella, O. Holderer, K. N. Raftopoulos C. M. Papadakis, M. P. Staropoli, M.S. Appavou, P. Müller-Buschbaum, H. Frielinghaus, "Structure and dynamics of nanocomposite hydrogels based on HEUR polymers and magnetite nanoparticles", *EUPOC 2016 Conference*, Gargnano, Lago di Garda (Italy), 22.–26.05.2016.

Acknowledgments

Here we are. Finally. At this final stage, I would like to acknowledge all the people which have been part of this path of my life.
From the professional side, I would like to thank in particular:

- *Dr. Henrich Frielinghaus, my supervisor at the JCNS institute, for his supervision and his help during my PhD experience*
- *Prof. Dieter Richter, for giving me the opportunity to do my PhD at the JCNS institute*
- *Prof. Peter Müller-Buschbaum, for the opportunity of attaining my PhD at the Physik Departement of the TUM, and being part of the E13 group*
- *The researchers: Dr. Gaetano Mangiapia, Dr. Ana Rita Brás, Dr. Herwin Jerome Unidad, Dr. Konstantinos Raftopoulos and Dr. Simona Maccarrone, for their important help during my PhD and for being good friends*
- *All the instrument responsibles which supported me during my beam times at the FRMII. In particular, I would like to thank Dr. Olaf Holderer for his kind support, and Dr. Marie Sousai Appavou, for being always very helpful*
- *All the members of the JCNS institute, in particular Dr. Noémi Szekely, Dr. Sultan Demirdis, and my office-mates: Rui Wang, Bernhard Hopfenmüller, Alexandra Steffen (finally, Dr.)*
- *All the members of the E13 Lehrstuhl at the Physik Department at the TUM, for being always nice and considering me part of their group.*
- *Prof. Apostolos Kyritsis for giving me the possibility to collaborate with his nice group at the Physics Department of the National Technical University of Athens*
- *Prof. Luigi Paduano for his constant support*

The are people which have been important in both aspects, professional and personal. Here I would like to thank in particular:

- *The amazing group composed of the JCNS/FRMII members: Luca Silvi, Bob Aldus, Jerome Unidad, Maria Maddalena Schiavone, Inês Crespo, Viviane Pecanha Antonio, Manuchar Gvaramia, Simona Maccarrone and Stefan Chang (intruder from Jülich), for making every working day nice and funny, and for being my second family here in Munich*

- *The shippies: Maria Paola Staropoli and Danila Gaudino. No comments need to be added*

Finally, but not less important, I would like to thank the people which have been (and are) important for my personal sphere, in particular during these intense PhD period:

- *Obviously, my family, always the greatest support in my life*

- *Salvatore, I still thank Luca Silvi for making us meet*

- *The special friends I have met in Munich, in particular, Alice and Richard*

In conclusion, I would like to thank myself very much, and Ali Najafi, for the curly braces.
LG,
Antonella